Zinc Oxide Architectures for Gas Sensing and Photocatalytic Applications

Thesis submitted to
the University of Calicut in partial fulfilment of the
requirements for the award of the degree of

Doctor of Philosophy
in Chemistry under the Faculty of Sciences

by
ARSHA KUSUMAM T.V.

Under the guidance of
Dr. N. K. Renuka

DEPARTMENT OF CHEMISTRY
UNIVERSITY OF CALICUT
KERALA-673 635
JUNE 2019

CERTIFICATE

This is to certify that the thesis entitled **"Zinc Oxide Architectures for Gas Sensing and Photocatalytic Applications"** is an authentic record of the research work carried out by **Arsha Kusumam T.V.**, under my guidance for the award of the degree of Doctor of Philosophy in Chemistry under the faculty of Sciences, University of Calicut, Kerala, and the same has not been submitted elsewhere for a degree or diploma.

University of Calicut	**Dr. N. K. Renuka**
Date : 31-01-2020	(Supervising Teacher)

CERTIFICATE

This is to certify that the thesis entitled **"Zinc Oxide Architectures for Gas Sensing and Photocatalytic Applications"** is an authentic record of the research work carried out by **Arsha Kusumam T.V**., under my guidance for the award of the degree of Doctor of Philosophy in Chemistry under the faculty of Sciences, University of Calicut, Kerala, and the same has not been submitted elsewhere for a degree or diploma. Certified that all the modifications suggested by the examiners have been incorporated in the thesis.

University of Calicut
Date : 31-01-2020

Dr. N. K. Renuka
(Supervising Teacher)

DECLARATION

I hereby declare that the thesis entitled **"Zinc Oxide Architectures for Gas Sensing and Photocatalytic Applications"** is the bonafide report of the original work carried out by me under the supervision of Dr. N. K. Renuka, Associate Professor, Department of Chemistry, University of Calicut for the award of the degree of Doctor of Philosophy in Chemistry under the Faculty of Sciences, University of Calicut, Kerala. The content of this thesis have not been submitted to any other institute or University for the award of any degree or diploma.

University of Calicut **ARSHA KUSUMAM T.V.**

Date: 31-01-2020

ACKNOWLEDGEMENT

THANK GOD

This thesis is the result of the work whereby I have been accompanied and supported by many people. It is a pleasant opportunity for me to express my gratitude to all of them.

At this moment of accomplishment, with a deep sense of gratitude, I wish to express my sincere thanks to my research guide Dr. N. K. Renuka for her valuable guidance, constant support, and scholarly inputs I received throughout the entire research period. Her deep insight helped me a lot at various stages of my research work. Under her guidance, I successfully overcame many difficulties and learned a lot. I sincerely thank her for the prompt reading and careful analysis of my thesis.

I would like to thank our present Head of the Department, Dr. Yahya Ismail, and the former Heads of the Department, Dr. P. Raveendran and Dr. K Muraleedharan for permitting me to use the research facilities in the Department. I express my sincere thanks to all the other Faculty members of the department. I wish to thank the Office staffs (present and former) and Librarian of the department for their services during my work. I thank Mr. K. Satheesan, for his help with the instrumentation.

I extend my sense of gratitude to Dr. K. N. Madhusoodanan, Vice-Chancellor, Cochin University of Science and Technology to grant me the permission to do the application study in Department of instrumentation, CUSAT. My heartfelt thanks to my dearest friend Siril V.S., Department of Instrumentation, CUSAT for her candid support and help. Her timely help and friendship shall always be remembered.

I extend my gratitude to CSIF, Calicut University, STIC Cochin (CUSAT), SAIF (IIT Bombay), IIT (Roorkee), NIT, Calicut for helping with characterisation part.

My sincere thanks to the really supportive and active young research scholars of the department for all the co-operation and care I received. I am thankful to my former research mates for their support during my work. Words fail short to express my love and affection to my dearest colleagues Dr. Divya T, Dr. Nikhila M.P., Dr. Anju M., Akhila A.K., Ansi V.A., Varsha Raveendran, Nidhisha V, Anjali C, Thasleena Panakkal and Indhu V. Their constant love, support, care and encouragement helped me to overcome all the difficulties during my research carrier. Special thanks to Nadira P.P, my friend, colleague and neighbour. I really appreciate her valuable support during the crucial moments of my research work.

Special thanks to all my teachers, especially at Mar Thoma College, Thiruvalla; Prof. Mary Sarah Cherian, Dr. Koshy John, Dr. Thomas Mathew, Dr. Raju Thomas, Dr. Joyes Jacob, Prof. Kurian John, Prof. P.G. Philip for their encouragements at different stages of the academic life. They are the sole reason for accomplishing this venture. I am so grateful to all my friends for their everlasting love and encouragement. Especially Ms. Neethu Sadasivan, Ms. Midhu George Veeran, Ms.Mercy Kuriakose and Ms. Sherin Punnoose.

I find no words to express my feelings towards my Chachan and Amma who have given me the freedom to choose my path. They taught me the value of hard work and rendered me enormous support during the whole tenure of my research work. Their conviction and belief in me made to change the entire impediment which came across this journey. Their patience and sacrifice will always remain as a main source of inspiration for *me throughout my life. I remember my grandparents at this moment, their prayers and blessings are the strength of my life. I thank my father-in-law and mother-in-law for their cooperation and valuable support. I am thankful to my brother Aneesh Kumar T.V, Jeothy Lakshmi P.S, Adinath, Rakesh P, Sumeera S, Sreehari, Sreeharsha and all other family members for their care and support.*

I express my thanks to my husband Sreekesh P, he was a source of constant inspiration and his whole hearted support made me to realize my dream. I would like to treasure the moments with the blossom of my life, Poppy, whose innocent smile makes all the stress vanish and make me to look forward for the bright future.

Finally I acknowledge authorities of CSIR for the financial assistance to complete this work.

ARSHA KUSUMAM T.V

To my Family………..

Preface

Environmental pollution is one of the most serious problems that the humanity and other life forms on our planet face today. Environmental pollution can be defined as "the contamination of the physical and biological components of the environment system to such a magnitude that typical environmental processes are harmfully affected." Pollutants can be naturally occurring or man-made substances, but they are considered contaminants when in excess of standard levels. The rules for protection of the environment are stricter in developed countries than in developing countries. If the norms of developed countries are applied in India, costs will be very high. Thus, the standards selected should be compatible with the country's economic situation.

Atmospheric pollutants such as nitrogen oxides (NO_x), carbon monoxide, sulphur dioxide and volatile organic compounds (VOCs), chiefly emanating from industrial activities and transportation vehicles, are harmful to human health. Great efforts have been made to develop devices that can detect the atmospheric pollutants. In this direction metal oxide based chemiresistive gas sensors are gaining much attention. High sensitivity, low response and recovery characteristics, low maintenance cost, good selectivity and linearity etc. make metal oxide based gas sensors more reliable and long lasting. The gas sensors based on metal oxides are cost effective and portable too.

The rapidly increasing population, depleting water resources, and climate change resulting in prolonged droughts and floods have rendered drinking water a competitive resource in many parts of the world. Traditional water/wastewater treatment technologies remain ineffective for providing adequate safe water due to increasing demand of water coupled with stringent health guidelines and emerging contaminants. In this scenario, heterogeneous photocatalysis using semiconductor metal oxides is gaining much importance in wastewater treatment for the past few decades.

Among the various semiconductor metal oxides, zinc oxide is a renowned semiconducting multifunctional material having wide technological applications. Zinc oxide (ZnO) has been intensively researched because of its unique properties, which make it adequate in various applications in industry, health, and research. Besides, the cost effectiveness, environmental friendly nature, availability and the simple fabrication methods make zinc oxide a potential candidate for various commercially important applications. Herein, the gas sensing and photocatalytic properties of zinc oxide are explored. Morphologically different zinc oxide architectures are fabricated, viz., nanoparticles, nanosheets, nanorods, nanoparticle assembled flowers, nanosheet assembled flowers, and nanorods assembled flowers for gas sensing and photocatalytic applications. NO_2 and NH_3 constitute the two analyte gases. The photocatalytic activity is monitored by studying Rhodamine B dye degradation and reduction of hexavalent chromium from aqueous solution.

The thesis consists of six chapters.

The first chapter gives a general introduction on environmental pollution, especially air pollution and water pollution. The various environmental pollutants, their sources and harmful effects are discussed in detail. A brief review on different metal oxides for gas sensing and photocatalytic application is also provided. A detailed description of the use of zinc oxide as a gas sensing tool and photocatalyst is given in this chapter.

The second chapter includes the experimental methods used for the present investigations. The hydrothermal synthetic strategy adopted for the synthesis of six morphologically different zinc oxide architectures and materials required for the synthesis are discussed here. Modification of the highly efficient zinc oxide photocatalyst with copper, iron and silver is also carried out. It also covers the fundamental working principles of various characterization techniques adopted, such as X-Ray Diffraction analysis (XRD), Scanning Electron Microscopy (SEM), Transmission Electron Microscopy (TEM), Fourier Transform Infra-Red spectroscopy (FTIR), UV Diffuse Reflectance Spectroscopy (UV-DRS), Photoluminescence Study (PL), Brunauer- Emmett -Teller (BET) Surface area analysis and X-ray Photoelectron Spectroscopy (XPS). Experimental details of the gas sensing and photocatalytic application studies are also discussed.

The third chapter presents a detailed discussion on the results of various characterization techniques used for the analysis of six morphological variations of zinc oxide structures. A detailed description of growth mechanism with a special emphasis on crystal plane orientation of zinc oxide architectures are also given. Chapter four comprises of the results and discussion of the gas sensing application of zinc oxide towards NO_2 and NH_3. A brief introduction on gas sensor applications, with special mention on zinc oxide based NO_2 and NH_3 sensors and their gas sensing mechanism is also presented here. Various factors influencing gas sensing properties of zinc oxide have been investigated. A comparison of the efficiency of the active system with previously reported ones is also made.

Photocatalytic applications of zinc oxide architectures are presented in chapter 5. This chapter is divided into two parts. Part A includes the photocatalytic reduction of hexavalent chromium. With a brief introduction on the importance of the removal of Cr(VI) from the waste water, the investigation results of the photocatalytic removal of hexavalent chromium using zinc oxide architectures is discussed in detail. The factors affecting the photoreduction of Cr (VI) and the reusability of the catalyst is also investigated. Part B deals with the photocatalytic degradation of the organic dye, Rhodamine B using the prepared zinc oxide catalyst systems. This section also gives a detailed discussion on the characterisation and photocatalytic activity of zinc oxide catalyst modified with copper, iron and silver. Influence of the amount of silver on the photocatalytic activity and the factors affecting photocatalytic dye degradation of the highest active system are discussed. Concomitant removal of Rhodamine B and hexavalent chromium is carried out using the silver modified zinc oxide system is also investigated.

Chapter 6 summarizes the main results in the thesis and provides the scope for future works.

CONTENTS

Preface

CHAPTER 1

CHAPTER 2

CHAPTER 3

CHAPTER 4

CHAPTER 6

ABBREVIATIONS

ZSF	Zinc oxide nanosheet flowers
ZRF	Zinc oxide nanorod flowers
ZPF	Zinc oxide nanoparticle flowers
ZS	Zinc oxide nanosheets
ZR	Zinc oxide nanorods
ZP	Zinc oxide nanoparticles
AgZSF	Silver loaded zinc oxide sheet flower
CuZSF	Copper loaded zinc oxide sheet flower
FeZSF	Iron loaded zinc oxide sheet flower
CTAB	Cetyltrimethylammonium bromide
HMTA	Hexamethylene tetramine
PVP	Polyvinylpyrrolidone
ppm	Parts Per Million
ppb	Parts Per Billion

Chapter 1

General Introduction

1 Environment and environmental pollution

Mankind is the product of his environment. The term environment covers "water, air and land and the inter-relationship which exist among and between water, air, land and human beings, other living creatures, plants, micro-organisms and property" [1]. The wellbeing of human life lies in his harmony with the environment. From the Vedic era itself, the people were aware of the importance of the environment and its protection. At that time, man has a close relationship with his environment, and he worshiped air, water and earth as goddess. They had a holistic approach towards Mother Nature and preserved each and every components of it. Now, modernization and urbanization due to the upsurge in technological field have dramatically changed human being's attitude towards his environment.

Advances in the area of science and technology have improved our life style to a great extent. Our day-to-day life became more comfortable and easier with these developments. But there is two sides for every coin. Rapid growth of industrialization has led to the deterioration of air, water and soil by the discharge of toxic materials to the biosphere. Besides all the benefits, we are faced with a variety of environmental issues such as air pollution, water pollution, soil pollution etc. We are the victims of the dramatic climate change associated with these developments in technological field. The negative impact of these climate changes are gravely affecting the aquatic, aerial and terrestrial animals and vegetation. It is our responsibility to keep the environment free from the contaminants, because we cannot deny the birth right of our future generation to have a clean air, water and earth. Addressing all these problems is the key global challenge that we face today, and if not done properly, we will be doomed for disasters.

Centred on this, a large quantum of research is going on to nullify the harmful effects of these environmental issues. Many initiatives are taken by world-wide authorities for the protection of environment. International environmental organizations like United States Environmental Protection Agency (US EPA), Intergovernmental Panel on Climate Change (IPCC), Greenpeace and World Wildlife Fund (WWF) are working for the protection of environment which includes land conservation, wildlife preservation and climate change prevention.

India is the first country to include provisions for the protection of environment in their constitution. The Water (Prevention and Control of Pollution) Act (1974) to provide for the prevention and control of water pollution, and for the preserving or refurbishing of wholesomeness of water in the country. The Air (Prevention and Control of Pollution) Act for the prevention, control and abatement of air pollution in India was endorsed in 1981. The environment protection act in 1986 has aimed at the protection and improvement of the environment. The terms “environment”, “environmental pollutants" and environmental pollution are well defined in section 2 under definitions of this act. The industries or individuals which violate the provisions of this act will be punishable with penalty.

Some of the major environmental problems, in addition to air pollution, water pollution and soil pollution are global warming, climate change, natural resource depletion and deforestation, loss of biodiversity, ozone layer depletion, photochemical smog and acid rain. Most of these problems are triggered by air pollution and water pollution. We will have brief discussion on air and water pollution, monitoring and the abatement measures of these pollutions in the coming sections.

1.1 Air pollution

Air pollution is one of the major impacts of industrial revolution and has become a main anxiety of the society. The substances in the atmosphere that can cause adverse effects to human health and environment can be considered as air pollutants. A number of poisonous gases enter the atmosphere through natural and anthropogenic activities. The industrial and automobile exhaust emissions produce a major fraction of air pollution. Agriculture, waste management and household activities, fossil fuel burning etc. are the other man-made sources of air pollution. The natural sources include volcanic eruption, dust storms, wild fires etc. The concentration of these pollutants when exceeds their permissible limit turn out to be life threatening and causes environmental imbalance.

Air pollutants may be toxic gases, liquid droplets, and particulate matter. These are categorized into primary pollutants and secondary pollutants. Primary air pollutants are directly emitted from the source whereas the secondary pollutants are not. The common primary air pollutants found in the atmosphere are carbon monoxide (CO), sulphur dioxide (SO_2), nitrogen oxides (NO_x), volatile organic compounds (VOC's), ammonia (NH_3), particulate matter etc. Secondary pollutants include ground level ozone (O_3) and peroxyacetyl nitrate. Nitrogen dioxide being a primary air pollutant results in the formation of ground level ozone, a secondary air pollutant. It has adverse effect on plants and animals and will damage fabrics, rubber and paints. Photochemical smog is an aftermath of the presence of ozone in the troposphere. The harmful effect of this phenomenon include reduced visibility, eye irritations and respiratory ailments. Acid rain is another problem caused by air pollution. The presence of sulphur and nitrogen oxides in the atmosphere fallouts in acid rain which badly affect human health, forest, wildlife and aquatic species, and causes damage to buildings.

The greenhouse gases such as carbon dioxide, methane etc. can trap heat in the atmosphere and increase the temperature of atmosphere. Climate change due to air pollution become a major headache for the community. The rise in global warming, as a consequence of increase in atmospheric temperature, due to the burning of fossil fuels and release of toxic gases have various harmful effect on the environment. It results in the melting of polar ice, rise in ocean temperature and sea level, unnatural weather patterns like flash floods, excessive snow or desertification, change in seasons etc. This change in overall weather scenario will adversely affect the social, economic and political status of the society.

Air pollution has caused respiratory diseases such as asthma, heart disease, stroke, chronic obstructive pulmonary diseases and cancer. According to world health organization, 4.2 million premature death occurred in 2016 due to poor air quality. According to a new report by Greenpeace and AirVisual (2018), twenty two out of 30 worst air polluted cities are in India, New Delhi being ranked in the world's most air polluted capital. Some of the serious situations of air pollution in India can be visualized from Figure 1.

Figure 1. Air pollution in India (Adapted from various sources in internet)

1.1.1 Air pollution monitoring

The elevated air pollution has forced the world-wide authorities to frame rules and regulations to control the emission of toxic pollutants to the atmosphere. A huge efforts have been taken by many countries for the monitoring and control of environmental pollution. The conventional analytical techniques used for monitoring air pollution, such as gas chromatography and optical spectroscopy are inefficient in the sense that they are time consuming and require high operational cost. The invention of solid state gas sensors is a great achievement in this juncture, which resulted from the man's quest to imitate the Nature, as gas sensors are more or less like an electronic nose. Sensor technology is ubiquitous in today's wold and gas sensors have become an indispensable part of our daily life.

1.1.2 Gas sensors

A gas sensor is a device, which on exposure to gaseous species, can change any one of its physical properties such as mass, electrical conductivity, capacitance etc. and produce measurable signals. Different gas sensors have been developed for the past few decades based on their operating principles, nature of sensing material etc., such as chemiresistive gas sensors, catalytic combustion gas sensors, potentiometric gas sensors, acoustic gas sensors and optical gas sensors. Among them, chemiresistive gas sensors (chemosensors) using semiconductor metal oxides are the potential candidates for gas sensing.

Gas sensors find application in various fields as shown in Figure 3.

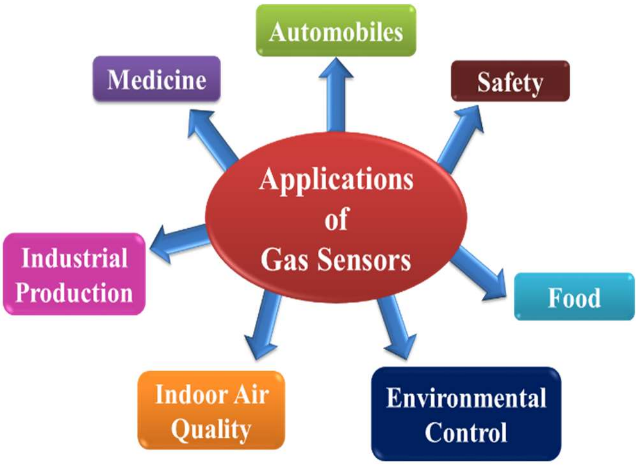

Figure 3. Applications of gas sensors

1.1.3 Gas sensor characteristics

Gas sensors are characterized by the following parameters. The discussion is mainly confined to sensors that produce measurable change in electrical resistance of the material, upon exposure to the gases.

- ***Sensitivity***: The term sensitivity can be defined as the ratio of change of resistance in the analyte gas i.e., $\Delta R = R_a - R_g$, to the value of resistance in air R_a. It is usually expressed in percentage values.

  $$\text{Sensitivity, } S = [(R_a - R_g)/R_a] \times 100$$

  Where R_a and R_g are the resistance of the material in air and in the presence of analyte gas respectively. The resistance change in semiconducting gas sensors on exposure to reducing and oxidizing gases are summarized in table 1.

Semiconductor	Reducing gas	Oxidizing gas
n-type	Resistance decreases	Resistance increases
p-type	Resistance increases	Resistance decreases

- ***Selectivity:*** The selectivity of a gas sensor can be referred as the specific response towards a particular molecule in the presence of other interfering species. This can be expressed as:

$$Selectivity = \frac{Sensitivity\ of\ a\ particular\ gas}{Sensitivity\ towards\ interfering\ gases}$$

The selectivity of a gas sensor should always be greater than unity.

- ***Response and recovery time:*** The response and recovery time of gas sensors are defined as the time taken by the sensor to reach 90% of the response value in the gas atmosphere and 10% of the base value in air respectively.
- ***Stability:*** The ability of a sensor to reproduce its performance for a period of time is termed as its stability.
- ***Operating temperature:*** The temperature at which the sensor has shown the maximum response value.
- ***Detection limit:*** The lowest concentration of analyte gas which can be detected by the sensing material under given conditions.
- ***Dynamic range:*** The analyte concentration range between the detection limit and the highest limiting concentration is known as the dynamic range of the sensor.

- ***Linearity:*** Linearity of a gas sensor can be defined as the relative deviation of an experimentally determined calibration graph from an ideal straight line.
- ***Resolution:*** The lowest concentration difference that can be distinguished by the gas sensor is termed as its resolution.

An ideal sensor should be highly sensitive and selective towards analyte gases. They must possess fast response and recovery characteristics, low detection limit, a large dynamic range, good linearity and a long life cycle. The sensor should operate at low temperatures with minimum power consumption. High sensitivity, low response and recovery characteristics, low maintenance cost, good selectivity and linearity etc. make metal oxide based gas sensors more reliable and long lasting. The gas sensors based on metal oxides are cost effective and portable too.

1.1.4 Chemiresistive gas sensors based on metal oxides

Semiconductor metal oxides undergo resistance change upon exposure to oxidizing or reducing gases. In the presence of oxidizing gases, the resistance of the material increases, while the resistance decreases on exposure to reducing gases. Metal oxide based chemiresistive gas sensors are attractive due to their high sensitivity, fast response-recovery time, dynamic range of detection and cost effectiveness. They are easy to handle and require low maintenance. Since these type of sensors satisfy most of the characteristic features of the gas sensors, enormous efforts are going on in this area to develop gas sensors operating at low temperatures, with high sensitivity and selectivity. Different metal oxides such as SnO_2, ZnO, WO_3, In_2O_3, CuO, TiO_2 etc. have been widely employed as sensing platform for the past few decades. Some of the important metal oxide gas sensors are discussed below.

i. SnO_2

Tin oxide is the most studied semiconductor material for gas sensor application over the past few decades [2-4]. This n-type semiconductor is used for detecting various gases such as carbon monoxide, hydrogen sulphide, nitrogen oxides, ammonia, acetone, ethanol etc. The low cost, high thermal and chemical stability of tin oxide makes it more suitable for gas sensing. The lack of selectivity is the major problem associated with SnO_2 based sensors. The problem can be resolved by the addition of foreign materials in the sensor matrix [5-8]. Other metal oxides and noble metals are used for improving the sensing characteristics of tin oxide gas sensors.

ii. ZnO

Zinc oxide is the first material used for gas sensor applications [9]. Since then the field of gas sensor technology has emerged dramatically. It is an n-type semiconductor possessing excellent characteristics for various technological applications. Zinc oxide has been explored for sensing both reducing as well as oxidizing gases including toxic and non-toxic gases. The gas sensing property of zinc oxide towards different gases like nitrogen oxides, sulphur dioxide, humidity, ammonia, ethanol and various volatile organic compounds have been reported [10-15]. The sensing characteristics mainly depend on the size and morphology of the sensing materials. The simple fabrication methods of zinc oxide in various morphologies has attracted zinc oxide towards gas sensing applications.

iii. WO_3

Tungsten oxide is also a promising candidate for gas sensor application and is widely used for environmental and safety purposes [16-18].

Since it is an n-type semiconductor, the major charge carriers present in the material are electrons. It is found to be sensitive towards a large variety of gases. Like other metal oxide gas sensors, the lack of selectivity of WO_3 limits its application in specifically detecting one analyte gas from a mixture of gases.

iv. In_2O_3 [19,20]

Indium oxide gas sensors are found to be useful in the detection of noxious and explosive gases. The high performance, reliability and short response time make it suitable for sensor applications. The selectivity issue of the sensor material can be resolved by tuning the morphology and by doping.

Various other n-type metal oxides such as TiO_2 [21], Fe_2O_3 [22], etc. have been used for the detection of various environmentally important gases. A few p-type metal oxides are also used a gas sensing materials such as CuO [23, 24], NiO, Cr_2O_3 etc. The major problem associated with most of the metal oxide gas sensors is their lack of selectivity. The problem can be solved by tuning morphological and structural features, controlling the grain size and incorporation of other materials such as graphene, other metal oxides and noble metals, with the sensing materials.

1.2 Water pollution

Water is an essential component which sustains life on earth. Almost 70% of the earth's surface is covered with water. However, more than 97% of the total water content in earth is salt water and is in non-drinkable form. The remaining 3% of earth's fresh water resources mostly includes icecaps and glaciers (69%) and ground water (30%). Only less than 1% fresh water is thus available for human consumption. Consequently, the effective utilization and protection of these fresh water resources is of great importance.

We are now facing a global water quality catastrophe. The water quality is important in the sense that it defines the well-being of the environment, society and the economy. Rapid industrialization, increasing food production, continuing population growth and urbanisation etc. are placing pressure on water resources and increasing the unfettered or illegal discharge of contaminated water within the fresh water bodies. As a consequence, the clean potable water sources are diminishing. Huge amount of wastes from industrial and agricultural sector are discharged in the rivers. The quality of water can be compromised by the presence of a myriad of different components such as toxic chemicals, radiological hazards and infectious agents. The toxic chemicals include both organic and inorganic waste materials from industrial, domestic as well as agricultural run offs. They are mainly organic dyes, phenolic compounds, pesticides, heavy metals etc. The presence of these materials above its acceptable levels in fresh water system presents a global threat to human health and wellbeing.

The industrial as well as domestic discharge include both biodegradable and non-biodegradable wastes. Biodegradable wastes are not toxic in its lower concentrations, and can be easily decomposed by the microorganisms by the expense of the dissolved oxygen form water. Hence their higher concentration creates biological oxygen demand (BOD) and produces problems in aquatic environment. The biodegradable waste include domestic waste, sewage effluent, agricultural residue, paper, wood, clothes etc. that can be easily degraded under normal conditions. On the contrary, non-biodegradable wastes are highly toxic even at low concentrations. They cannot be easily decomposed by any of the microorganisms present in water bodies. Consequently, they will persist in the water bodies for a long time. Consumption of this water will create bioaccumulation of these toxins in organisms and results in bio-magnification. The common non-biodegradable wastes include pesticides, synthetic organic dyes, phenolic compounds, heavy metals etc. The common sources of water pollution ate portrayed in Figure 2.

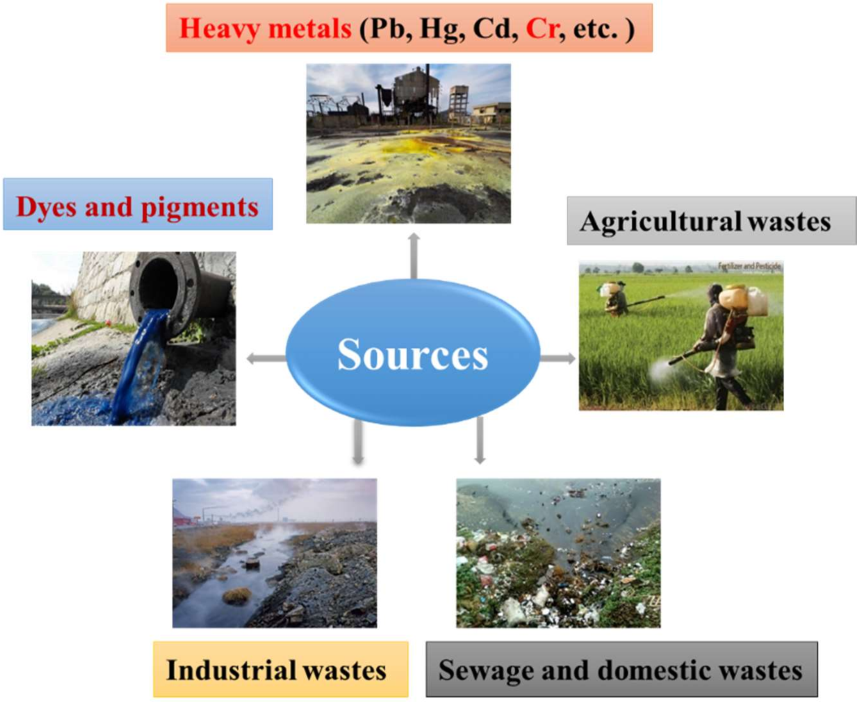

Figure 2. Sources of water pollution

1.2.1 Water pollution from textile industry

The textile dying and manufacturing industries consume a large amount of clean water for processing, dyeing and printing, and produces the highest rate of water pollution. A myriad of toxic chemicals used in these industries are discharged to the water bodies without sufficient treatment.

Many of these chemicals directly or indirectly affect the human health. It was reported that about 1.6 million litres of water is consumed per day for the production of about 8000 kg of fabric. The removal of surplus colour from the dyed and printed fabric as well as cleaning the printing machines to remove loose colour paste from printing blankets, printing screens and dyeing vessels require huge amount of water. The waste water, after all these process, loaded with a number of toxic chemicals, which when discharged to the water bodies without sufficient pre-treatment, create appalling environmental problems.

1.2.2 Water pollution by heavy metals

Another major problem confronted by the society is water pollution due to heavy metal contamination. A number of heavy metals such as Mercury (Hg), Cadmium (Cd), Lead (Pb), Chromium (Cr), Arsenic (As) etc. produce serious health as well as environmental problems. They are produced by both natural and anthropogenic activities. Due to the rapid industrialization, the accumulation of heavy metals in earth surface has increased many times by human activities rather than from natural sources. The mining industries are considered as the major anthropogenic source of heavy metal pollutants. Most of the heavy metal pollutants are carcinogenic and lethal to human life. They enter the body system through water, food and air, and bio-accumulate over a period of time. These non-biodegradable heavy metal pollutants tend to accumulate in the ecosystem, thereby deteriorating human health and environment.

The toxic effects of heavy metals can be attributed to their ability to form bonds with thiol group of proteins and alters the biochemical lifecycle. Some of the heavy metals like iron, cobalt, zinc, cop-per, manganese, etc., in its lower concentration are considered to be essential metabolites while their excess causes life threatening situations. The heavy metals such as chromium, mercury, cadmium, arsenic etc. are considered to be deadly even at very low concentrations. The presence of heavy metal ions in drinking water causes several fatal diseases such as cardiovascular diseases, cancer, brain damage, failure of kidney and nervous system. It also upset the physical and mental growth of infants and children.

Apart from these, various other sources like agricultural waste, sewage, domestic wastes etc., also contribute to water pollution.

1.2.3 Water pollution abatement

A paradigm shift is required in strategies for the prudent management of waste water. Various programmes have been implemented world-wide for controlling water pollution. Serious concern is given to rejuvenate our polluted rivers, in our country. The enforcement of strict rules and regulations for the discharge of industrial waste water to the fresh water bodies must be strengthened in order to avoid water pollution. Governments are conducting programmes to make people aware about the seriousness of water pollution and encouraging the domestic users as well as industries to recycle and reuse the waste water at source. Effluent treatment plants should be installed in industries.

Waste water management is a hurdle in front of the society. Many methods have been employed for the treatment of waste water. Some of the conventional techniques that are being used for waste water treatment include precipitation, coagulation/flocculation, adsorption, ion-exchange, biological treatment, ozonisation, electro-dialysis, and membrane separation. These techniques have inherent limitations as they are less efficient, require high operational cost and leads to the production of secondary sludge. Here arises the need of a promising technique for water purification. In this scenario, heterogeneous photocatalysis is gaining much importance in wastewater treatment for the past few decades.

1.2.4 Photocatalytic treatment of waste water

Photocatalysis, an advanced oxidation process, using semiconductor catalysts is an effective, innovative and clean technology.The term heterogeneous photocatalysis can be defined as, "the process in which light photons are used to activate a solid photocatalyst, which changes the rate of a chemical reaction without being involved itself in the process of chemical transformation. This technique can be effectively employed for the removal of organic and inorganic pollutants from waste water.

Semiconductor metal oxides have been employed as photocatlyst for the effective treatment of waste water because of their characteristic electronic structure, light absorption properties, excited-state lifetimes and charge transport characteristics. When photons of suitable energy fall on the surface of a metal oxide, excitation of electrons from valence band to conduction band takes place by the absorption of a photon of energy equal to or higher than the bandgap energy of the material. This results in the formation of an electron- hole pair, which is a prerequisite for the process of photocatalysis.

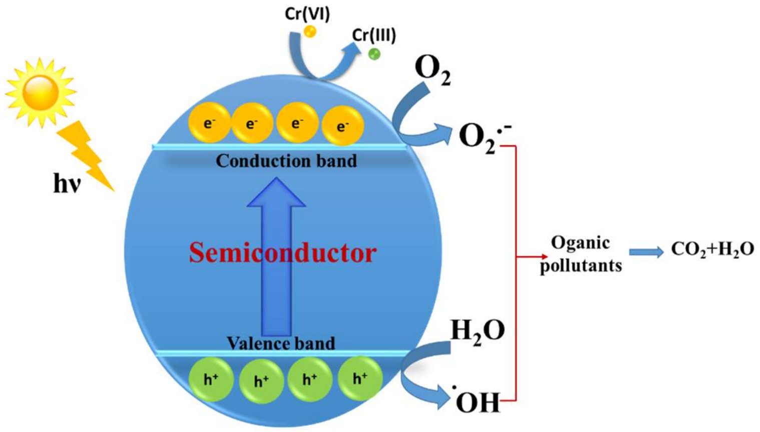

Figure 4. General mechanism of photocatalysis

The mechanism of photocatalysis is portrayed in Figure 4. The mechanism involves the following steps:

(i) Light harvesting

(ii) Excitation of electrons to conduction band, leaving behind holes in the valence band

(iii) Electron/hole migration, transport and recombination

(iv) Utilization of electrons and holes for photocatalytic reduction and oxidation processes respectively.

The electrons in the conduction band reduces oxygen molecules to superoxide radicals and holes react with water molecules to form hydroxyl radicals by photo-oxidation process. The highly oxidizing hydroxyl radicals and superoxide radicals together with holes can easily decompose organic pollutants in the waste water to its less toxic forms i.e., carbon dioxide and water. The excited electrons can also aid the photocatalytic reduction of heavy metal pollutants. The advantages of photocatalysis over other conventional waste water treatment techniques is displayed in Figure 5.

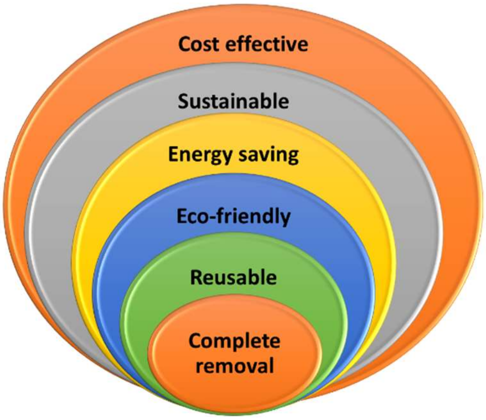

Figure 5. Advantages of photocatalysis over conventional techniques

1.2.5 Advances in metal oxide nanostructures in photocatalytic water treatment

The emergence in the field of nanoscience and technology has dramatically changed the perceptions of present world. Nanoscience have influenced almost all the fields including basic science, technology, economics and politics. Even our day to day life depends on the progress in nanotechnology. Nanomaterials with exceptional properties than their bulk counter parts have revolutionized the technological field. The optimization and control of size in the nanometer scale have crucial role in enhancing the properties of the materials. Carbon nanotubes, grapheme, metal oxide nanomaterials, nano metal particles etc. are all promising candidates for the future applications.

Semiconductor metal oxides have been widely employed as a photocatalyst for the removal of contaminants from waste water. Various metal oxides have been used for decades as a photocatalysts for the effective treatment of waste water. Some of the important metal oxide photocatalysts to be quoted in this direction are discussed below.

i. Titanium dioxide (TiO_2)

Titanium dioxide is the most studied system for photocatalytic applications. The Degussa P25 is a highly efficient photocatalyst due to the contemporary presence of anatase and rutile TiO_2 structures. Numerous organic pollutants such as synthetic organic dyes, pesticides, phenolic compounds etc. were removed from waste water using TiO_2 as photocatlyst. The catalyst can absorb a small amount of photons from the visible region, thereby reducing its application in visible light. Modification of the catalyst system with other materials is a suitable option for extending its activity to visible range.

Various types of titania nanostructures have been studied for the photocatalytic application. Liang et al. prepared titania nanotubes for the photocatalytic degradation of 2,3-dichlorophenol in aqueous solution [25]. Their results have shown that the photocatalytic activity of the TiO_2 nanotube depends on its structural characteristics such as length of the tube, wall thickness and crystallinity. Mesoporous TiO_2 nanoparticles were modified by curcumin and the incorporation of curcumin on titania surface changes the removal direction from adsorption to the photocatalytic pathway [26]. The crystal plane dependent photocatalytic activity of TiO_2 nanosheets were explored by Han and his co-workers [27]. Titania nanosheets with high percentage of exposed (001) planes are highly efficient for the photocatalytic degradation of methyl orange. But the high cost and difficulty in the removal of catalyst from the reaction medium necessitates an alternative for this catalyst.

ii. Zinc oxide (ZnO)

ZnO is considered a suitable alternative to TiO_2 because of its good catalytic, optoelectronic and photochemical properties along with its low cost. It has a band gap value of 3.7 eV. The photogenerated holes in zinc oxide have strong enough oxidizing power to decompose organic pollutants because of the valence band position of zinc oxide. ZnO has been tested to decompose aqueous solutions of numerous dyes, and many other environmental pollutants. In some of the cases, zinc oxide has been reported to be more efficient than titania [28-39].

Hierarchically assembled porous ZnO spherical nanoparticles showed a superior photocatalytic activity than TiO_2 nanoparticles for the degradation of phenol [40]. Zinc oxide nanoflowers were more efficient than nanorods for the photocatalytic degradation of 4-chlorophenol under UV irradiation [41]. The outstanding performance of the nanoflowers is due to the presence of larger amount of oxygen vacancy on the surface of the material. Similarly, the 3D flower-like zinc oxide hierarchical microstructures prepared by a low-temperature aqueous solution route were more active than other nanostructured zinc oxide powders i.e., nanosheets, nanoparticles and nanorods [42].

iii. Copper oxide (CuO)

The copper oxide, CuO is a p-type semiconductor with an indirect band gap of 1.2 – 1.9 eV. The material has become a focus of attention due to its key role in environmental remediation and biopharmaceutical industries [43]. Vaidehi et al. have synthesized copper oxide nanoparticles through green method by using *Solanum lycopersicum* leaf extract [44]. The system is found to be a potential biocidal and photocatalytic agents. Copper oxide nanoparticles prepared from different precursor solution were highly efficient for the removal of a numerous dyes viz. Rhodamine B, methylene blue, methyl orange dyes [45].

iv. Tungsten Oxide (WO_3)

Tungsten Oxide, WO_3 is not a versatile catalyst as that of titania. WO_3 has generally showed a low photoactivity to degrade pollutants that have been ascribed to the higher rate of electron-hole recombination and to the low rate of electron transfer to oxtgen molecule. Sayama and co-workers used amorphous peroxotungstic acid as the precursor for the preparation of WO_3 catalyst, which was more active than WO_3 systems obtained with different methods [46]. The high activity for the degradation of various organic compounds was explained by the good crystallinity, high surface area, and efficient light absorption in the visible light region. Incorporation of foreign materials can improve the photocatalytic performance of tungsten oxide by lowering the electron-hole recombination rate [47-52].

1.3 Present work and relevance

In the backdrop of environmental pollution, both water and air pollution, we have made an effort to device gas sensors and photocatalysts based on zinc oxide architectures. Zinc oxide structures with various morphologies have been utilized for gas sensing and photocatalytic applications. Nitrogen dioxide (NO_2) and ammonia (NH_3) sensing as well as photocatalytic removal of hexavalent chromium and Rhodamine B using zinc oxide architectures are examined.

1.3.1 Gas sensing

The analyte gases selected for the present work is nitrogen dioxide and ammonia. A brief description on these gases are given below:

Nitrogen dioxide, a strong oxidizing gas, is one among the most hazardous gaseous pollutants produced by both natural and anthropogenic activities. A reasonably high concentration of this brownish red gas enters to the atmosphere through human activities. It is a major component in automotive emission, and is also released from industrial sources. The detrimental effects of NO_2 include damage to respiratory tracks, cardiovascular diseases, skin or eye burn etc. It also degrades the dyes and pigments in the textile industry. Environmental imbalance is also noted, as it produces ground level ozone which causes photochemical smog. Apart from this, acid rain caused by NO_2 is responsible for the corrosion of metals and substantial damage to trees and crops which will adversely affect our economy. NO_2 exposure to plants seriously affect the formation of chlorophyll and thereby reducing the rate of photosynthesis. According to the American Conference of Government Industrial Hygienists, the threshold value of NO_2 gas in air is 3 ppm.

Ammonia is a colourless, reducing gas with a pungent odour. It is alkaline in nature, highly corrosive and dissolves in water to form ammonium hydroxide. Ammonia is a widely used industrial gas for the production of fertilizers, pesticides, explosives, manufacture of plastics, textiles, dyes and other chemicals. This irritating and corrosive gas causes serious respiratory track disorders, skin burns, permanent eye damage or blindness. According to U.S Occupational Safety and Health Administration (OSHA), the maximum limit of ammonia exposure in air for 8 hours is 25 ppm.

1.3.2 Photocatalysis

Organic dyes, pesticides, heavy metal ions etc. constitute a major part of the contaminants. Organic dyes usually co-exist with heavy metal pollutants in waste water bodies. Thus the simultaneous removal of these materials from aqueous medium is also a serious problem we are confronted with. Among the various pollutants, here the concern is focused on Rhodamine B and hexavalent chromium, since chromium is used as a mordant in textile industry.

Rhodamine B, a xanthene dye, is widely used as a colouring agent in textiles and food stuffs. It is highly soluble in water. Regardless of its prevalent applications, it is found to be harmful to the environment and causes various health hazards to human beings. The health hazards of chromium depend on its oxidation state. It exists in two stable oxidation states such as hexavalent and trivalent. Hexavalent chromium is extremely toxic, mutagenic and carcinogenic, while the latter is less toxic and an essential metabolite. Hexavalent chromium is extensively used in electroplating and metal surface processes, inorganic pigment manufacturing, wood processing industry and leather tanning. According to WHO regulations, the maximum concentration of Cr (VI) allowed in drinking water is below 0.05mg/L.

1.4 Zinc oxide as a promising candidate for gas sensing and photocatalytic applications

The emergence of zinc oxide as a photocatalyst and gas sensor is gaining much attention in the current scenario of environmental pollution. Among the various semiconductor metal oxides, zinc oxide is a renowned semiconducting multifunctional material having wide technological applications. The facile fabrication of zinc oxide in various morphologies having multifunctional properties are the advantages of the material. It is a II-VI binary semiconductor metal oxide, whose ionic character lies in between the covalent and ionic semiconductors. Zinc oxide can crystallize in wurtzite, zinc blende and rock salt (NaCl) structures, but the thermodynamically stable phase is wurtzite structure. It is an n-type semiconductor with wide band gap value of 3.37 eV. It has a large exciton binding energy of 60 meV, which ensures the room temperature excitonic emission. The high melting point of zinc oxide (1975° C) indicates its thermal and chemical stability. Besides, the cost effectiveness, environmental friendly nature, availability and the simple fabrication methods make zinc oxide a potential candidate for various commercially important applications.

1.4.1 Morphology and crystal plane dependent activity in zinc oxide

The morphology tuned activity of zinc oxide rely on its size and specific crystal plane orientations. Under ambient conditions, zinc oxide crystallizes in hexagonal wurtzite structure (Figure 6a) with two lattice parameters a= 0.3296 and c= 0.52065 nm. This belongs to the space group C^4_{6v} (Schoenflies notation) and $P6_3mc$ (Hermann–Mauguin notation). In the crystal structure of zinc oxide, each O^{2-} ions is surrounded by four Zn^{2+} ions and vice versa to form a tetrahedral coordination (Figure 6b). This leads to the formation of a non-centro symmetric structure having polar surfaces along the c-axis, which induces piezoelectric characteristics, spontaneous polarization and defect generation in zinc oxide.

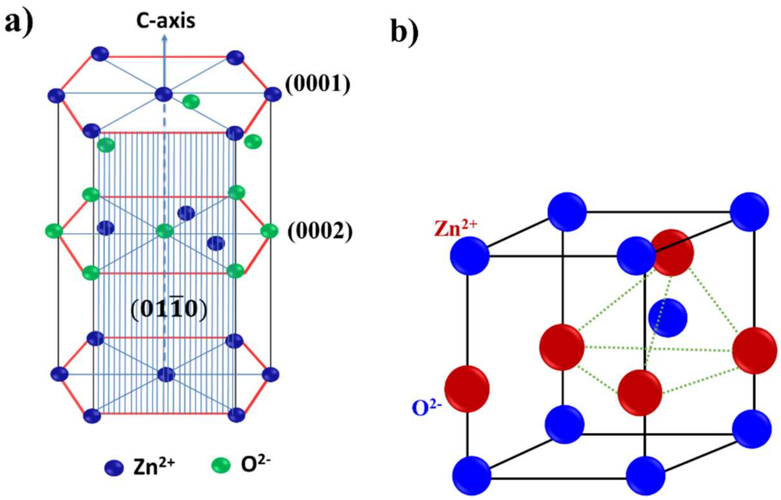

Figure 6. Hexagonal wurtzite structure of zinc oxide (a) and tetrahedral coordination of Zn-O (b).

The crystal planes in hexagonal structures are indexed by Miller-Bravais indices, which has four numbers (*h k i l*). Where *h, k* and *l* are same as that in Miller indices and $i=-(h+k)$. Hence the different planes in zinc oxide can be represented as $\{0001\}$, $\{2\bar{1}\bar{1}0\}$ and $\{01\bar{1}0\}$.

These crystal planes belong to the family of polar and non-polar planes in zinc oxide. The polar surfaces in zinc oxide include the oxygen polar $(000\bar{1})$ and zinc polar (0001) planes. The oxygen polar planes are negative in nature and the zinc polar is positive. Zinc oxide has exceptionally stable polar surfaces. Normally, the polar surfaces undergo reconstruction to get stabilized. But the polar surfaces in zinc oxide i.e., zinc polar (0001) and oxygen polar $(000\bar{1})$ surfaces, are stable, atomically flat and without reconstruction. Surface physicists have been taking efforts to understand the superior stability of the ZnO ± (0001) polar surfaces. The most common non-polar facets composed of equal number of Zn^{2+} and O^{2-} in zinc oxide having low surface energy and are $\{2\bar{1}\bar{1}0\}$ and $\{01\bar{1}0\}$. The intrinsic anisotropy in zinc oxide results growth of crystal along c-axis i.e., in (0001) direction. The normal growth rate in zinc oxide crystal planes follows the order $\{2\bar{1}\bar{1}0\} < \{01\bar{1}0\} < \{0001\}$. Eventually, the crystal planes where higher growth rate occurs will get diminished. Therefore, in the absence of any of the surface directing agents, zinc oxide structures will grow along the c-axis and the resultant morphology will be nanorods having prominent non-polar surfaces due their lower energies. The highly active polar surfaces are responsible for the enhanced activity of ZnO system [53-58].

Different morphological variations of zinc oxide can be achieved by tuning the growth rate along different crystal directions. Morphologically different zinc oxide architectures namely quantum dots, nanoparticles, nanorods, nanosheets, nanowires, nanotubes, nanofibres, nanobelts, nanoneedles, nanoprism, nano/microflowers, nano/microspheres, hollow spheres, nanopyramids, nanotetrapods and nanoplates have been developed by adopting different synthetic conditions.

Current research interests are paid for the development of complex structures by the self-assembly of nano scale building units. Considerable efforts have been taken in this direction for the formation of three dimensional hierarchical micro/nano superstructures by the self-assembly of one dimensional and two dimensional nanostructures such as nanoparticles, nanorods and nanosheets. These hierarchical structures are found to exhibit excellent electronic, optical as well as catalytic properties than their nano-building units. These self-assembled hierarchical structures prevent the agglomeration of particles and augment the quantum efficiency of photocatalysis due to their unique structure and crystal plane orientations.

Morphology and crystal plane dependent activity studies of zinc oxide have been studied by various researchers. Morphology dependant photocatalytic activity has been studied extensively by many researchers [59-61]. Zinc oxide nanodisk has been effectively employed for the degradation of methylene blue in aqueous solution [62]. The photocatalytic degradation of methyl orange over zinc oxide nanorods was discussed by Ghule et al. [63]. Wang et al have proved that zinc oxide with flower like morphology exhibited enhanced activity towards photodegradation of 4-chlorophenol in aqueous solution under UV radiation compared with zinc oxide nanorods [59]. Flower like and grass like zinc oxide hierarchical structures were found to be effective for NO_2 sensing than the commercial zinc oxide. Jin et al. have synthesized porous single crystalline ZnO nanoplates and discussed the synergistic effect of phenol on ZnO for the photoreduction of hexavalent chromium in detail [64]. Kaoilin supported ZnO was used by Siboni et al. and the effect of different factors on photoreduction of Cr(VI) was well studied [65]. Laser induced photoreduction of Cr(VI) using zinc oxide catalyst was studied by Qamar and co-workers [66]. The effect of hole scavengers in the photocatalytic reduction of hexavalent chromium was also studied by various groups [67-70].

Previous reports show that samples with large fraction of polar planes contain more oxygen vacancies and show high catalytic activity [71]. Liu et al have synthesized zinc oxide nano whiskers with exposed reactive (0001) plane for gas sensing application [72]. The effects of exposed crystal planes on the gas sensing property of ZnO was pursued by Xu et al and found that ZnO nanosheets with dominating exposed (0001) facets exhibit superior sensitivity than the (1010) one [73]. A theoretical approach on the adsorption of NO_2 on oxygen deficient surface of zinc oxide has been reported by Breedon et al [74, 75]. The significance of (0001) crystal planes in zinc oxide for gas sensing have been demonstrated by Quin et al [76]. The higher fraction of exposed zinc and oxygen polar planes in zinc oxide contributes to its excellent photocatalytic performance [77]. Zeng et al. reported a higher adsorption of reactive species such as hydroxyl and super oxide radicals on the zinc polar (0001) surface of zinc oxide [78]. This enables the higher rate of photo degradation of organic dyes in zinc oxide with exposed polar facets. Zinc oxide nanosheets films supported on magnetically driven cilia with exposed (0001) polar planes are reported to be highly active photocatalyst.

1.5 Objectives of the present study

The present work has the following objectives:

1. Synthesis of zinc oxide architectures of six morphological variations through a facile low temperature hydrothermal method viz., 1. Nanosheets, 2. Nanorods 3. Nanoparticles, 4. Nanosheet assembled flowers, 5. Nanorods assembled flowers, 6. Nanoparticle assembled flowers.
2. Characterization of the prepared systems using various spectroscopic and analytical techniques. X-Ray Diffraction analysis (XRD), Scanning Electron Microscopy (SEM), Transmission Electron Microscopy (TEM), UV Diffuse Reflectance spectroscopy (UVDRS), Fourier Transform Infra-Red spectroscopy (FTIR), Raman spectroscopy, Photoluminescence spectroscopy, and BET surface area analysis constitute the characterization tools.
3. Gas sensor applications of zinc oxide architectures for the detection of oxidizing gas NO_2 and reducing gas NH_3.
4. Detailed study of various factors influencing the gas sensing property of zinc oxide nanosheets.
5. Photocatalytic reduction of hexavalent chromium using morphologically different zinc oxide structures. Study of factors influencing the photoreduction efficiency of zinc oxide nanoparticles.
6. Photocatalytic degradation of rhodamine B, a cationic dye using morphologically different six zinc oxide architectures.

7. Modification of the nanosheet assembled flower like zinc oxide architectures by loading different weight percentages of copper, iron and silver.
8. Characterization of the modified systems using X-Ray Diffraction analysis (XRD), Scanning Electron Microscopy (SEM), Transmission Electron Microscopy (TEM), UV Diffuse Reflectance spectroscopy (UVDRS), X-ray Photoelectron Spectroscopy (XPS), Photoluminescence spectroscopy, and BET surface area analysis.
9. Photocatalytic degradation of Rhodamine B by the modified systems and identification of the most active system.
10. Concomitant removal of rhodamine B and hexavalent chromium by the most active silver modified zinc oxide sheet assembled flower like structure.

References

1. The environment (protection) act, 1986 Section 2a.
2. L.A. Patil, M.D. Shinde, A.R. Bari, V.V. Deo, Highly sensitive and quickly responding ultrasonically sprayed nanostructured SnO_2 thin films for hydrogen gas sensing, Sens. Actuators B: Chem. 143 (2009) 270.
3. C. Jin, T. Yamazaki, K. Ito, K.T.N. Nakatani, H_2S sensing property of porous SnO_2 sputtered films coated with various doping films, Vacuum 80 (2006) 723.
4. E. Kanazawa, G. Sakai, K. Shimanoe, Y. Kanmura, Y. Teraoka, N. Miura, N. Yamazoe, Metal oxide semiconductor N_2O sensor for medical use, Sens. Actuators B: Chem. 77 (2001) 72.
5. G. Behr, W. Fliegel, Electrical properties and improvement of the gas response in multiple-doped SnO_2, Sens. Actuators B: Chem. 26 (1995) 33.
6. I.S. Hwang, S.-J. Kim, J.-K. Choi, J. Choi, H. Ji, G.T. Kim, Synthesis and gas sensing characteristics of highly crystalline ZnO–SnO_2 core–shell nanowires, Sens. Actuators B: Chem. 148 (2010) 595.
7. J. Gong, Q. Chen, M.-R. Lian, N.-C. Liu, R.G. Stevenson, F. Adami, Macro machined nanocrytalline silver doped SnO_2 H_2S sensor, Sens. Actuators B: Chem. 114 (2006) 32.
8. T. Zhang, L. Liu, Q. Qi, S. Li, G. Lu, Development of microstructure In/Pd-doped SnO2 sensor for low-level CO detection, Sens. Actuators B: Chem. 139 (2009) 287.
9. T. Seiyama, A. Kato, K. Fujiishi, M. Nagatani, A new detector for gaseous components using semiconductive thin film. Anal. Chem. 34 (1962) 1502.

10. T. Y. Chen, H.I. Chen, C.S. Hsu, C.C. Huang, J.S. Wu, P.C. Chou, W.C. Liu, Characteristics of ZnO nanorods-based ammonia gas sensors with a cross-linked configuration, Sens. Actuators B: Chem. 221 (2015) 491.
11. M.A. Chougule, S. Sen, V.B. Patil, Fabrication of nanostructured ZnO thin film sensor for NO_2 monitoring, Ceramics International 38 (2012) 2685.
12. K. Diao, M. Zhou, J. Zhang, Y. Tang, S. Wang, X. Cui, High response to H_2S gas with facile synthesized hierarchical ZnO microstructures, Sensors and Actuators B 219 (2015) 30.
13. X. Chen, J. Liu, X. Jing, J. Wang, D. Song, L. Liu, Self-assembly of ZnO nanosheets into flower-like architectures and their gas sensing properties, Materials Letters112(2013)23.
14. A.S. Kazemi, R. Afzalzadeh, M. Abadyan, ZnO Nanoparticles as Ethanol Gas Sensors and the Effective Parameters on Their Performance, J. Mater. Sci. Technol., 29 (2013) 393.
15. Q. Qi, T. Zhang, Q. Yu, R. Wang, Y. Zeng, L. Liu, H. Yang, Properties of humidity sensing ZnO nanorods-base sensor fabricated by screen-printing, Sensors and Actuators B 133 (2008) 638.
16. B. Cao, J. Chen, X. Tang, W. Zhou, Growth of monoclinic WO_3 nanowire array for highly sensitive NO_2 detection, J. Mater. Chem., 19 (2009) 2323.
17. X.L. Li, T.J. Lou, X.M. Sun, Y.D. Li, Highly Sensitive WO_3 Hollow-Sphere Gas Sensors, Inorg. Chem. 43 (2004) 5442.
18. R. Godbole, V. P. Godbole, P. S. Alegaonkarc, S. Bhagwat, Effect of film thickness on gas sensing properties of sprayed WO_3 thin films, New J. Chem. 41(2017) 11807.

19. S. Elouali, L.G. Bloor, R. Binions, I.P. Parkin, C.J. Carmalt, J.A. Darr, Gas Sensing with Nano-Indium Oxides (In_2O_3) Prepared via Continuous Hydrothermal Flow Synthesis, Langmuir 283 (2012) 1879.
20. J. Tamaki, C. Naruo, Y. Yamamoto, M. Matsuoka, Sensing properties to dilute chlorine gas of indium oxide based thin film sensors prepared by electron beam evaporation, Sens. Actuators B: Chem., 83 (2002) 190.
21. W. Maziarz, A. Kusior, A.T. Zajac, Nanostructured TiO_2-based gas sensors with enhanced sensitivity to reducing gases, Beilstein J. Nanotechnol. 7 (2016) 1718.
22. Q. Hao, L. Li, X. Yin, S. Liu, Q. Li, T. Wang, Anomalous conductivity-type transition sensing behaviors of n-type porous α-Fe_2O_3 nanostructures toward H_2S. Mater. Sci. Eng. B 176 (2011) 600.
23. . X. Gou, G. Wang, J. Yang, J. Park, D. Wexler, Chemical synthesis, characterisation and gas sensing performance of copper oxide nanoribbons. J. Mater. Chem. 18 (2008) 965.
24. . H. Kim, C. Jin, S. Park, S. Kim, C. Lee, H_2S gas sensing properties of bare and Pd-functionalized CuO nanorods. Sens. Actuators B: Chem. 161(2012) 594.
25. H.C. Liang, X.Z. Li, Effects of structure of anodic TiO_2 nanotube arrays on photocatalytic activity for the degradation of 2,3-dichlorophenol in aqueous solution, Journal of Hazardous Materials 162 (2009) 1415.
26. Z.M. Abou-Gamra, M.A. Ahmed, Synthesis of mesoporous TiO_2–curcumin nanoparticles for photocatalytic degradation of methylene blue dye, Journal of Photochemistry & Photobiology, B: Biology 160 (2016) 134.

27. X. Han, Q. Kuang, M. Jin, Z. Xie, L. Zheng, Synthesis of Titania Nanosheets with a High Percentage of Exposed (001) Facets and Related Photocatalytic Properties, J. Am. Chem. Soc., 131 (2009) 3152.
28. C.C. Chen, Degradation pathways of ethyl violet by photocatalytic reaction with ZnO dispersions, J. Mol. Catal. A: Chem. 264 (2006) 82.
29. C.A.K. Gouvêa, F. Wypych, S.G. Moraes, N. Durán, N. Nagata, P. Peralta Zamora, Semiconductor assisted photocatalytic degradation of reactive dyes in aqueous solution, Chemosphere 40 (2000) 433.
30. A. Akyol, H.C. Yatmaz, M. Bayramoglu, Photocatalytic decolourization of Remazol Red RR in aqueous ZnO suspensions, Appl. Catal. B: Environ. 54 (2004) 19.
31. S. Sakthivel, B. Neppolian, M.V. Shankar, B. Arabindoo, M. Palanichamy, V. Murugesan, Solar photocatalytic degradation of azo dye: comparison of photocatalytic efficiency of ZnO and TiO_2, Sol. Energy Mater. Sol. Cells 77 (2003) 65.
32. C. Lizama, J. Ferrer, J. Baeza, H.D. Mansilla, Optimized photodegradation of reactive blue 19 on TiO_2 and ZnO suspensions, Catal. Today 76 (2002) 235.
33. I. Poulios, I. Tsachpinis, Photodegradation of the textile dye Reactive Black 5 in the presence of semiconducting oxides, J. Chem. Technol. Biotechnol. 74 (1999) 349.
34. B. Neppolian, S. Sakthivel, B. Arabindoo, M. Palanichamy, V. Murugesan, Degradation of textile dye by solar light using TiO_2 and ZnO photocatalysts, J. Environ. Sci. Health A Tox. Hazard. Subst. Environ. Eng. 34 (1999) 1829.

35. V. Kandavelu, H. Kastien, K.R. Thampi, Photocatalytic degradation of isothiazolin-3-ones in water and emulsion paints containing nanocrystalline TiO_2 and ZnO catalysts, Appl. Catal. B: Environ. 48 (2004) 101.
36. P. Percherancier, R. Chapelon, B. Pouyet, Semiconductor-sensitized photodegradation of pesticides in water: the case of carbetamide, J. Photochem. Photobiol. A: Chem. 87 (1995) 261.
37. A.A. Khodja, T. Sehili, J.F. Pihichowski, P. Boule, Photocatalytic degradation of 2-phenylphenol on TiO_2 and ZnO in aqueous suspensions, J. Photochem. Photobiol. A: Chem. 141 (2001) 231.
38. I. Poulios, M. Kositzi, A. Kouras, Photocatalytic decomposition of triclopyr over aqueous semiconductor suspensions, J. Photochem. Photobiol. A: Chem. 115 (1998) 175.
39. G. Colón, M.C. Hidalgo, J.A. Navío, E. Pulido Melián, O. González Díaz, J.M. Do˜na Rodríguez, Highly photoactive ZnO by amine capping assisted hydrothermal treatment, Appl. Catal. B 83 (2008) 30.
40. F. Xu, P. Zhang, A. Navrotsky, Z.-Y. Yuan, T.-Z. Ren, M. Halasa, B.-L. Su, Hierarchically assembled porous ZnO nanoparticles: synthesis, surface energy, and photocatalytic activity, Chem. Mater. 19 (2007) 5680
41. Y. Wang, X. Li, N. Wang, X. Quan, Y. Chen, Controllable synthesis of ZnO nanoflowers and their morphology-dependent photocatalytic activities, Sep. Purif. Technol. 62 (2008) 727.
42. B. Li, Y. Wang, Facile synthesis and enhanced photocatalytic performance of flower-like ZnO hierarchical microstructures, J. Phys. Chem. C 114 (2010) 890–896.

43. G. Ren, D. Hu, E.W. Cheng, M.A. Vargas-Reus, P. Reip, R.P. Allaker, Characterisation of copper oxide nanoparticles for antimicrobial applications. Int. J Antimicrob. Agents. 33 (2009) 587.
44. D. Vaidehi, V. Bhuvaneshwari, D. Bharathi, B.P. Sheetal, Antibacterial and photocatalytic activity of copper oxide nanoparticles synthesized using *solanum lycopersicum* leaf extract, Mater. Res. Express, 5 (2018).
45. E.E. Mbu, D. Dodoo-Arhin, S.K. Ntwampe, E. Malenga, E. Fosso-Kankeu, Photocatalytic Degradation of Azo and Rhodamine Dyes Using Copper (II) Oxide Nanoparticles, 10th Int'l Conference on Advances in Science, Engineering, Technology & Healthcare (ASETH-18) Nov. 19-20, 2018.
46. K. Sayama, H. Hayashi, T. Arai, M. Yanagida, T. Gunji, H. Sugihara, Highly active WO3 semiconductor photocatalyst prepared from amorphous peroxo-tungstic acid for the degradation of various organic compounds, Appl. Catal. B: Environ. 94 (2010) 150.
47. Liu H, Peng T, Ke D, Peng Z and Yan C, Preparation of photocatalytic activity of dysprosium doped tungsten trioxide nanoparticles. Mater Chem Phys 104 (2007) 377.
48. Purwanto A, Widiyandari H, Ogi T and Okuyama K, Role of particle size for platinum-loaded tungsten oxide nanoparticles during dye photodegradation under solar-simulated irradiation. Catal Commun 12 (2011)525.
49. Cho IS, Kwak CH, Kim DW, Lee S and Hong KS, Photophysical, photoelectrochemical, and photocatalytic properties of novel SnWO4 oxide semiconductor with narrow band gaps. J Phys Chem C 113 (2009) 10647.

50. Ungelenk J and Feldmann C, Nanoscale β-$Sn_{1-n}WO_4$ · nα-Sn – a highly efficient photocatalyst for daylight-driven degradation of organic dyes and its real ‘green’ synthesis. Appl Catal B – Environ 102 (2011) 515.
51. Sajjad AKL, Shamaila S, Tian B, Chen F and Zhang J, One step of WO_3/TiO_2 nanocomposites with enhanced photocatalytic activity. Appl Catal B – Environ 91 (2009) 397.
52. Sajjad AKL, Shamaila S, Tian B, Chen F and Zhang J, Comparative studies of operational parameters of degradation of azo dyes in visible light by highly efficient WO_x/TiO_2 photocatalyst. J Hazard Mater 177 (2010) 781.
53. S.A. Chevtchenko, J.C. Moore, U. O ¨ zgu¨r, X. Gu, A.A. Baski, H. Morkoc, B. Nemeth, J.E. Nause, Comparative study of the (0001) and (000) surfaces of ZnO. Appl. Phys. Lett. 89 (2006) 182111.
54. J. Lahiri, S. Senanayake, M. Batzill, Soft X-ray photoemission of clean and sulfur covered polar ZnO surfaces: a view of the stabilization of polar oxide surfaces. Phys. Rev. B 78, 155414 (2008).
55. O. Dulub, U. Diebold, G. Kresse, Novel stabilization mechanism on polar surfaces: ZnO(0001)-Zn. Phys. Rev. Lett. 90 (2003) 016102.
56. P.S. Bagus, F. Illas, G. Pacchioni, F. Parmigiani, Mechanisms responsible for chemical shifts of core level binding energies and their relationship to chemical bonding. J. Electron. Spectrosc. Relat. Phenom. 100(1–3), 215–236 (1999).
57. G. Kresse, O. Dulub, U. Diebold, Competing stabilization mechanism of the polar ZnO (0001)-Zn surface. Phys. Rev. B 68, 245409 (2003).
58. A. O¨ nsten, D. Stoltz, P. Palmgren, S. Yu, M. Go¨thelid, U.O.Karlsson, Water adsorption on ZnO(0001): transition from

triangular surface structure to a disordered hydroxyl terminated phase. J. Phys. Chem. C, 114 (2010)11157.

59. Y. Wang, X. Li, N. Wang, X. Quan and Y. Chen, Controllable synthesis of ZnO nanoflowers and their morphology-dependent photocatalytic activities, Sep. Purif. Technol. 62 (2008) 727.
60. A. Mc Laren, T. Valdes-Solis, G. Li, S.C. Tsang, Shape and size effects of ZnO nanocrystals on photocatalytic activity, J. Am. Chem. Soc. 131 (2009) 12540.
61. D. Li and H. Haneda, Morphologies of zinc oxide particles and their effects on photocatalysis, Chemosphere 51 (2003) 129.
62. K. Sini, B. Satpati , M. Satyabrata, Enhanced photocatalytic activity of Co doped ZnO nanodisks and nanorods prepared by a facile wet chemical method, Phys. Chem. Chem. Phys. 16 (2014) 12741.
63. L. A. Ghule, A. A. Patil, K. B. Sapnar, S. D. Dhole, K. M. Garadkar, Photocatalytic degradation of methyl orange using ZnO nanorods, Toxicol. Environ. Chem. 93 (2011) 623.
64. Z. Jin , Y.X. Zhang, F.L. Meng, Y. Jia, T. Luo, X.Y. Yu, J. Wanga, J.H. Liua, X.J. Huang, Facile synthesis of porous single crystalline ZnO nanoplates and their application in photocatalytic reduction of Cr(VI) in the presence of phenol, J. Hazard. Mater. 276 (2014) 400.
65. M.S. Siboni, M. Farrokhi, R.D.C. Soltani, A. Khataee, S. Tajassosi, Photocatalytic reduction of hexavalent chromium over ZnO nanorods immobilized on kaolin, Ind. Eng. Chem. Res. 53 (2014) 1079.
66. M. Qamar, M.A. Gondal, Z.H. Yamani, Laser-induced efficient reduction of Cr(VI) catalyzed by ZnO nanoparticles, J. Hazard. Mater. 187 (2011) 258.
67. P. Banerjee, S. Chakrabarti, S. Maitra, B.K. Dutta, Zinc oxide nanoparticles- sonochemical synthesis, characterization and

application for photo-remediation of heavy metal, Ultrason. Sonochem. 19 (2012) 85..

68. S. Chakrabarti, B. Chaudhuria, S. Bhattacharjee, A.K. Rayb, B.K. Dutta, Photo-reduction of hexavalent chromium in aqueous solution in the presence of zinc oxide as semiconductor catalyst, Chem. Eng. J. 153 (2009) 86.
69. S. Challagulla, R. Nagarjuna, R. Ganesan, S. Roy, Acrylate-based polymerizable sol−gel synthesis of magnetically recoverable TiO2 supported Fe3O4 for Cr(VI) photoreduction in aerobic atmosphere, ACS Sustainable Chem. Eng. 4 (2016) 974−982.
70. M.N. Joubani, M.S. Siboni, J.K. Yang, M. Gholami, M. Farzadkia, Photocatalytic reduction of hexavalent chromium with illuminated ZnO/TiO2 composite, J. Ind. Eng. Chem. 22 (2015) 317.
71. G. R. Li, T. Hu, G. L. Pan, T. Y. Yan, X. P. Gao, H. Y. Zhu, Morphology-Function Relationship of ZnO: Polar Planes, Oxygen Vacancies, and Activity, J. Phys. Chem. C, 112 (2008) 11859.
72. J. Liu, X. Chen, W. Wang, Y. Liu, Q. Huang, Z.Guo, Self-assembly of [10-10] grown ZnOnanowhiskers with exposed reactive (0001) facets on hollow spheres and their enhanced gas sensitivity, Cryst.Eng.Comm. 13 (2011) 3425.
73. J. Xu, Z.Xue, N. Qin, Z. Cheng, Q. Xiang, The crystal facet-dependent gas sensing properties of ZnOnanosheets: Experimental and computational study, Sens. Actuators B 242 (2017) 148.
74. M. Breedon, M.J.S. Spencer, I. Yarovsky, Adsorption of NO and NO2 on the ZnO (2-1-10) surface: A DFT study, Surf. Sci. 603 (2009) 3389.

75. M. Breedon, M. J. S. Spencer, I. Yarovsky, Adsorption of NO2 on Oxygen Deficient ZnO (2-1-10) for Gas Sensing Applications: A DFT Study, J. Phys. Chem. C 114 (2010) 16603.
76. N.Qin, Q. Xiang, H. Zhao, J. Zhanga, J. Xu, Evolution of ZnO microstructures from hexagonal disk to prismoid, prism and pyramid and their crystal facet-dependent gas sensing properties, Cryst. Eng. Comm, 16 (2014) 7062.
77. R. Boppella, K. Anjaneyulu, P. Basak, S.V. Manorama, Facile Synthesis of Face Oriented ZnO Crystals: Tunable Polar Facets and Shape Induced Enhanced Photocatalytic Performance, J. Phys. Chem. C 117 (2013) 4597.
78. J.H. Zeng, B.B. Jin, Y.F. Wanga, Facet enhanced photocatalytic effect with uniform single-crystalline zinc oxide nanodisks, Chemical Physics Letters 472 (2009) 90.
79. F. Penga, Q. Zhou, C. Lu, Y. Ni, J. Koua, Z. Xu, Construction of (001) facets exposed ZnO nanosheets on magnetically driven cilia film for highly active photocatalysis, Applied Surface Science 394 (2017) 115.

Chapter 2

Experimental Procedure and Characterization Techniques

2.1 Introduction

Metal oxide nano/microstructures are prepared through various physical and chemical routes. The properties of the material rest on the synthetic strategies adopted and the fine elucidation of the properties of the material can be done using different analytical and spectroscopic techniques. In this chapter, we will describe the method of preparation of catalyst systems, materials used for this purpose, various characterization techniques used to analyse the systems and the experimental details of application studies viz, gas sensing and photocatalysis are presented.

2.2 Materials

The reagents used for the preparation of zinc oxide architectures and the application studies were of analytical grade and were used without further purification.

Sl.No.	Chemicals/Reagents	Company
1.	Zinc oxide	Merck
2.	Zinc nitrate hexahydrate	Sigma Aldrich
3.	Cetyltrimethyl ammoniumbromide (CTAB)	Sigma Aldrich
4.	Hexamethylene tetramine (HMTA)	Sigma Aldrich
5.	Poly vinyl pyrrolidone K-30 (PVP)	Sigma Aldrich
6.	Sodium hydroxide (NaOH)	Sigma Aldrich
7.	Silver nitrate	Sigma Aldrich
8.	Copper nitrate	Sigma Aldrich
9.	Ferric nitrate	Sigma Aldrich

10.	Titanium dioxide	Sigma Aldrich
11.	NO_2 gas	Chemtron India Ltd.
12.	NH_3 gas	Chemtron India Ltd.
13.	Rhodamine B	Himedia
14.	Methylene blue	Merck
15.	Potassium dichromate	Merck
16.	Sulphuric acid	Merck
17.	Ferroin indicator	Merck
18.	Ferrous ammonium sulphate	Merck
19.	Silver sulphate	Merck
20.	Mercuric sulphate	Merck
21.	Methanol	Merck
22.	Phenol	Merck
23.	Ethanol	Merck
24.	Acetone	Merck
25.	Hydrochloric acid	Merck
26.	Ammonium oxalate	Himedia
27.	Isopropanol	Merck
28.	Ethylene diamine tetraacetic acid	Merck

2.3 Synthesis of zinc oxide architectures

The hierarchical flowerlike structures and their nanobuilding units were prepared via low temperature hydrothermal method in the presence and absence of different surfactants.

2.3.1 Synthesis of nanosheets assembled flower like zinc oxide structures (ZSF)

Nanosheets assembled flower like structures were prepared by mixing solutions of 0.6 M NaOH and 0.0025 M CTAB with 0.1M zinc nitrate hexahydrate ($Zn(NO_3)_2.6H_2O$) solution. The obtained mixture was stirred for 2 hours. After the completion of vigorous stirring, the resultant solution was transferred to a 500mL Teflon lined stainless steel autoclave and kept in an air oven at 90°C for 15hrs. The white products obtained were washed consecutively with water and ethanol for four times and dried in an oven at 80°C. The final products were calcined at 400°C for 2 hrs. The obtained sample was represented as ZSF.

2.3.2 Synthesis of nanorods assembled flower like zinc oxide structures (ZRF)

Flowerlike structures with nanorods as constituent units were prepared using the aforementioned method without using CTAB. Herein we have used 0.6 M NaOH and 0.1 M zinc nitrate hexahydrate for the synthesis. The mixed solutions were vigorously stirred for 2 hours. After that it was transferred to a 500 mL Teflon lined stainless steel autoclave and kept in an air oven at 90°C for 15hrs. The obtained white products were washed with deionized water for several times and dried in an oven at 80°C. The final products were calcined at 400°C for 2 hrs. The obtained sample was represented as ZRF.

2.3.3 Synthesis of nanoparticles assembled flower like zinc oxide structures

Nanoparticles assembled flowers (ZPF) were prepared by the same manner as that of ZRF, except that the reaction time was adjusted to 3 hours. In detail, 0.6 M NaOH and 0.1 M zinc nitrate hexahydrate for the synthesis.

The mixed solutions were vigorously stirred for 2 hours. After that it was transferred to a 500 mL Teflon lined stainless steel autoclave and kept in an air oven at 90ºC for 3 hrs. The obtained white products were washed with deionized water for several times and dried in an oven at 80ºC. The final products were calcined at 400ºC for 2 hrs. The obtained sample was represented as ZPF.

2.3.4 Synthesis of zinc oxide nanosheets (ZS)

Zinc oxide nanosheets were prepared by the following route. A mixture of NaOH (0.6 M) and CTAB (0.0025 M) in deionized water was stirred vigorously for 15 minutes. 0.1 M zinc nitrate hexahydrate ($Zn(NO_3)_2.6H_2O$) solution was added to the above mixture drop by drop and was stirred for 2 hours. The resultant solution was transferred to a 500mL Teflon lined stainless steel autoclave and kept in an air oven at 90ºC for 3 hours. The obtained white precipitate were washed consecutively with water and ethanol for four times and dried in an oven at 80ºC. The final products were calcined at 400ºC for 2 hrs. The obtained sample was represented as ZS.

2.3.5 Synthesis of zinc oxide nanoparticles

Zinc nitrate hexahydrate (0.1 M) and polyvinylpyrrolidone (PVP) were separately dissolved in deionized water. The two solutions were mixed thoroughly and NaOH (0.6 M) solution was slowly added to the above mixture. The reaction mixture was transferred to a 500 mL Teflon lined autoclave and was kept in an oven at 90^0 C for 15 hours. The precipitate obtained was washed with de-ionised water and acetone to remove excess PVP. The final product was dried at 80^0C for overnight and was ground to form a fine powder. The oxide powder was then subjected to calcination at 400º C for 2 hours and the catalyst system was labelled as ZP.

2.3.6 Synthesis of zinc oxide nanorods

The precursors for the synthesis were Zinc nitrate hexahydrate ($Zn(NO_3)_2.6H_2O$) and hexamethylenetetramine ($C_6H_{12}N_4$). The hydrothermal reaction solution was prepared by mixing an equimolar quantity of $Zn(NO_3)_2.6H_2O$ and hexamine. The solution was kept in a laboratory oven at 90^0 C for 15 hours. After the completion of the reaction, the white product obtained was washed with DI water and ethanol several times. It was then dried in an oven at 80^0C. The dried samples were ground well and calcined at 400° C for 2 hours. The system was denoted as ZR.

2.4 Modification of ZSF system for photocatalytic applications

2.4.1 Preparation of copper, iron and silver modified analogues of ZSF system

For further tuning the photocatalytic properties of zinc oxide nanosheets assembled flower like architectures, we have incorporated copper, iron and silver as the foreign materials. Wet impregnation and photochemical deposition were adopted for this purpose. 0.2 g zinc oxide was stirred with 0.003 M solutions of copper nitrate trihydrate , ferric nitrate nonahydrate and silver nitrate in deionized water separately in three beakers for two hours. After the thorough stirring, the solid product was separated by centrifugation. The obtained product was washed with deionized water for several times and dried in an oven at 80° C. The dried samples were calcined at 400° C for 2 hours. The catalyst were denoted as AgZSF, CuZSF and FeZSF for silver, copper and iron modified ZSF system.

2.4.2 Modification of zinc oxide nanosheets assembled flowerlike architectures (ZSF system) with different weight percentages of silver

Different weight percentages (1%, 3%, 5% and 7%) of silver modified analogues of zinc oxide were prepared by stirring 0.2 g zinc oxide with 0.001 M, 0.003 M, 0.005 M and 0.007 M silver nitrate solution in deionized water for 2 hours. Washed and centrifuged to get a greyish product which then dried in an oven at 80^{o} C. The four samples were calcined at 400^{o} C for two hours. The obtained catalyst powders were represented as 1AgZSF, 3AgZSF, 5AgZSF and 7AgZSF respectively for 1, 3, 5 and 7 weight percentages of silver modified zinc oxide systems.

2.5 Characterization tools

The characterization of the prepared zinc oxide systems were done using various analytical and spectroscopic techniques such as:

- X-Ray diffraction technique (XRD)
- Transmission electron microscopy (TEM)
- Field emission scanning electron microscopy (FESEM)
- Raman spectroscopy
- Ultra violet-visible diffuse reflectance spectroscopy (UV-Vis DRS)
- Photoluminescence spectra (PL)
- Fourier transmission of infra-red spectra (FTIR)
- Brunauer- Emmett -Teller (BET) Surface area analysis
- X-ray photoelectron spectroscopy(XPS)

The fundamental working principles of the aforementioned techniques are briefly described below.

2.5.1 X-ray diffraction analysis (XRD)

X-ray diffraction is a tool not only for structural investigation, but also can be implemented for calculation of particle size, stress measurements and determination of orientation etc. of materials. The mathematical expression for X-ray diffraction is derived by Bragg and his son. There must exist a definite phase relationships between the X-rays and atoms in the sample, because the atoms are arranged periodically in the lattice. The phase relations are in such a way that destructive interference takes place in most directions of scattering and constructive interference takes place in few directions forming diffracted beams. The two significant geometric facts to be considered while dealing with Bragg's law are:

i. The incident beam, the normal to the reflecting plane, and the diffracted beam are always coplanar.

ii. The diffraction angle, which is the angle between the diffracted beam and transmitted beam is always 2θ.

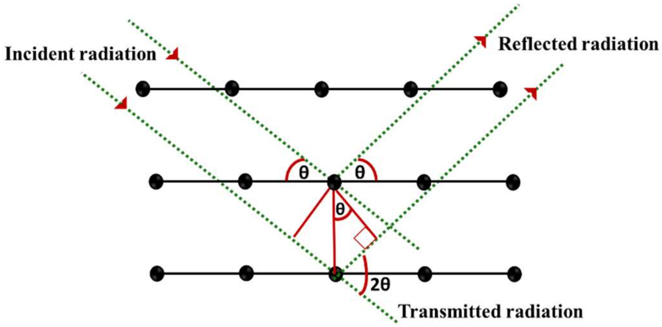

Figure 1. Bragg diffraction from a set of crystal planes.

The Bragg's diffraction from a set of crystal planes is shown in Figure 1. The diffraction of monochromatic X-rays takes place only at those particular angles of incidence which satisfy the Bragg's law. Bragg's law can be mathematically expressed as;

$$n\lambda = 2d \sin\theta$$

Where ' λ' is the wavelength of the radiation used,'d' is the interplanar spacing, 'θ' is the angle between diffracted beam and the relevant crystal plane and 'n' is the order which is often unity. By measuring the angle ' θ ', the interplanar spacing'd' can be calculated, provided the wavelength of X-ray is known.

Besides, XRD can be used to determine the crystallite size of the sample. The simplest approach is to use the Scherer equation. The crystallite size by the Scherrer's formula:

$$D = \frac{0.9\lambda}{\beta cos\theta} ,$$

Where D is crystallite size, λ is the wavelength of the radiation, β stands for the full width half maxima (in radians) and θ represents the angle (in degrees) at which the highest intense peak appears.

The size calculated from X-ray diffraction analysis can be related to the size of the individual crystals, rather than the size of particles formed from the agglomeration of these crystals in the sample. In the present work, the crystal phase and crystallinity of the samples were investigated by Rigaku Miniflex 600 diffractometer (Cu-Kα radiation) equipped with a rotating anode to characterize the crystalline nature of the systems.

2.5.2 Field emission scanning electron microscopy (FESEM)

The field emission scanning electron microscopy (FESEM) analysis is a technique used for studying the surface morphology of the samples. A focused beam of electrons is used to generate an image. The important components of this analytical technique are electron gun, electronic lenses, scanning coil, sample, and detector. The electron gun produces low and high energy electron beams ensuing in both enhanced spatial resolution and reduced sample damage. The primary electrons thus generated are accelerated in a high electric field gradient. The beam of electrons are deflected and focused by the electronic lenses present in the system produce a narrow beam which bombards the object resulting in the generation of secondary electrons (SE) from the sample. The detector monitor these secondary electrons and produces an electronic signal, finally converted into an image. The surface morphology of the samples in the present study was analysed using JEOL Model JSM-6390LV scanning electron microscope. Figure 2 displays the schematic diagram of field emission scanning electron microscopy.

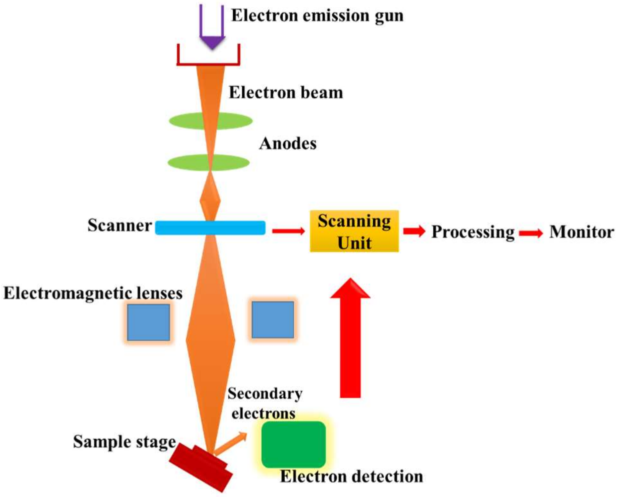

Figure 2. A schematic representation of field emission scanning electron microscopy.

2.5.3 Transmission electron microscopy (TEM)

Transmission electron microscopy (TEM) is a microscopic technique where a beam of high energy electrons is transmitted through a sample to make an image. When electron beam passes through a thin section of the sample material, it reacts with atoms of the sample and are scattered. A sophisticated system of electromagnetic lenses focuses the scattered electrons into an image or a diffraction pattern depending on the mode of working. Figure 3 shows the path of the electron beam in a transmission electron microscope. Selected area electron diffraction pattern (SAED) is a unique technique in TEM, in which the diffraction pattern obtained from a selected area of the sample offers an exceptional capability to decide the lattice parameter and crystal symmetry. The 'd' spacing of the planes can be determined by the following equation;

$$Rd=L\lambda$$

Where L is the effective camera length, λ is the de Broglie wavelength of the accelerating electrons, R is the ring radius of a standard electron diffraction pattern, and d is the interplanar spacing. In the present study, TEM (FEI TECNAI 30 G2, 300KV) was used.

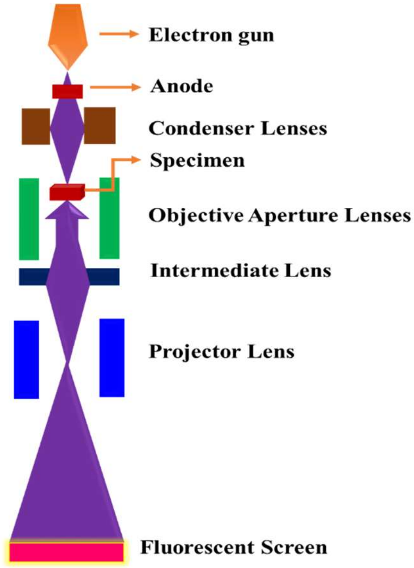

Figure 3. Schematic diagram showing the path of the electron beam in transmission electron microscope.

2.5.4 Raman spectroscopy

This spectroscopic technique is based on the inelastic scattering of monochromatic light, generally from a laser source. The incident photons from the laser source interact with the vibrating molecules of the sample and create a scattered light. The frequency of the scattered photons is moved up or down in agreement with the frequency of the incident radiation. This shift in frequency provides information about the vibrational, rotational and other low frequency transitions within the molecule.

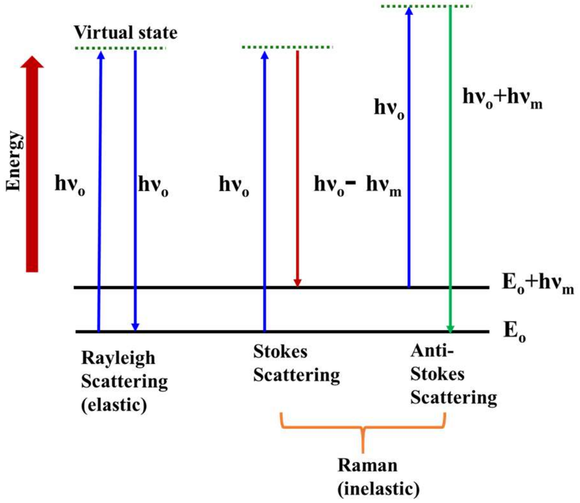

Figure 4. Jablonski diagram of Rayleigh and Raman process.

A monochromatic radiation of frequency 'υ_o' when incident on a non-absorbing medium, most of the radiation is transmitted through the medium without any change, and some of it is scattered. The analysis of the scattered radiations, a small portion of the scattered energy will be found at frequencies $\acute{\upsilon}=\upsilon_o\pm\upsilon_m$. The displaced frequencies are associated with the transitions between vibrational, rotational, and electronic levels of the molecular systems. The scattering of radiation without any change in frequencies is called Rayleigh scattering and that with change in the frequency is called Raman scattering. Raman scattering is always accompanied by Rayleigh scattering. Stokes lines are raman lines at wave numbers less than the incident wave number (υ_o- υ_m). Anti- Stokes lines are wave numbers greater than υ_o, (υ_o+υ_m). The frequency shifts of the Raman lines, their polarization and intensity are characteristics of the scattering substance. Normally, Stokes lines are considered for analysis because anti-

Stokes lines are much weaker than Stokes lines. The levels involved in the Raman spectra are shown in Figure 4. In the present work, Raman spectra of the prepared systems were recorded using Bruker multi Ram FT-NIR spectrometer with Nd-YAG Laser source (1064nm).

2.5.5 Ultra violet-visible diffuse reflectance spectroscopy (UV-Vis DRS)

UV-Visible reflectance spectroscopy is an ideal tool for the examination of electronic states of a material. When a light radiation incident on the material surface, a part of the radiation is absorbed, reflected, transmitted or scattered. In diffuse reflectance spectroscopy, the reflected or scattered light is analysed. The total reflectance from the material surface depends on particle size and microstructural characterisations. The diffuse reflectance is the scattering of incident ray from a polished surface in multiple angles rather than the specular reflection i.e., in a single angle which is represented in Figure 5.

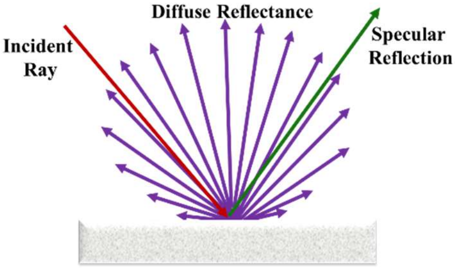

Figure 5. Diffuse reflectance from a smooth surface.

According to Lambert’s equation, the energy absorbed by a surface which shows negligible reflection is given as,

$$I = Io\exp(-\alpha t)$$

Where, Io and I are incident and transmitted intensities respectively.

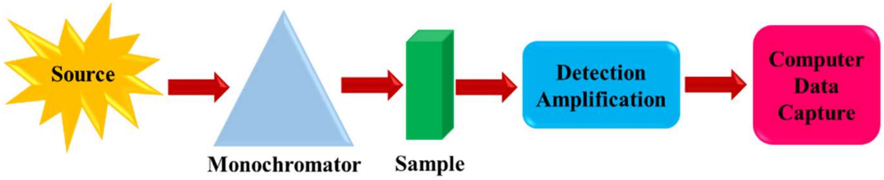

Figure 6. Schematic representation of the simple instrumentation of UV-visible spectrophotometer

Figure. 6 displays the schematic illustration for the simple instrumentation of a UV-visible spectrometer. Deuterium arc lamp is used as the source radiation, which gives a continuous spectrum below 400 nm. In order to select the wavelength at which absorption measurement is to be taken, a monochromator is used.

The band gap determination from diffuse reflectance spectra can be done using the expression proposed by Kubelka and Munk. The Kubelka-Munk expression is as follows:

$$\frac{k}{s} = \frac{(1 - R\infty)^2}{2R\infty} \equiv F(R\infty)$$

Where $F(R\infty)$ is the Kubelka-Munk function, k, the absorption coefficient, s is scattering coefficient and $R\infty$ represents the ratio of sample reflectance to the reflectance of reference. Band gap of the material can be obtained from the expression;

$$\alpha h\nu = C(h\nu - Eg)^n$$

Where ‘α’ represents the absorption coefficient and $h\nu$ is the energy of photon. C is a constant. The value of n=2 for directly allowed transition and that for indirect transition is n=1/2. In the case of direct band gap semiconductor like ZnO, the equation for band gap determination can be written as;

$$\alpha h\nu = C(h\nu - Eg)^2$$

UV–visible absorption spectra of the samples were recorded in the wavelength range of 200 to 800 nm using Jasco V-550 spectrophotometer in diffuse reflectance mode using $BaSO_4$ as reference.

2.5.6 Photoluminescence spectroscopy

Photoluminescence (PL) spectroscopy is a potential tool for the optical characterization of semiconductor materials. This non-invasive technique used for the identification of band gap, point defects etc., The electrons in the valence band are excited by light photons of energy $h\nu$. The excited electron undergo several radiative and non-radiative transitions to come back to the ground level. The radiative transitions from conduction band to valence band results in the luminescence spectra, which corresponds to the band gap of the material. The photoluminescence measurement is used to resolve information on band gap, recombination process, impurity levels and surface structure and excited levels in the semiconductor materials. In the present work, the photoluminescence emission spectrum was measured using RF-5301 PC- Shimadzu spectrofluorophotometer at room temperature following excitation at λ= 325nm.

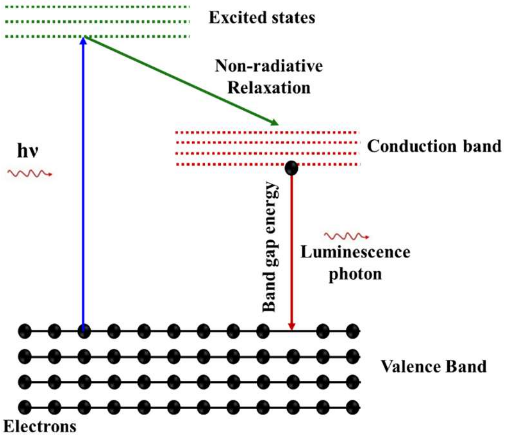

Figure 6: Schematic diagram of photoluminescence excitation

2.5.7 Fourier transform infrared spectroscopy (FTIR)

This technique is a preferred method in infrared spectroscopy, which is very significant to understand the molecular absorption and transmission characteristics. It is a non-destructive and simple method compared to various analytical techniques. Every molecule has characteristic vibrational energy levels and upon absorption of suitable energy results in corresponding transitions. The selection rule for the vibrational transition is that the dipole moment of the molecule must change ($\Delta v = \pm 1$) during molecular vibration. IR spectrum is characteristic of each molecule. The quantized vibrational energy of the molecule is represented as,

$$E_{vib} = (v + \frac{1}{2})h\nu.$$

Where, 'v' is the vibrational quantum number and can have the values v = 0, 1, 2, 3…etc. 'h' is the Planks constant and $'\nu'$ is the vibrational frequency of the chemical bond.

FTIR spectroscopy provide the structural and vibrational characteristics of the molecule. It gives an idea about the nature of the functional groups on the surface of sample and also the presence of various active adsorption sites. The intensity of vibrational peaks is an indication of the quantity of the specific moiety present in the sample mixture. With the help of advanced algorithms it is an efficient tool for quantitative analysis. The experimental set up consists of the following parts: IR source, sample holder, interferometer, a detector and a computer. IR source of wave number range 4000-400 cm^{-1} is used for recording the spectrum. The radiation is then passed through a beam splitter, where the encoding of the signal takes place. The emitted signal is passed through the sample and the transmitted light is measured by the detector and ultimately transferred to the computer. The sample preparation was done by solid potassium bromide (Sigma Aldrich FTIR grade), by grinding 200 mg KBr with 20 mg sample powder. The transparent pellet is placed in the sample holder to transmit IR radiation. The intensity of the transmitted radiation is measured by the detector.

In the present work, the FTIR spectra of the prepared samples were recorded using Jasco FTIR- 4100 spectrometer by KBr disc method.

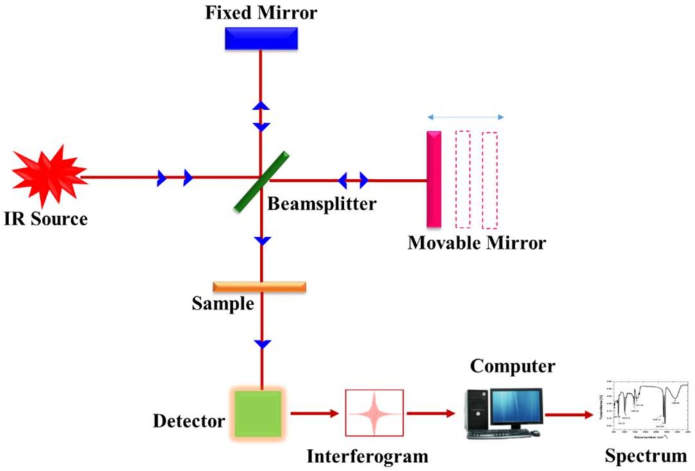

Figure 7. Schematic diagram of experimental set up for FTIR analysis

2.5.8 BET Nitrogen adsorption surface area analysis

BET Nitrogen adsorption surface area analysis is an efficient technique for the measurement of specific surface area of nanomaterials. Brunauer Emmet and Teller theory (BET theory) is an extension of Langmuir adsorption theory, in which the surface area of the material can be measured from the volume of adsorbed gas (N_2 gas at 77K) on the surface. The nitrogen (N_2) molecule is chemically inert and has the strong adsorption ability to form multilayer adsorption on most of the solid surfaces. The BET study provides information about micro, meso and macroporous structures due to the suitable wide range of relative pressures and wide acceptance of the cross sectional area. BET equation is derived on the basis of some general assumptions (1)The surface is homogeneous (2)There is no interaction between adsorbed molecules (3) Multilayer adsorption(4) Except for the first layer is heat of adsorption and higher layer is heat of condensation. At saturated pressure of the adsorbed gas the number of layer is infinite.

BET equation for multilayer adsorption is represented as,

$$\frac{\mathrm{P}}{(\mathrm{Po}-\mathrm{P})\mathrm{V}} = \frac{1}{\mathrm{CVm}} + \frac{\mathrm{C}-1}{\mathrm{CVm}}\frac{\mathrm{P}}{\mathrm{Po}},$$

Here the terms P/P_o represents the relative pressure of the adsorbed gas, 'C' is the BET constant related to the interaction between solid and the adsorbed gas molecules, V is the volume of gas adsorbed and Vm volume of gas for monolayer adsorption. Straight line is obtained by plotting $P/(P_o-P)V$ against P/P_o [Figure 8]. From the slope and intercept of the straight line the value of V_m can be calculated.

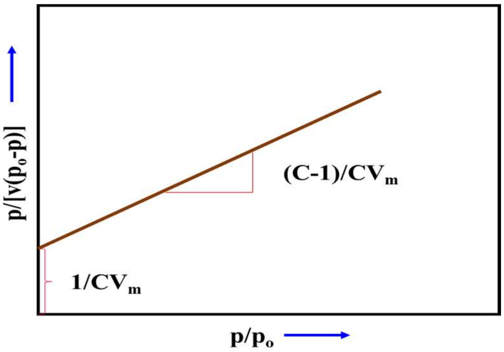

Figure 8. BET adsorption isotherm by plotting p/p_o against $p/v(p_o-p)$

In the present work, surface area of the samples was analysed by Micromeritics Gemini surface area analyzer using nitrogen adsorption at 77K.

2.5.9 X-ray Photoelectron Spectroscopy (XPS)

X-ray photoelectron spectroscopy (XPS) is an efficient technique for the analysis of surface states of the material. It is also known as Electron Spectroscopy for Chemical Analysis (ESCA). The analysis technique can be applied to a wide range of materials.

The fundamental principle of XPS analysis is photoelectric effect. X-ray photons of energy, $h\nu$, when incident on the surface of a material, photoelectrons from the inner core shell of the material is ejected. The kinetic energy of the ejected electrons equal to; Kinetic Energy= $h\nu - BE$; where BE stands for the binding energy of the ejected photoelectron. No two electrons in the periodical table have the same electron energy levels, thus it is possible to get the elemental combination of the material from XPS analysis. Furthermore, the oxidation state of the elements, empirical formula of the material, surface contaminants etc., can also be identified form X-ray photoelectron spectroscopy. The surface analysis depth of XPS measurements is approximately 5 nm, which is higher than that of SEM/EDS analysis.

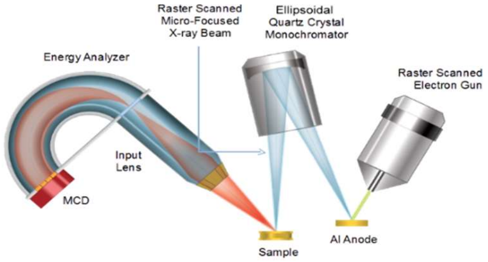

Figure 9. Schematic representation of X-ray Photoelectron Spectroscopy (XPS)

The instrument consist of an X-ray source, electron energy analyser, an ultra-high vacuum stainless steel chamber, magnetic field shielding and sample holder. PHI 5000 VersaProbe III XPS analyser is used in the present study for the identification of silver loading in zinc oxide.

2.6 Gas sensing application

2.6.1 Substrate cleaning

The substrate act as a basement for sensing material as well as it provides mechanical stability and rigidity to the sensing film. Generally, the substrates used for film coating include glass, alumina, silicon and metals, aluminium nitride and beryllium oxide based ceramic. Among them, glass is widely accepted one for film coating because it will not alter the electrical and optical properties of the sensing material. Hence, we have used ordinary borosil glass plates with 1×1 cm dimension as the substrate material.

Prior to film deposition, it is very important that the substrates should be thoroughly cleaned. The impurities present on the surface of the substrate will definitely interfere with the measurements. The common contaminants present on the substrate include dust, fingerprints, oil, and lint particles. The cleaning technique usually rest on on the nature of the substrate and nature of the contaminants. The following steps were adopted for cleaning the glass substrate:

1. Firstly, the glass substrate (1×1 cm) were washed in soap solution and then with deionized water to remove any traces of soap.
2. It is then subjected to acetone washing by ultrasonication and rinsed with deionized water.
3. Third step involves the chromic acid washing. Here a brown solution of saturated potassium dichromate in concentrated $H_2 SO_4$ is used for the cleaning purpose. Chromic acid is known to be efficient for removing contaminants from glass substrates. The substrates were soaked in chromic acid solution for about 1 hour at 90° C.

4. Finally, the glass slides were thoroughly washed with deionized water and dried in an oven at 100° C.

2.6.2 Sensor fabrication and gas response measurements

Appropriate amount of zinc oxide powder was ground together with a few drops of ethanol in an agate mortar. The slurry obtained was coated on a previously cleaned borosil glass plate with a dimension 1×1cm. The prepared ZnO films were calcined at 400ºC for 2 hours. The thickness of the films were measured to be 1.2 µm.

Prior to the gas sensing experiment, the sensor materials were heated and cooled repeatedly in order to avoid the effect of moisture and other impurities. All the gas sensing measurements were carried out at atmospheric pressure, and the temperature was adjusted by means of a temperature controller. The sensor set up consists of a stainless steel test chamber with an effective volume of 280 mL. Two copper wires connected to the sensing material by silver paste worked as electrical contact for the sensor.

A heater consist of nichrome wire aids to reach preferred temperature for the sensor material. Once the desired temperature is attained, a calculated volume of the analyte gas was injected to the chamber from the calibrated cylinder. The optimum operating temperature is identified by conducting experiments at different temperature conditions. The percentage response (S) of the material was calculated by the following equation:

%Response, $S= [(R_g-R_a)/R_a]\times100$ (for oxidizing gases)

$S= [(R_g-R_a)/R_a]\times100$ (for reducing gases)

Where R_g is the sensor resistance in the presence of analyte gas atmosphere and R_a is the resistance of the material in air. The response and recovery time of gas sensors are defined as the time taken by the sensor to reach 90% of the response value in the gas atmosphere and 10% of the base value in air.

2.7 Photocatalytic activity measurement

2.7.1 Photocatalytic reduction of hexavalent chromium

30ppm Cr(VI) solution was prepared by dissolving potassium dichromate in deionized water. The pH of the solution was adjusted by adding adequate amount of 0.1N HCl or NaOH. A catalyst dosage of 1 g/L was used throughout the reactions. Prior to UV light exposure, the mixture was stirred in dark for 30 minutes to reach adsorption desorption equilibrium. The photocatalytic experiments were carried out in a Luzchem LSZ4X model photoreactor under continuous stirring at room temperature. Samples of liquids were extracted at regular intervals of time. Centrifuged to separate suspended particles and analyzed by standard diphenyl cardazide (DPC) assay using a UV-visible spectrophotometer at λ_{max}= 540nm. The influence of hole scavengers was studied by adding 10μL of ethanol or phenol to the reaction mixture.

2.7.2 Photocatalytic degradation of Rhodamine B

The photocatalytic activity of the catalyst systems was evaluated by monitoring the photo decomposition of aqueous Rhodamine B solution under UV irradiation. The reactions were carried out at room temperature. 50 mg of the catalyst was added to 50mL of 10mg/L Rhodamine B aqueous solution. The pH of the dye solution was adjusted to 11. The mixture was stirred for 20 minutes in dark to reach the adsorption desorption equilibrium and then exposed to UV light (λ= 380nm) in a Luzchem LZC 4X model photoreactor with continuous stirring to maintain uniform distribution of suspension throughout the reaction. It was then allowed to react, and aliquots of 4 mL were withdrawn after regular time intervals (10 minutes). The solution was centrifuged and the absorption spectrum of supernatant liquid was recorded by UV/visible spectrophotometer. The characteristic absorption peak of Rhodamine B at λ=554nm was chosen to monitor the concentration by quantitative analysis method. The catalytic efficiency was expressed in terms of percentage photodegradation of Rhodamine B, which has been calculated using the formula:

$$\%\ \text{Degradation} = \frac{Co - Ct}{Co} \times 100$$

Where C_o is the initial concentration of dye solution and C_t is the concentration after a time‘t’.

2.7.3 Chemical oxygen demand (COD)

Chemical oxygen demand (COD) measurement was carried out by using the following method; the organic contaminants present in the samples were oxidized by potassium dichromate in H_2SO_4 in the presence of $HgSO_4$ and Ag_2SO_4 in the medium. The blank as well as the dye sample were refluxed in H_2SO_4 in the presence of $HgSO_4$ and Ag_2SO_4, and then refluxed with known volume of standard $K_2Cr_2O_7$ solution. The amount of potassium dichromate is estimated by titrated against with standard ferrous ammonium sulfate (FAS) using ferroin as indicator. A blank experiment was also conducted with dye solution without photodegradation. The samples are dye solutions after photocatalytic treatment. COD was calculated by the following formula:

$$COD = \frac{(Blank\ titre\ value - Sample\ titre\ value) \times Normality\ of\ FAS \times 8 \times 1000}{Volume\ of\ the\ sample}$$

References

1. C.P. Poole Jr., F.J. Owens, Introduction to Nanotechnology, A John Wiley 81 Sons, Inc., Publication, Hoboken, New Jersey, 2003.
2. S.K. Kulkarni, Nanotechnology: Principles and Practices (Third edition), Springer International Publishing, Cham, Switzerland, 2015.
3. S.G. Podorov, N.N. Faleev, K.M. Pavlov, D.M. Paganin, S.A. Stepanov, and E. Forster, A new approach to wide-angle dynamical X-ray diffraction by deformed crystals" J. Appl. Crystallogr., v.39, 2006.
4. D. McMullan, "Scanning electron microscopy 1928–1965". Scanning, 2006, 17 (3): 175–185.
5. Z. L. Wang, Reflected Electron Microscopy and Spectroscopy for Surface Analysis, Cambridge University Press, Cambridge, New York, 1996, ISBN: 0-521-48266-6456.
6. D.B. Williams, C.B. Carter, Transmission Electron Microscopy: A Textbook for Materials Science. New York, USA: Springer, 2009, p. 35, ISBN 978-0-387-76500-6.
7. P. Griffiths, J.A. de Hasseth, Fourier Transform Infrared Spectrometry (2nd ed.). Wiley-Blackwell., 2007, ISBN 0-471-19404-2.
8. J. F. Moulder, W. F. Stickle, P. E. Sobol and K. Bomben, Handbook of X-ray Photoelectron Spectroscopy, Perkin-Elmer Corporation.
9. S. J. Gregg, K. S. W. Sing, Adsorption, Surface Area and Porosity, Academic Press, London etc., 1982.
10. I. Langmuir, J. Am. Chem. Soc. 1918, 40, 1361.
11. S. Brunauer, P.H. Emmett, E. Teller, J. Am. Chem. Soc. , 1938, 60, 309.
12. G. Horvath, K. Kawazoe, J. Chem. Eng. Jpn., 1983, 16, 470.

Chapter 3

Characterization of Zinc Oxide Architectures

ZnO structures prepared through different routes have been characterized using various analytical tools. The results in this regard are discussed in this section.

3.1 X-Ray diffraction analysis

The powder X-Ray diffraction analysis clearly indicates the phase purity and crystalline nature of the prepared samples. Figure 1 shows the XRD pattern of the prepared zinc oxide systems. 2θ values and the corresponding crystal planes are: 31.7° (100), 34.3° (002), 36.2 (101), 47.4 (102), 56.5 (110), 62.8 (103) and 67.8 (112) (JCPDS No. 36-1451), which in turn confirms the hexagonal wurtzite structure of zinc oxide. The crystallite size of the samples were calculated using Debye Scherrer equation:

$$D = 0.9\lambda/\beta\cos\theta \qquad (1)$$

Where D is the average crystallite size (Å), λ is the wavelength of the X-ray radiation (Cu Kα = 1.54178 Å), β is the full width at half maximum intensity of the peak corresponding to the plane (101), and θ is the diffraction angle (36.2). From the above equation the average crystallite sizes were found to be 29.24 nm, 28.28 nm and 31.68 nm for flower like zinc oxide architectures zinc oxide nanosheet assembled flower (ZSF), rod assembled flower (ZRF) and particle assembled flower (ZPF) respectively. The same for individual nano units were 22.91 nm, 21.65 nm and 21.62 nm respectively assigned to zinc oxide nanosheets (ZS), nanorods (ZR) and nanoparticles (ZP) systems.

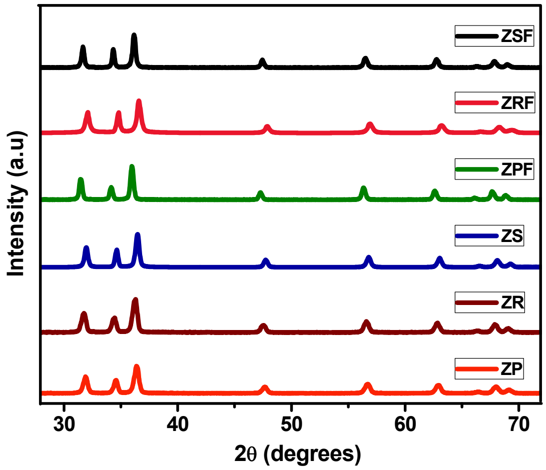

Figure 1. XRD pattern of ZnO systems

3.2 Electron microscopy analysis

Morphology of the catalyst systems are apparent from the electron microscopic images (Figure 2 and 3). Flower like structures composed of self-assembled nanosheets as petals were obtained through CTAB assisted hydrothermal route (Figure 2a). The average particle size observed is approximately 2-3 µm. The interleaving nanosheets have the uniform thickness of about 30 nm. These nanosheets were arranged in such a fashion that they lead to a unique flower like morphology. Zinc oxide nanorods assembled flowers (ZRF) and nanoparticle assembled flowers (ZPF) were synthesized in the absence of CTAB. The formation of nanoparticles assembled flowers were achieved within a reaction period of 3 hours and increasing the hydrothermal treatment time to 15 hours resulted in the formation of nanorod assembled flower like architectures. The average particle size, revealed from Figure 2b and 2c, was found to be 3-4 µm and 1-2 µm for ZRF and ZPF systems respectively.

By reducing the hydrothermal treatment time of nanosheets assembled flower like system (ZSF) to 3 hours, sheet like structures with an average thickness of ~30 nm were formed (Figure 2d). Keeping the hydrothermal treatment time of ZSF system to 15 hours and replacing the surfactant CTAB with PVP and HMTA, resulted in the formation of nanoparticles (ZP) and nanorods (ZR) respectively. The Nanoparticles having size less than 100 nm and naorods having diameter 500-600 nm is also evident from the scanning electron microscopic images (Figure 2e and 2f) of ZP and ZR systems respectively.

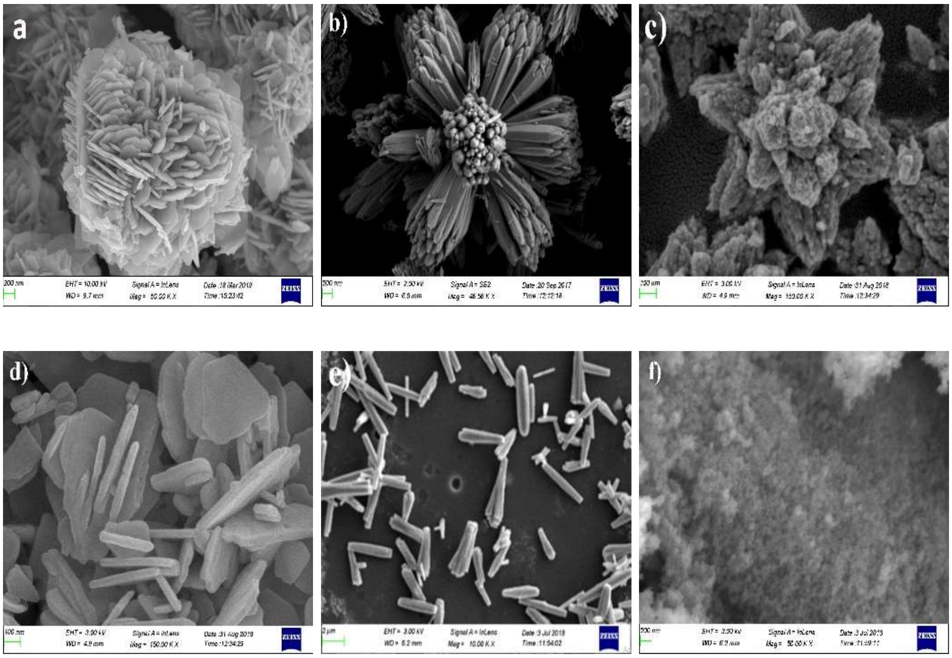

Figure 2. FESEM images of Zinc oxide systems ZSF (a); ZRF (b); ZPF(c); ZS(d); ZR (e) and ZP (f)

Further confirmation of crystal structure and morphology was obtained by means of high resolution transmission electron microscopic (HRTEM) analysis. The TEM images were in agreement with the scanning electron microscopic images. The flower like architectures composed of self-assembled nanosheets, nanorods and nanoparticles can be clearly seen from Figure 3a - 3c respectively, assigned to ZSF, ZRF & ZPF systems. The nanobuliding units such as nanosheets, nanorods and nanoparticles are displayed in Figure 3d - 3f respectively signifying ZS, ZR & ZP systems. The sheet like structures have some porous nature which can be identified from the TEM images.

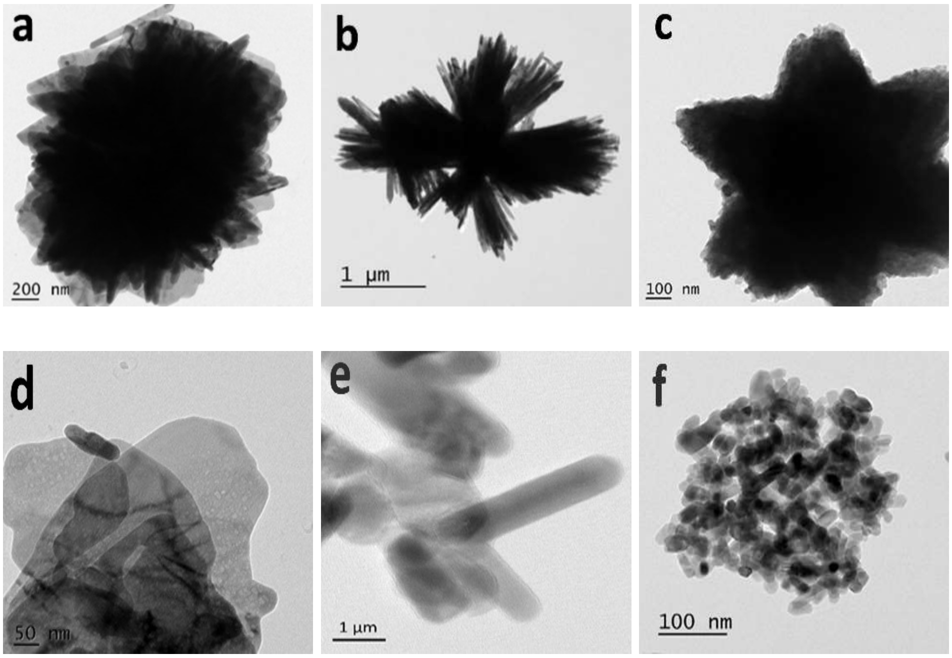

Figure 3. TEM images of zinc oxide systems

The HRTEM images of nanosheets and nanoparticles are displayed in Figure 4. Lattice fringes corresponding to interplanar spacing 0.28 nm indicates exposed (0001) planes in nanosheets (Figure 4b). Nanoparticles having size less than 100 nm is observed in Figure 4c. The inter planar spacing in nanoparticles is 0.26 nm (Figure 4d), which signifies the exposed non-polar$(10\bar{1}0)$facets.

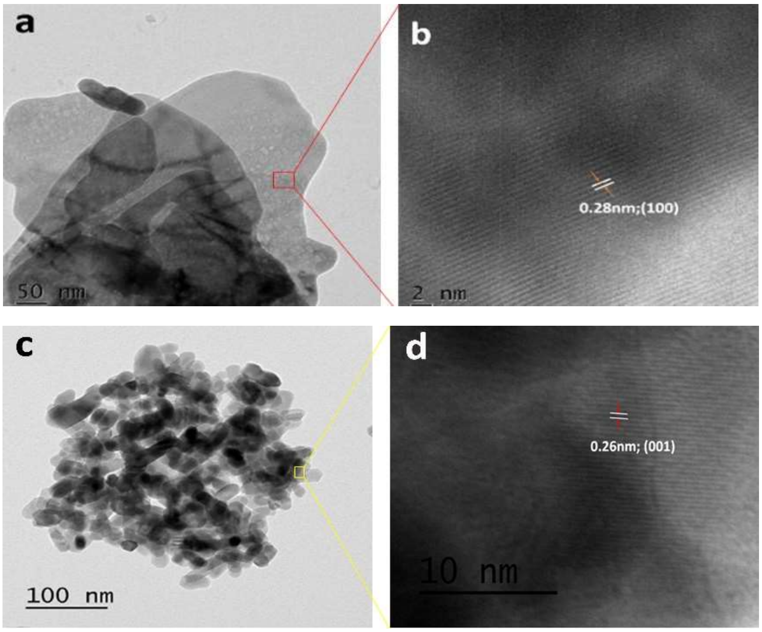

Figure 4. HRTEM images of ZS (a&b) and ZP (c&d) systems

3.3 Growth mechanism

Zinc oxide crystallizes in hexagonal wurtzite structure in which each Zn^{2+} ion is tetrahedrally coordinated to four surrounding O^{2-} ions and vice versa which constitute both polar and non-polar crystal facets. The polar surfaces in zinc oxide include the oxygen polar $(000\bar{1})$ and zinc polar (0001) planes. The oxygen polar planes are negatively charged while zinc polar planes are positively charged. This oppositely charged basal planes results in a normal dipole moment along the c-axis. Normally, the polar surfaces undergo large surface reconstruction in order to get stabilized. But the zinc oxide structures have exceptionally stable polar surfaces. The most common non-polar facets in zinc oxide having low surface energy are $\{2\bar{1}\bar{1}0\}$ and $\{01\bar{1}0\}$. The typical hexagonal wurtzite structure of zinc oxide is depicted in Figure 5. The intrinsic anisotropy in zinc oxide results in its crystal growth along c-axis to form one dimensional nanostructures. Therefore, in the absence of any of the surface directing agents, zinc oxide structures will grow along c-axis and the resultant morphology will be nanorods having prominent non-polar surfaces due to their lower energies.

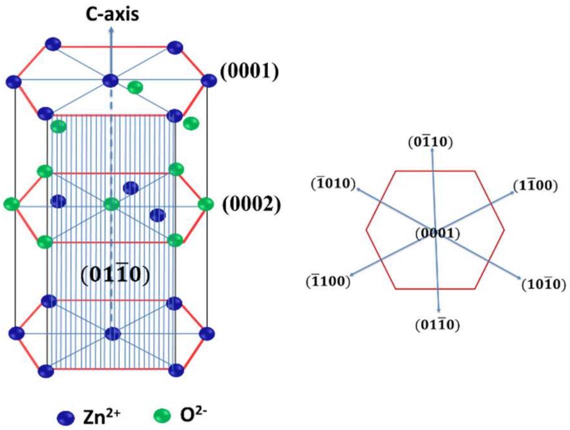

Figure 5. Crystal planes in hexagonal wurtzite structure of zinc oxide

We can tune the growth rates of zinc oxide crystals along different direction by controlling the hydrothermal reaction parameters such as precursor concentration, temperature, reaction time, use of surfactants etc. The use of proper surfactant for moulding the morphology of zinc oxide architectures have long been studied. We have adopted three surfactant molecules for the effective tuning of morphology. The surfactants used were cetyl trimethyl ammonium bromide (CTAB), polyvinyl pyrrolidine (PVP) and hexamethylene tertamine (HMTA). The presence of surfactant in the solution decreases its surface tension thereby enabling the formation of a new phase.

3.3.1 Zinc oxide nanosheets and nanosheets assembled flower like architectures

Zinc nitrate in aqueous medium dissociates in the presence of a strong base like NaOH to form zinc hydroxide. The excess OH^- present in the reaction medium further reacts with zinc hydroxide and results in the formation of a tetrahedral anionic species $Zn(OH)_4^{2-}$, which is the growth unit of zinc oxide. The cationic surfactant CTAB forms CTA^+ ions in the solution with a long hydrophobic tail and a tetrahedral head. The matching symmetry and the electrostatic interaction between the positively charged surfactant and the negatively charged zinc oxide growth unit leads to the formation of a complex $[CTA^+\text{-}[Zn(OH)_4]^{2-}]$. Thus CTAB in the medium can act as an ionic carrier as well as it facilitate the oriented growth of zinc oxide crystal.

$$Zn(NO_3)_2 + 2NaOH \leftrightarrow Zn(OH)_2 + 2NaNO_3 \qquad (1)$$

$$Zn(OH)_2 + 2OH^- \leftrightarrow [Zn(OH)_4]^{2-} \qquad (2)$$

$$CTAB \leftrightarrow CTA^+ + Br^- \qquad (3)$$

$$[Zn(OH)_4]^{2-} + CTA^+ \leftrightarrow \{CTA^+\text{-}[Zn(OH)_4]^{2-}\} \qquad (4)$$

$$\{CTA^+\text{-}[Zn(OH)_4]^{2-}\} \leftrightarrow ZnO + H_2O + CTA^+ \qquad (5)$$

The polar surfaces in zinc oxide are stabilized by the combined effect of CTA^+ and OH^- ions. This inhibits the growth of zinc oxide along c-axis. Consequently, the elongation of zinc oxide along the nonpolar crystal facets takes place. Nanosheets having polar exposed surfaces will be the outcome of this synthetic route. Subsequently, with increasing hydrothermal treatment time, Ostwald ripening takes place and the nanosheet building units get self-assembled to assume spherical shapes in order to lower surface energy. More and more nanosheets become interlaced and overlapped with each other to form a multilayer network structure, and thereby forming the flower like ZnO micro structures. Zhao et al also have obtained a flower like morphology when the reaction was allowed to proceed up to the same reaction time (~15 hrs) in presence of citric acid [1]. They suggested an initial nanosheet formation of ZnO, which aggregates to nanospheres within an hour of the reaction. Sun et al. have suggested a change in behaviour of

CTAB in the presence of excess NaOH, which can affect the growth process [2]. As suggested by Xu et al. the formation of zinc oxide nanosheets through CTAB assisted route adopts a growth orientation along nonpolar planes [3].

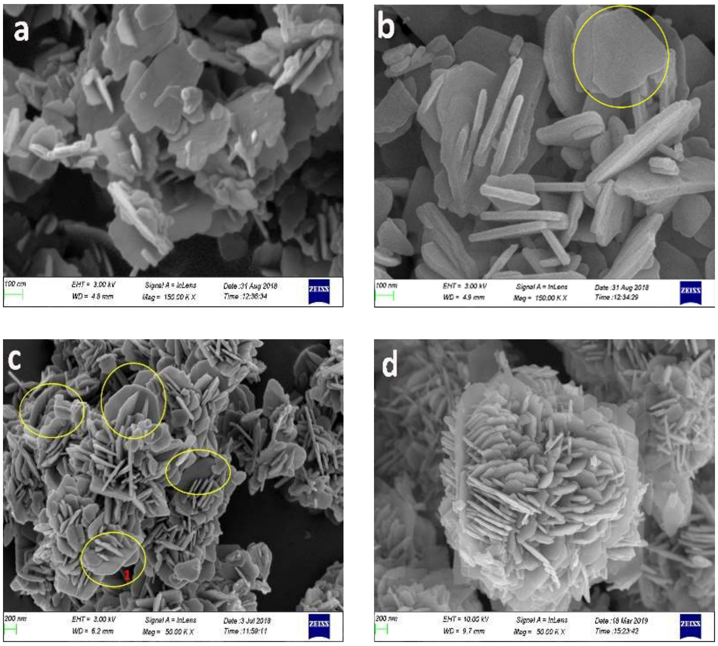

Figure 6. CTAB assisted hydrothermal synthesis of zinc oxide at different time intervals: stirring only (a); hydrothermal thermal treatment time 3 hrs (b), 9 hrs (c) and 15 hrs (d)

The SEM images of zinc oxide architectures prepared through CTAB assisted hydrothermal route at different time interval is portrayed in Figure 6. The detailed information of morphology and growth evolution of zinc oxide flowers can be derived from these images. The initial formation of nanosheets having no definite crystal edges formed after the vigorous stirring of zinc nitrate with NaOH and CTAB is shown in Figure 6a. As the reaction proceeds, the edges of nanosheets become sharp and some distorted hexagonal shapes were seen. Figure 6b is the SEM image of zinc oxide nanosheets achieved within a time interval of 3 hours. After 9 hours of hydrothermal treatment, oriented attachment of more and more nanosheets were observed. This leads to the secondary growth of nanosheets on primary hexagonal sheets (Figure 6c). Distorted hexagonal structures with exposed polar planes can be clearly seen in Figure 6b and 6c.

The encircled portion in Figure 6c labeled as 1 is zoomed in Figure 7a. The primary growth of hexagonal shaped zinc oxide nanosheets and the secondary formation of nanosheets on the hexagonal structure is obvious from the Figure. The enlarged view of the petals of zinc oxide flower like structures composed of nanosheets as the building units is shown in Figure 7b. The edges of distorted hexagonal nanosheets are highlighted with yellow lines. It can be also figured out from this image that the nanosheets are actually distorted hexagonal shapes with exposed polar surfaces.

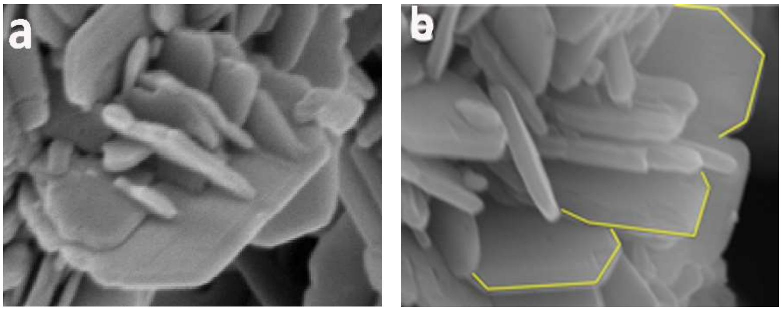

Figure 7. Magnified view of distorted hexagonal shaped nanosheets

3.3.2 Nanoparticle and nanorod assembled flower like architectures (ZPF and ZRF)

The role of CTAB in the formation of zinc oxide nanosheets is again confirmed from the preparation of zinc oxide nanorods assembled flowers (ZRF) as well as nanoparticle assembled flower like (ZPF) structures. These two structures i.e., ZRF and ZPF are prepared through the same procedure as that of ZSF and ZS systems respectively except that the surfactant CTAB is not used in these case. Hydrothermal treatment time of 3 hours results in the formation of nanoparticles assembled flower like architectures. Further increase in the reaction time to 15 hours yields nanorods assembled flowers. The increase in hydrothermal reaction time enabled oriented attachment of nanoparticles in flower like structures to form nanorods. In the absence of CTAB, the anisotropic growth along c-axis will takes place and the final structure will be nanorods with exposed nonpolar facets.

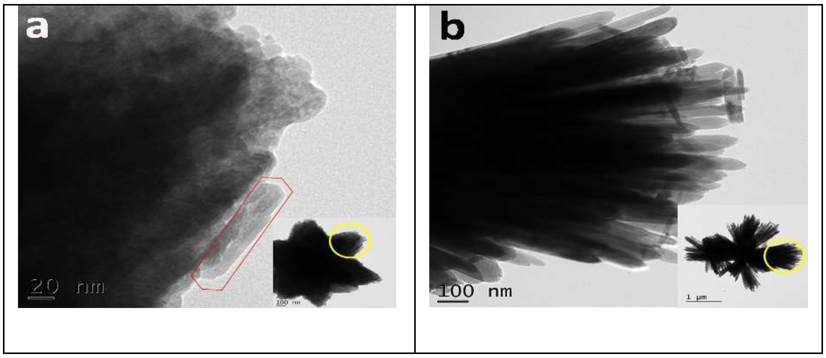

Figure 8. Petals of nanoparticle assembled flowers (a) and nanorods assembled flowers (b)

The petals of ZPF and ZRF are displayed in Figure 8. From this we can understand that the flowers are formed by the self-assembly of nanoparticles and nanorods respectively for ZPF and ZRF systems. The commencement of nanorod formation can be clearly figured out from the region marked red in Figure 8 a. It is noted that nanorod assembled flowers are obtained through prolonging the reaction time for ZP. Hence, it is indicated that rod structure is generated by the aligned nano particles.

3.3.3 Nanoparticles and Nanorods (ZP and ZR)

For the synthesis of nanoparticles and nanorods, we have used two different surfactant molecules viz, polyvinyl pyrrolidone (PVP) and hexamthylene tetramine (HMTA). Being nonpolar surfactants, PVP and HMTA can easily get attached to the non-polar surfaces of zinc oxide. This will result in the evolution of zinc oxide along c-axis to form nanorods. The nanoparticles are actually short nanorods with an average diameter 20 nm and length 50 nm. This provides a clear image of the possible attachment of surfactants on the non polar surfaces and inhibiting the growth along that direction. Eventually the growth direction of zinc oxide will be in the c-axis and subsequent predominance of non-polar crystal facets in nanoparticles and nanorods. Nanoparticles, due to their size in the nano regime (under 100 nm), provide a possibility for highly exposed surfaces than nanorods with large size. A schematic representation of growth of zinc oxide in the presence of HMTA is shown in Figure 9.

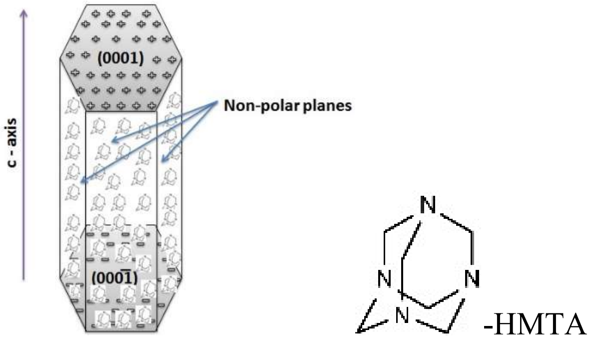

Figure 9. Oriented growth of zinc oxide nanorods in the presence of HMTA

3.4 Surface area analysis

The BET surface area values obtained by nitrogen adsorption studies are presented in Table no. 1. Considerable difference in surface area values was noted in systems, achieved via hydrothermal synthetic route. Zinc oxide nanoparticles possessed highest surface area, 40.349 m^2/g. The value is almost three fold higher when compared to the nanosheets, vis., 13.747 m^2/g. Surface area of zinc oxide nanorods (ZR) were found to be 12.815 m^2/g. Flower like structures, owing to their large size, have lower surface area as expected. Zinc oxide nanoparticle assembled flowers have the largest surface area among the flower like structures. A value of 20.327 m^2/g is ascribed to ZPF system. ZRF system with rod like morphology possessed a surface area value of 10.324 m^2/g. The least surface area among the six morphologically different structures is observed for zinc oxide nanosheet assembled flower like architecture (ZSF), 8.092 m^2/g. The surface area values are summarized in Table 1.

Table 1. Surface area values of ZnO systems

System	**Surface Area (m^2/g)**
ZP	40.349
ZPF	20.327
ZS	13.747
ZR	12.815
ZRF	10.324
ZSF	8.092

3.5 Fourier Transform Infra-Red Spectroscopy

The FTIR spectra of all the calcined zinc oxide samples are displayed in Figure 10. The IR band between 520 and 450 cm^{-1} observed in all samples corresponds to the stretching frequency of Zn–O vibrations. The intense band at 3435 cm^{-1} indicates the stretching vibration of –O–H mode of hydroxyl group in the catalyst. The weak absorption band at 2345 cm^{-1} is due to the adsorbed CO_2 molecules in the prepared systems. The peak around 1640 cm^{-1} signifies the stretching mode of physisorbed water molecules in the oxide samples.

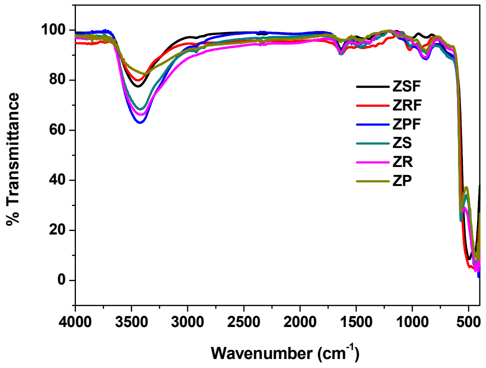

Figure 10. FTIR spectra of zinc oxide systems

3.6 UV-Vis Diffuse Reflectance Spectroscopy

UV- Visible diffuse reflectance spectra (UV-DRS) were recorded in the wavelength range 250-700 nm. The absorption spectra and the corresponding Kubelka-Munk plots of all the systems are shown in Figure 11a and 11b respectively. The catalyst systems exhibit broad absorption spectra in the UV region. It is clear that the materials absorb in the entire UV region. The absorption edge lies around 380-400 nm. The band gap values calculated for flower like systems were 3.18, 3.19 and 3.17 eV respectively, for ZSF, ZRF and ZPF systems. The band gap values were 3.21 eV, 3.17 eV and 3.22 eV respectively for nanosheets, nanorods and nanoparticles.

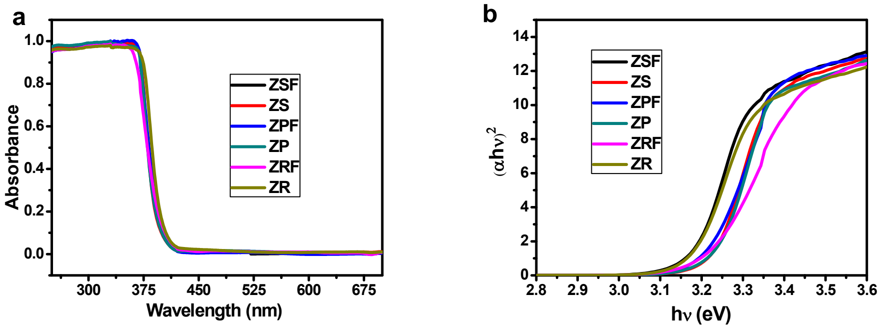

Figure 11. UV-Visible absorption spectra (a) and corresponding Kubelka-Munk plots (b) of the catalyst systems.

3.7 Photoluminescence study

Photoluminescence (PL) spectroscopy is an ideal characterization technique for the determination of defects in ZnO. Figure 12 illustrates the photoluminescence spectra of the prepared systems. The room temperature photoluminescence spectra of all the systems were measured at an excitation wavelength of 325 nm. The near band edge (NBE) emission responsible for the recombination of free excitons lies around 380-400 nm for all the systems.

The defect states in the prepared systems were analyzed from the visible region of PL spectra. It is well established that the presence of defects will induce the defect energy levels in the band gaps of semiconductor materials. Various types of defects present in zinc oxide such as zinc vacancies, oxygen vacancies, interstitial zinc and interstitial oxygen contribute to different PL peaks in the visible region [4]. The emissions at ~485 nm and ~530 nm are due to the oxygen vacancy defects in the system [5]. The electron transfer between conduction band and singly ionized as well as doubly ionized oxygen vacancies (V_o^* and V_o^{**}) contributes to the green emission at 530 nm. The intensity of emission is determined by the density of the oxygen vacancies in the ZnO nanostructures [6].

ZSF system with nanosheets assembled flower like structure possesses the least intense photoluminescence spectrum, which indicates the lowest electron-hole recombination efficiency in the system. It was also noticed that the PL intensity at 530 nm is highest for ZnO nanosheets. This suggests that the system is rich in oxygen vacancy defects. The amount of oxygen vacancy defects in the systems as indicated by the PL spectra followed the order ZS>ZRF>ZPF>ZR>ZP>ZSF.

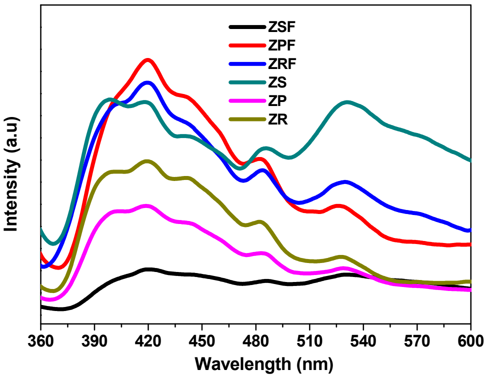

Figure 12. Photoluminescence spectra of Zinc oxide samples

3.8 Raman spectral analysis

To further support the observation derived from the PL analysis, the Raman spectra of the systems were obtained (Figure 13). Zinc oxide with wurtzite structure belongs to C_{6v}^4 ($P6_3mc$) space group. The optic mode in zinc oxide predicted by group theory is as follows:

$$\Gamma opt= A_1+ 2B_1+ E_1+ 2E_2 \qquad (2)$$

Where A_1 and E_1 modes (polar) are both IR and Raman active, whereas E_2 (non-polar) is only Raman active. The non-polar E_2 mode comprises of low and high frequency phonons (E_2 low and E_2 high), which are related to the vibration of the Zn sublattice and oxygen atoms, respectively. B_1 mode is both Raman and IR inactive. Raman spectra showing E_2 (high) mode is sketched in Figure 13, which is an indication of oxygen species in zinc oxide. A shift in the peak position of Raman spectra to lower frequency indicates an increase in oxygen vacancy [7-10]. The E_2 high mode for Zinc oxide nanosheet can be clearly seen at 435 cm^{-1}. A shift for this panel by 4 cm^{-1} is observed from ZP system which is located at 439 cm^{-1}. Hence it is confirmed that zinc oxide nanosheets are having more oxygen vacancy than the nanoparticles.

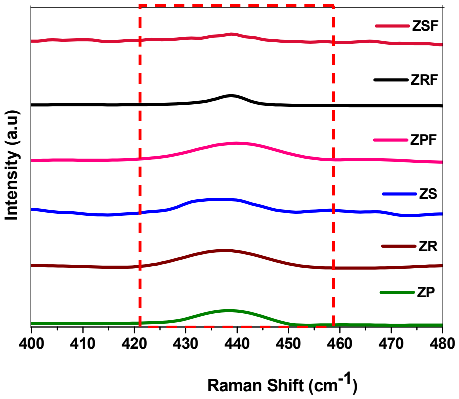

Figure 13. Raman spectra of zinc oxide systems at room temperature

References

1. X. Zhao, F. Lou, M. Li, X. Lou, Z. Li, J. Zhou, Sol_gel-based hydrothermal method for the synthesis of 3D flower-like ZnO microstructures composed of nanosheets for photocatalytic applications, Ceram. Int. 40 (2014) 5507
2. X.M. Sun, X. Chen, Z.X. Deng, Y.D. Li, A CTAB-assisted hydrothermal orientation growth of ZnO nanorods, Materials Chemistry and Physics 78 (2002) 99.
3. X.L. Xu, Y.Chen, S.Y.Ma, S.H.Yan, Y.Z.Ma, T.Wang, H.Q.Bian, CTAB-assisted synthesis of unique 3D ZnO and the acetone sensing performances, Materials Letters151 (2015) 5.
4. A. B. Djurisˇic´, Y. H. Leung, K. H. Tam, L. Ding, W. K. Ge, H. Y. Chen, S. Gwo, Green, yellow, and orange defect emission from ZnO nanostructures: Influence of excitation wavelength, Appl. Phys. Lett., 2006 , 88, 103107 (1-3).
5. D. Chen, Z. Wang, T. Ren, H. Ding, W. Yao, R. Zong, Y. Zhu, Influence of defects on the photocatalytic activity of ZnO, J. Phys. Chem. C. 118 (2014) 15300−15307.
6. T. A. T. Do,H. T.Giang, D. V.Huong, P. Q.Ngan,G. H. Thai, D. T. Thu, T. D. Lam, Correlation between photoluminescence spectra with gas sensing and photocatalytic activities in hierarchical ZnO nanostructures, RSC Adv. 7 (2017) 9826–9832.
7. R. Zhang, P. G. Yin, N. Wang, L.Guo, Photoluminescence and Raman scattering of ZnOnanorods, Solid State Sci. 11 (2009) 865–869.
8. H. Fukushima, T. Kozu, H. Shima, H. Funakubo, H. Uchida, T. Katoda, .K. Nishida, “Evaluation of Oxygen Vacancy in ZnO using Raman Spectroscopy”, In: Proceedings of the Joint IEEE

International Symposium on the Applications of Ferroelectric (ISAF 2015), International Symposium on Integrated Functionalities (ISIF 2015), and Piezoelectric Force Microscopy Workshop (PFM 2015): Singapore, May 24-27, 2015.

9. H. Fukushima, T. Kozu, H. Shima, H. Funakubo, H. Uchida, T. Katoda, K. Nishida, Evaluation of oxygen vacancies in ZnO single crystals and powders by micro-Raman spectroscopy, J. Ceram.Soc.Jpn. 125 (2017) 445-448.
10. J. Das, S.K. Pradhan, D.R. Sahu c , D.K. Mishra d , S.N. Sarangi e , B.B. Nayak d , S. Verma e , B.K. Roul, Micro-Raman and XPS studies of pure ZnO ceramics, Physica B 405 (2010) 2492–2497.

Chapter 4

Gas Sensor Applications of Zinc Oxide Architectures

4.1 Introduction

The quest of human beings to imitate Mother Nature has led to numerous wonderful inventions. The artificial emulation of olfaction is one among them, which is thought to be very difficult for decades. Olfaction is the capability of our nose to selectively recognize different odorant in the air. The odorants are actually chemicals which can be detected by the sensory cells in the nose. The olfactory receptors present in our nose are specific protein molecules that can bind chemicals selectively and the signals are transmitted to brain. This gives us the sense of smell. Fabrication of devices which are capable of imitating our nose was a grave issue before the scientific world. Researchers paid much of their time for the fabrication of devices that can sense chemicals artificially. A potential technological invention which can be called as electronic nose is termed as Gas sensors.

In the beginning of 20th century, people used caged canary, a songful bird, for the detection of poisonous gas in mines. This was the first model of gas sensors used by human beings. In 1938, Wagner et al. observed a significant change in electrical properties of semiconductor material on exposure to reducing or oxidizing gas at high temperatures [1]. Motivated from wagner's observation, Seyama et al., in 1962, used zinc oxide thin film for the detection of gaseous components [2]. They observed a change in electrical conductivity of the film on adsorption and desorption of gases at high operating temperatures above 400° C. Reducing gases like ethanol, carbon dioxide etc. increase the conductivity of the film and oxidizing gases like O_2 decrease the same. Their results were promising when compared to the conventional thermal conductivity detectors. Seyama's pivotal work became the stepping stone in the development of semiconductor gas sensors.

After that in the early 1970s, Taguchi patented a gas sensor device using tin oxide as the sensing material for the detection of explosive gases [3].

Although the first gas sensor device by Seyama operated above 400° C, the Taguchi's sensor operates preferably in the temperature range around 200° C. A momentous expansion in the field of semiconductor gas sensors were endured in the late 1980s. A great deal of efforts have been taken by many researchers since then for the development of a gas sensor with high sensitivity, selectivity, fast response-recovery characteristics, wide range of detection and low detection limit, with low power consumption.

Gas sensors find much applications in various day to day technologies. Many industries, domestic as well as automobile technologies, relay on gas sensors. They have found application in environmental monitoring, emission and quality control, medical diagnostics and safety purposes. The current scenario of environmental pollution and rapid change in climate demands the early detection of toxic gases. Different types of gas sensors have been used for decades, such as catalytic, semiconductor, electrochemical, optical and surface acoustic wave gas sensors [4]. Among the various types, semiconductor metal oxide gas sensors play a key role in the detection of various pollutants in both water and air. Semiconductor metal oxides such as SnO_2, ZnO, WO_3, In_2O_3, Cr_2O_3, Co_3O_4, CuO, TiO_2, Fe_2O_3, CeO_2, NiO, TeO_2, and MoO_3 have been used as gas sensors by researchers.

4.2 Gas sensing mechanism in Metal Oxide

Gas sensing is a surface phenomenon in which the gas-solid interaction takes place on the surface of the sensing material. There are two basic functions involved in gas sensors. They are receptor functions and tranducer functions. The ability of the sensor to interact with the chemical species is governed by the receptor function. Transducer function converts the signal produced by chemical interaction with the metal oxide surface into measurable electrical signals. Receptor and transducer functions of a semiconducting metal oxide depends on its morphology, surface area, exposed crystal planes, structural defects, impurities, etc.

The actual mechanism involved in semiconductor metal oxide gas sensing is still under controversy and not fully understood. However, some well accepted models for gas sensing is put forwarded by the researchers all over the world. Chemiresistive sensing mechanism is followed in most of the metal oxide gas sensors. On exposure to air, metal oxides ionosorb oxygen as O_2^-, O^- and O^{2-} depending upon the temperature at which ionosorption takes place. At room temperature, O_2^- is adsorbed on the surface of metal oxide thereby capturing electrons from the material. Consequently the resistance of n-type semiconductor increases and p-type semiconductor decreases at room temperature. On exposure to reducing gases like NH_3, ethanol, CO_2 etc., the gas molecules get oxidized by the surface adsorbed anionic oxygen species and release electrons back to the metal oxide lattice. As a result, exposure to reducing gases, decrease in the resistance of n-type metal oxides.

Chemiresistive gas sensing mechanism can also be exemplified using oxygen vacancy model. The change in the oxygen stoichiometry of the sensing material due to the reactions between oxygen vacancies and gas molecules is the key focus of this model. Oxidizing gases like NO_2 directly react with metal oxide surfaces and affect its charge carrier density. The oxygen vacancy in metal oxide surface can act as active sites for oxidizing gases to get adsorbed. The oxygen molecules of NO_2 are adsorbed by oxygen vacancy defects on the surface of the sensing material and then capture free electrons during this reaction. The subsequent capturing of electrons from the surface of metal oxides by oxidizing gases results in an increased resistance of the material. Therefore, these vacancy defects function as acceptors that reduce the free electron concentration and form electron depletion region at the surface.

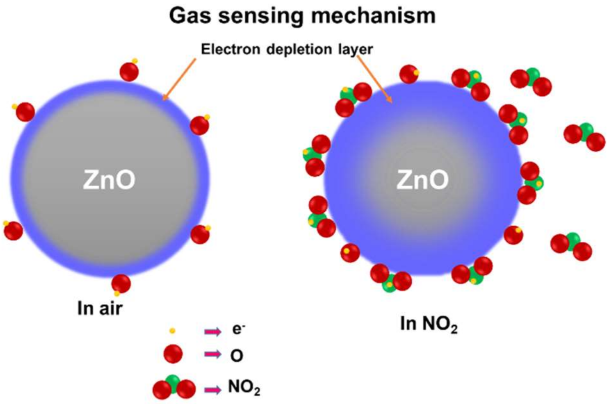

Figure 1. Gas sensing mechanism for oxidising gases

4.3 ZnO based sensors

Zinc oxide, a well-known semiconductor metal oxide, with n-type conductivity is widely used as a gas sensing platform due to its interesting physical, chemical, thermal and electrical properties. It has been widely used for the fabrication of gas sensors which can detect a wide range of gaseous pollutants. Zinc oxide nanostructures have played various roles in optical, electrochemical and chemoresistive sensors. It has been employed for the detection of various pollutants and non-polluting materials including toxic and non-toxic organic compounds, heavy metals, cations and anions, reducing and oxidizing gases (both toxic and non-toxic) etc. Simultaneous detection of phenol and o-cresol was achieved by zinc oxide nanosheets [5]. Hu et al. developed an electrochemical sensor using zinc oxide branched hierarchical nanorods for the detection of a carcinogenic compound hydrazine [6]. The system has shown a highest sensitivity of 5.35 $\mu A \mu M^{-1} cm^{-2}$ with a short response time of 3s. Their results confirmed the specific surface area dependent performance of zinc oxide nanostructures.

An electrode composed of ZnO-Cu nanocomposite was used for the immobilisation of glucose oxidase, thereby constructing a glucose biosensor [7]. (3-aminopropyl) triethoxysilane (APTES) capped zinc oxide quantum dots were employed as fluorescent probe for the detection of picric acid in water [8].

Chey et al. fabricated a glucose biosensor based on zinc oxide nanorods for indirect detection of mercury ions [9]. β-cyclodextrin-capped ZnO quantum dots were used as a fluorescent probe for the micromolar detection of Co(II) ions [10]. A chemosensor based on zinc oxide imine linked biocompatible system was utilized for the nanomolar detection of Co(II) ions [11]. Recently, a fluorescent paper sensor based on zinc oxide nanoparticles was put forward for copper ions by Liu et al [12]. The sensor can detect micromolar levels of copper ions without the aid of a photoluminescence spectrometer. Kaur et al. reported a selective Hg (II) sensor made up of zinc oxide nanoparticles decorated with organic receptors [13]. The sensor has shown more than 90% accuracy for nanomolar detection of mercury ions with a detection limit of 0.19 nM. Salen decorated zinc oxide structures were reported by various researchers for the recognition studies of Hg (II) and Mg (II) ions [14]. Sharma and his team developed a highly selective Al(III) and Zn(II) ions based on surface modified zinc oxide nanoparticles [15]. Moussawi et al. made an effort to synthesize curcumin modified zinc oxide for the detection and removal of arsenic [16].

Zinc oxide quantum dots were synthesised via a simple method by Singh et al [17]. The highly luminescent quantum dots modified with APTES were employed for sensing free chlorine in water. Urea coupled zinc oxide sensors were utilized for an effective differential anion sensor [18]. Fluoride ion binding leads to a red shift in the uv-visible absorption spectrum of receptor while sulphate ions produced a blue shift. Selective detection of sulphate ions achieved via decoration of zinc oxide surface with an anion receptor based on monopodal thiourea [19].

Prodigious efforts were taken by the researchers to exploit the gas sensing behaviour of zinc oxide towards various gaseous pollutants and other important gases. Hierarchically porous ZnO nanosheets were used for CO detection at an operating temperature of 300° C [20]. ppb level detection of volatile organic compounds (VOCs) such as acetone and benzene were carried out using hollow zinc oxide nanocages [21]. The architecture dependent gas sensing performance for VOCs is obvious from the report. Hydrogen, the future energy source, sensing was done with zinc oxide nanofibers with an exceptional sensitivity and selectivity [22]. Diao et al. investigated the influence of morphology on H_2S sensing properties of zinc oxide microstructures [23]. ZnO nanosheets self-assembled flower like ZnO architectures showed a maximum response to ethanol gas at an operating temperature 370° C [24]. A cross-linked ZnO nanorods (NRs)-based ammonia gas sensor operating at 300° C was fabricated using this fine semiconductor metal oxide [25].

In this section, the sensing ability of ZnO systems towards an oxidizing gas NO_2 and a reducing gas NH_3 was explained. ZnO with different morphologies are analysed for their ability to detect the presence of these gases, which is monitored by the change resistance of the material.

4.4 Why we need NO_2 sensors….?

Nitrogen dioxide, a strong oxidizing gas, is one among the most hazardous gaseous pollutants produced by both natural and anthropogenic activities. A reasonably high concentration of this brownish red gas enters to the atmosphere through human activities. It is a major component in automotive emission, and is also released from industrial sources. It is a secondary pollutant produced from the primary source NO during automobile exhaust emission, which contributes the major portion. NO_2 is used as an intermediate for the production of HNO_3 which is employed for the production of fertilizers. Electric power plant boilers are also a major source of NO_2. The high temperature heating processes involved in industrial boilers, petroleum refineries, incinerators, gas turbines, iron and steel mills, cement manufacture and glass manufacture accompanied with the production of nitrogen oxides. Natural sources of nitrogen oxides comprise lightning and forest fires.

On reaction with UV light, NO_2 undergo photodecomposition and results in the production of organic as well as inorganic nitrates. Production of HNO_3 by the absorption of moisture in the atmosphere causes acid rain. The reactive species produced during the photodissciation of NO_2 leads to the formation of peroxyacetyl nitrate in the atmosphere.

The detrimental effects of NO_2 include damage to respiratory tracks, cardiovascular diseases, skin or eye burn etc. It also degrades the dyes and pigments in the textile industry. Environmental imbalance is also noted, as it produces ground level ozone which causes photochemical smog. Ozone in the stratosphere protect us from the UV radiation, whereas its presence in troposphere is very dangerous. Apart from this, acid rain caused by NO_2 is responsible for the corrosion of metals and substantial damage to trees and crops which will adversely affect our economy. NO_2 exposure to plants seriously affect the formation of chlorophyll and thereby reducing the rate of photosynthesis.

According to the American Conference of Government Industrial Hygienists, the threshold value of NO_2 gas in air is 3 ppm. Environmental protection agency (EPA) suggests a still lower concentration, 0.053 ppm. Considering the aforementioned toxic effects, there is an urge to fabricate efficient NO_2 sensors that can monitor the concentration in the ppm level. Considerable effort has been undertaken by the researchers in this direction. A summary on the gas sensing properties of unloaded/loaded metal oxide semiconductors for NO_2 gas sensing is listed in Table 1.

Table 1: Summary of NO_2 sensors

Ref. No	**Sensing material**	**Detection range**	**Operating temperature**	**Response Time (t_{resp})**	**Recovery Time (t_{rec})**	**Sensitivity (S)**
26	ZnO	100 ppb – 1 ppm	25-200° C	20 s (200° C, 1 ppm)	-	0.3 (200°C, 100ppb) $\Delta R/R_o$
27.	Poly(3-hexylthiophene)/ZnO Hybrid (p-type)	1-100 ppm	25° C	15 min	45min	59% (4ppm) (Ra−Rg)/ Ra × 100 (%)
28.	ZnO	100 ppb-1ppm in dry air	200° C Dark (D) and Light (L) conditions	2 min 45 s 3.2 min 1.3 min	10 min 8 min 22 min 12 min	0.213, 0.195 (100ppb, D, L) 1.308, 1.316 (1ppm, D, L)
29.	WO_3 films	10 ppm	Room Temperature (RT)	20 min	40 min	1.8 (RNO2/ Rair)
30.	WO_3 films	0.16 ppm	RT	20 min	42.5 min	4.0
31.	WO_3@GO	15 ppm	RT	4 min	5 min	1.2
32.	WO_3@GO	0.9 ppm	RT	18.6 min	23.3 min	63.73
33.	WO_3@NWCNTs@rGO nanohybrids	10 ppm	RT	7 min	15 min	1.2
34.	Zinc oxide	1 ppm in air	350°C	~3–6 min	>5 min	~+80%
35.	Reduced graphene oxide	5 ppm in dry N2	RT	>10 min	10 min	~-30%
36.	graphene–	1-20 ppm	RT-300°C	25–200 s	25–200 s	140

	WO_3	in humid air				(R_{NO2}/R_{AIR}) (250°, 5 ppm, 0.5wt%)
37.	rGO-ZnO	1-25 ppm in humid air	RT-	165 s	499 s	25.6% (5 ppm) (Ra −Rg)/Ra ×100%,
38.	SnO_2 nanoparticles-rGO	5 ppm	50	135 s	200 s	3.31 (rGO wt% 26.5) Rg/Ra
39.	Cu_2O nanowires-rGO	2 ppm	RT	~500s	>500s	67.8% ([(Igas − Io)/Io] × 100%) LOD= 64ppb
40.	Discoid SnO_2/ rGO	0-2 ppm	75° C	11 min	6 min	696 (1ppm) (R=Rg/Ra) (1.4wt% rGO) LOD= 50ppb
41.	In_2O_3–rGO	5 to 100 ppm	RT	4 min	24 min	8.25 (30ppm) Rg/Ra
42.	3D graphene aerogel–ZnO	10-200 ppm	RT	132 s	164 s	8% (50 ppm) ((Rg−Ra)/Ra× 100%)
43.	ZnO	0.058-23 ppm	190° C	15s (T) 21s (F)	36s(T) 29s(F)	275 (T) 60(F) (5ppm) Rg/Ra
44.	ZnO	5 ppm in N_2	250° C	~4 min	~25 min	199 (R -

						Ro)/Ro
45.	WO_3	1-100 ppm	75-250° C	>100s	>800 s	10 (5 ppm, 100° C) Rg/Ra
46.	ZnO	10-100 ppm	100-250° C	~20 s	>200 s	3100% (100ppm, 175° C) (Rg − Ra/Ra) × 100
47.	ZnO	20 ppb-1 ppm	150 ° C	-	-	4.5 (1ppm, long nanorods) Rg/Ra
48.	ZnO	20 ppm	RT	1.42 min	1.71 min	~119 Rg/Ra
49.	Graphene/ WO_3	100 ppm	100° C (2.45V)	-	-	~1.29 (2 wt%) Rg/Ra
50.	ZnO	5-20 ppm in N_2 and air	RT	72 s in N_2 20 min in air	69 s 15 min	32 (N_2) 2.5(air) (20ppm) Rg/Ra

4.5 ZnO as NO_2 sensor

Zinc oxide was chosen as the first semiconductor metal oxide gas sensing material. It is an n-type semiconductor with a wide band gap value 3.37 eV. The material is rich in oxygen vacancy defects, which makes it pertinent for gas sensor applications. Zinc oxide based sensors possess various advantages over conventional sensors. The high mechanical, thermal and chemical stability, good electrical and chemical properties, low cost and non-toxic nature made it more attractive for gas sensing application. Easy fabrication methods of the sensor material with high performance make zinc oxide more prominent in the gas sensing field. It satisfies the “4S” requirements for gas sensors i.e. sensitivity, stability, speed and selectivity.

Different factors have been influencing the gas sensing properties of zinc oxide. The morphology and size, surface area, crystal defects, exposed surface planes, operating temperature, nature of analyte gas etc. have role in deciding the performance of zinc oxide gas sensors. Zinc oxide hollow spheres were synthesised by a carbon microsphere template method. The system is selective for the detection of NO_2 at 240° C [51]. A theoretical approach on the adsorption of NO_2 on oxygen deficient surface of zinc oxide has been reported by Breedon et al [52]. A cacti like structure and nanoneedles of zinc oxide were prepared by a low temperature method and is employed for NO_2 sensing applications [53]. The gas sensing studies were conducted for a range of temperatures 150-250. The results revealed that the change in morphology has significantly change the gas sensing behaviour. A higher response is shown by Cacti like structure than nanoneedles towards NO_2 sensing. Morphology dependent gas sensing properties of zinc oxide for NO_2 sensing were discussed by Rai et al [54]. A maximum response of 44.2 for 50 ppm NO_2 gas was achieved at 300° C.

Wang et al. adopted a mechanoelectrospinning assisted selective growth method for the construction of a patterned zinc oxide nanorods array gas sensor [55]. The sensor presented excellent ohmic behaviour and high response to oxidizing gas NO_2 at 225° C. Their findings shed light on the fabrication of patterned nanostructured materials efficient for gas sensing. Zeolite modified zinc oxide nanostructures were used for NO_2 sensing applications [56]. A highly sensitive room temperature sensor based on zinc oxide nanopetals was reported by Sonker and his team [57].

Crystal plane dependent NO_2 sensing properties of zinc oxide have been explored by many researchers [58]. Studies revealed that zinc oxide with higher rate of oxygen vacancies are found to be highly sensitive for gas sensing. From the literature survey we came to the conclusion that most of the NO_2 sensors operate at temperatures greater than 200^o C. Even though a number of reports on room temperature NO_2 sensors are available, the long response and recovery time seem to be a drawback for such systems. Thrust is always focused on NO_2 gas sensors operating at low temperature, with high response time and low response and recovery time.

4.6 Need of ammonia sensors

Ammonia is a colourless, reducing gas with a pungent odour. It is alkaline in nature, highly corrosive and dissolves in water to form ammonium hydroxide. Ammonia is a widely used industrial gas for the production of fertilizers, pesticides, explosives, manufacture of plastics, textiles, dyes and other chemicals. It is a precursor for amino acids and nucleotides and is essential for many of the biological processes. It is a major constituent in many of the household cleaning lotions. Naturally ammonia is formed by the decay of organic matter which includes plants, animals and animal wastes.

Ammonia in its anhydrous form is lighter than air and will easily escape upwards. However, ammonia on reaction with moisture results in the formation of ammonium hydroxide which causes various health problems. The necrosis of tissues caused by ammonium hydroxide results in cellular destruction. The extraction of water by the breakdown of cellular proteins causes inflammatory effects. This irritating and corrosive gas causes serious respiratory track disorders, skin burns, permanent eye damage or blindness.

According to U.S Occupational Safety and Health Administration (OSHA), the maximum limit of ammonia exposure in air for 8 hours is 25 ppm.

Herein we make an attempt to fabricate six morphologically different zinc oxide nano/micro structures with specific crystal plane orientations. Out of the three morphological variations three are flower like architectures and remaining are the nano-building units of corresponding flower like structures. Six morphologically different zinc oxide nanostructures namely, nanosheets assembled flowers, nanosheets, nanoparticle assembled flowers, nanoparticles, nanorod assembled flowers and nanorods are achieved via a facile low temperature synthetic routes by changing the surfactant molecule. The gas sensing efficiency of the well characterized systems are investigated. Oxidizing gas NO_2 and reducing gas NH_3 are used as the analyte gases. The factors influencing gas sensing, such as crystal plane effect, oxygen vacancy defects, operating temperatures, gas concentration etc. are systematically analysed. Stability of the system is monitored by conducting the experiments over five cycles. Selectivity of the prepared systems towards NO_2 (oxidizing gas) over NH_3 (reducing gas) is also examined in this study.

4.7 Results and Discussion: NO_2 sensing

4.7.1 Morphology dependent NO_2 sensing properties of Zinc oxide

The three flower like structures viz., nanosheet assembled flowers (ZSF), nanorod assembled flowers (ZNF) and nanaoparticle assembled flowers (ZPF) as well as their nano-building units, nanosheets (ZS), nanorods (ZN) and nanoparticles (ZPF) are the systems under investigation. From the literature survey, it is found that the zinc oxide nanostructures are efficient at an operating temperature 200° C. Thus the morphological dependence on NO_2 sensing was carried out at this temperature with a gas concentration of 100 ppm. The resistance vs time plots of six morphologically different structures are portrayed in Figure 2. It can be seen from Figure 2 that the resistance of all the zinc oxide systems increases on exposure to NO_2 gas. The maximum change in resistance was shown by zinc oxide system with sheet like morphology. The temperature dependence of resistance for all the systems are given in the inset of Figure 2.

The % response of six morphologically different zinc oxide architectures were plotted in Figure 3. It is obvious from the Figure 3 that ZS system with sheet like morphology stands superior in sensing NO_2 at 200^o C than the other five morphological variations. The % responses calculated are 898, 2124, 109, 246, 343 and 70 for ZSF, ZS, ZRF, ZR, ZPF and ZP respectively with dry air as the recovery gas. It is obvious from Figure 1 that the base line resistance of zinc oxide nanosheets was very low as compared to the other five zinc oxide structures. This clearly indicates the increased carrier density in zinc oxide nanosheets which increases its sensitivity.

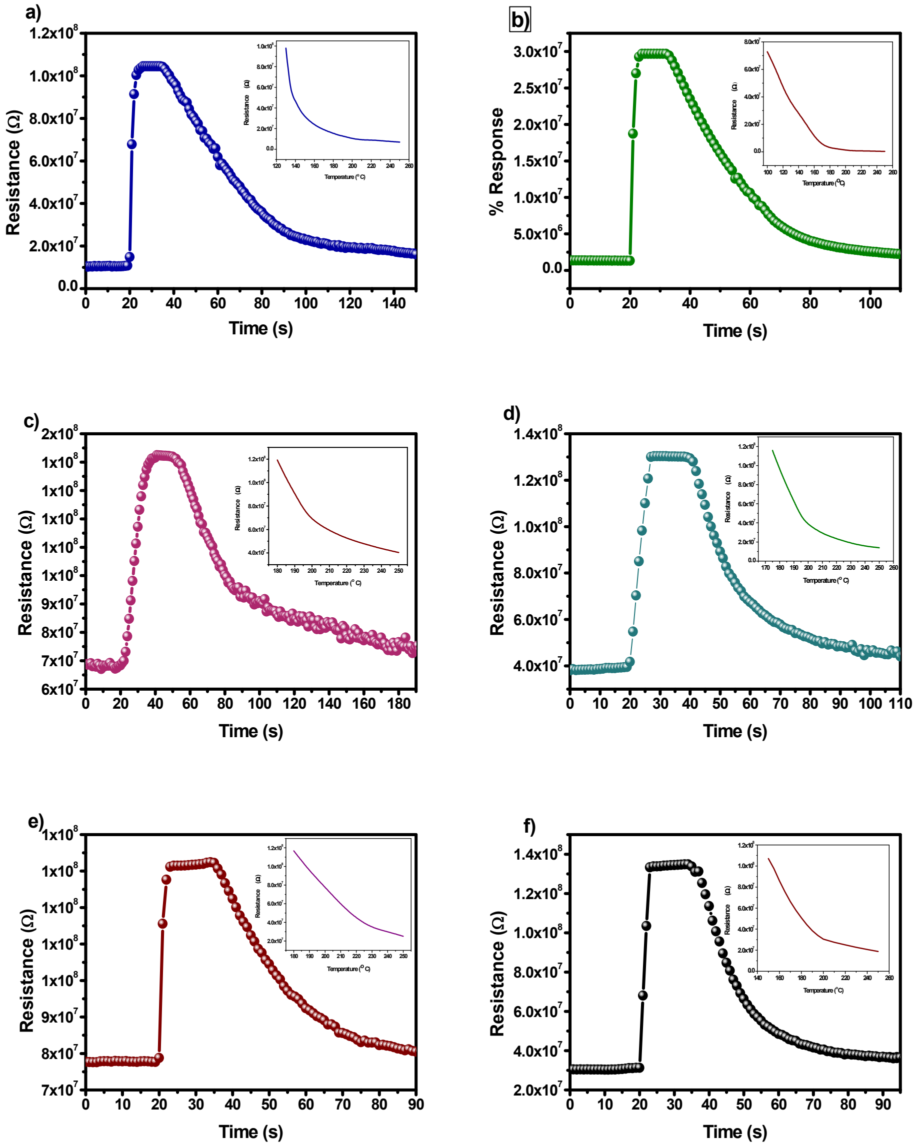

Figure 2. The morphology dependent NO_2 sensing properties of zinc oxide structures and their corresponding resistance vs temperature characteristics (inset): ZSF (a); ZS (b); ZNF (c); ZN (d); ZPF (e); ZP(f) (Gas concentration:100 ppm and temperature:200° C)

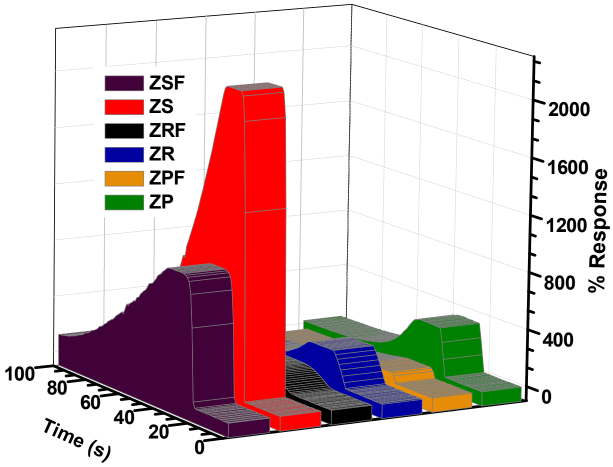

Figure 3. % Response curve for prepared zinc oxide systems

4.7.2 Temperature dependent gas sensing properties of zinc oxide systems

To optimize the operating temperature, the sensing studies were carried out at different temperatures using zinc oxide systems. The temperature ranges from 100-250° C and the analyte concentration was kept at 5 ppm. Figure 4, which demonstrates the temperature dependent gas sensing property of the prepared ZnO systems. The outstanding NO_2 sensing property of sheet like zinc oxide structure is again confirmed from the figure. Low temperature gas sensing was observed only for Z5 ZSF system. Zinc oxide nanosheets start responding to NO_2 gas at 100° C. The sensor response reaches a maximum at 170° C. Thereafter a decrease in sensitivity was observed. ZSF with nanosheet assembled flower like structures come next to zinc oxide nanosheets in NO_2 sensing performance. The sensitivity to NO_2 starts at 150° C and increases with temperature and reaches a maximum at 200°C. The reduction in response of the systems at higher temperatures may be due to the higher rate of desorption of NO_2 from the surface at high temperatures. The gas sensitivity of zinc oxide nanoparticles (ZP) and nanorods (ZR) linearly increases with temperature and the sensitivity values are much lower than that of zinc oxide nanosheets. The zinc oxide systems with nanorod assembled flowers (ZRF) and nanoparticle assembled flowers (ZPF) respond to NO_2 only above 200° C. The least NO_2 sensing characteristics was shown by ZPF systems.

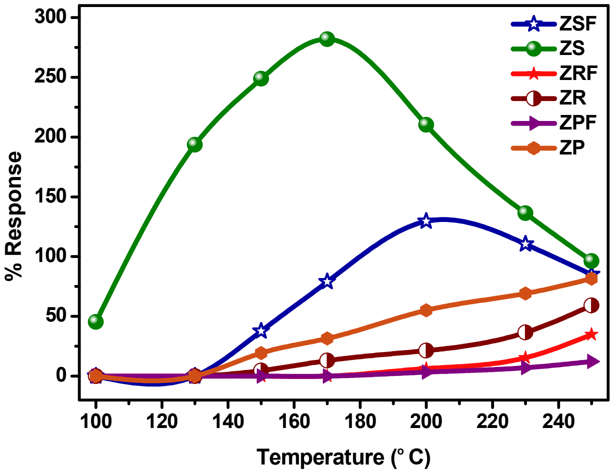

Figure 4. Temperature dependent NO_2 sensing properties of zinc oxide systems

4.7.3 Gas concentration dependent sensing

The morphological and temperature dependent studies revealed that zinc oxide system with sheet like structure is the best candidate for the detection of toxic gas NO_2. Thus further investigations were done with ZS system at an operating temperature of 170 ° C. A gas concentration of 1-100 ppm was analysed using zinc oxide nanosheets (Figure 5). The dynamic range of detection of the system is much superior to other previously reported works. A linear increase in sensor response was observed with increasing gas concentration, which in turn makes the system more reliable.

The highest response was achieved for 100 ppm NO_2 with a response value of 2279.64%. The lowest detection limit was found to be 1 ppm and the response value was 125.95% at 170° C. According to the American Conference of Government Industrial Hygienists, the threshold value of NO_2 gas in air is 3 ppm. Thus the system is established to be a successful NO_2 sensor.

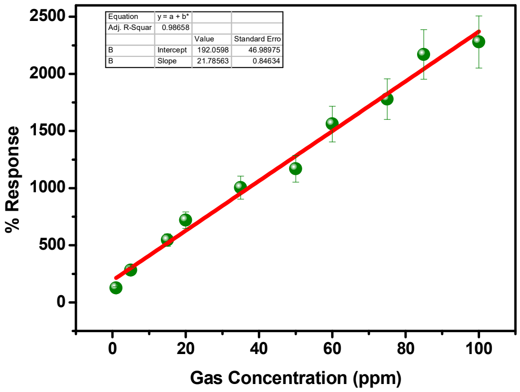

Equation	y = a + b*		
Adj. R-Squar	0.98658		
		Value	Standard Erro
B	Intercept	192.0598	46.98975
B	Slope	21.78563	0.84634

Figure 5. Response of ZS system to 1-100 ppm NO_2 concentrations

The dynamic response of ZS system to different gas concentrations (1-100 ppm) at 170° C is depicted in Figure 6. Here also it is seen that the response of the sensor increases with increase in gas concentration. The dynamic response curve indicates the reversibility of ZS system. Even after the continuous addition of higher gas concentrations, the sensor resistance recovers to its base line value in air, which is a good sensor characteristic, promising for practical application.

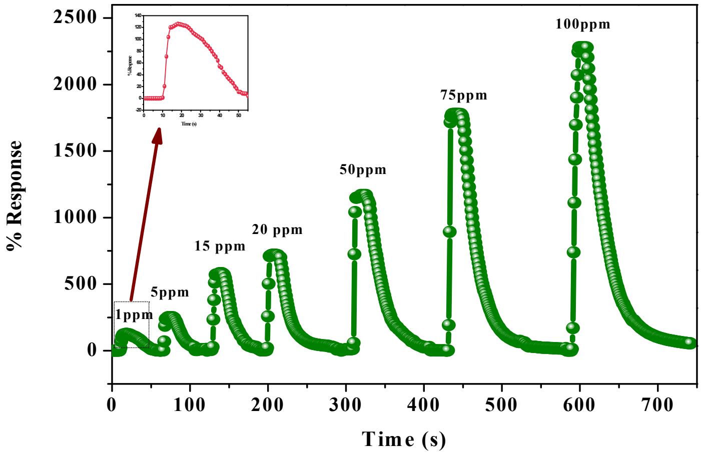

Figure 6. Dynamic response of ZS system to different concentrations of NO_2 at 170° C

The stability and reproducibility of the system was tested by exposing the metal oxide sensor to 20 ppm NO_2 for five cycles at 170° C. Figure 7 clearly indicates that even after the fifth cycle there is no potential reduction in sensor response. The results revealed that the sensor based on zinc oxide nanosheets has long term stability and reversibility.

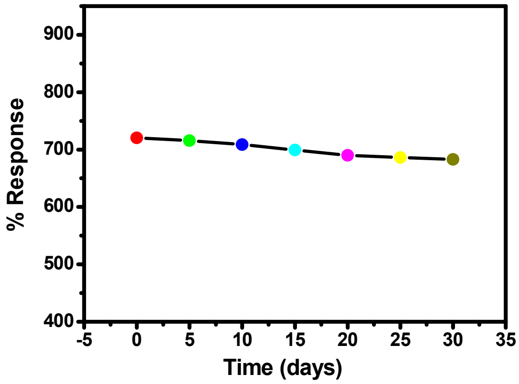

Figure 7. Stability of ZS system for five cycles

4.7.4 Gas sensing at lower working temperature – 100° C

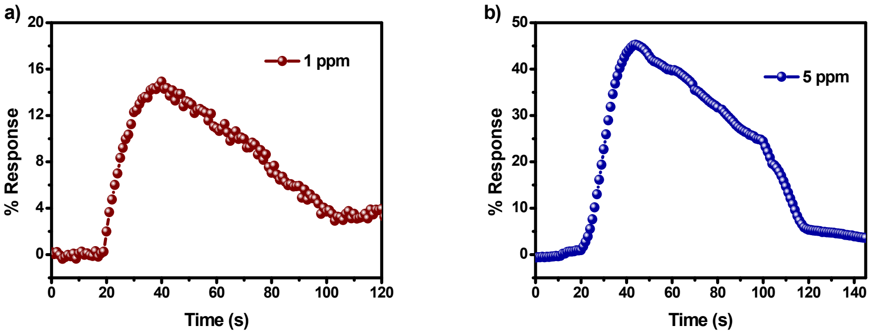

Figure 8. NO_2 sensing characteristics of zinc oxide nanosheets at 100° C

We further extended our experiments on the feasibility of zinc oxide nanosheets for NO_2 detection at lower working temperature, viz. 100° C. It is worthy to be noted that the ZS system is efficient at 100° C also. Figure 8 displays the response transient of zinc oxide nanosheets for 1 ppm and 5 ppm NO_2 at 100° C and percentage response of 14.91 and 45.3 respectively were achieved. From the literature survey, it is noted that the sensors operating at lower working temperatures usually show a long response and recovery time.The present system responds within 25 s on exposure to 5 ppm NO_2 even at 100° C and recovers to its original state within 90 s after the removal of gas from the chamber. This is understood to be a good quality for the sensor operating at low power consumption.

4.7.5 Response and recovery characteristics of zinc oxide nanosheets

All the prepared zinc oxide samples showed a fast response time and recovery time. Zinc oxide nanosheets possess a better response and recovery characteristics among the six morphological variations. Figure 9a shows the response transient to 35 ppm NO_2 at 170° C. It is observed that the ZS system has shown a fast response and recovery time of 3 s and 41 s respectively for

35 ppm NO_2. The response and recovery time vs temperature plot clearly indicates that the increase in temperature decreases response and recovery time.

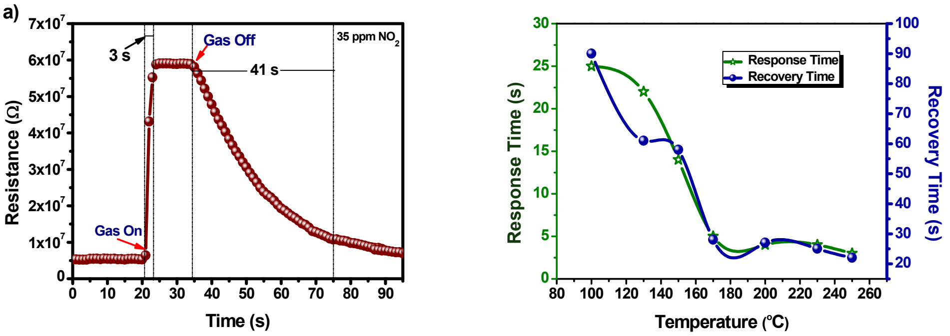

Figure 9. Response transient to 35 ppm NO_2 at 170° C (a); Temperature dependent response recovery characteristics (b)

It can be see that the zinc oxide nanosheets presented herein has noteworthy advantages over most of the reports system has substantial advantages over most of the reports presented in the Table 2.

Table 2. Literature review of NO_2 sensors operating at high operating temperature

Ref. No	**Sensing material**	**Detection range**	**Op. temp (°C)**	**t_{resp} (s)**	**t_{rec} (s)**	**S**	**Response equation**
59.	ZnO	0.2–5.0 ppm	250	-	-	199 (5ppm)	(R-Ro)/Ro
60.	ZnO	1 ppm	300	-	-	0.37	ΔR/Ro

61.	SnO_2	2 ppm 6 ppm 10 ppm	250	122 286 238	418 469 487	1.65 1.87 2.06	Rg/Ra
61.	SnO_2–ZnO (S.A>30 m^2/g)	2 ppm 6 ppm 10 ppm	“	142 376 317	400 407 343	2.06 2.90 4.26	Rg/Ra
61.	SnO_2–ZnO–Co	2 ppm 6 ppm 10 ppm	“	154 389 311	266 201 163	3.40 5.29 7.48	Rg/Ra
61.	SnO_2–ZnO	1 ppm	300	-	-	1.1	Rg/Ra
62.	ZnO	200	200	41	125s	64	100(Rg - Ra)/Ra
63.	ZnO	200	200	21	24	89	100(Rg - Ra)/Ra
64.	ZnO	10	350	120 (for 5 ppm)	150 (for 5 ppm)	1.81	Rg/Ra
65.	Au/ZnO	50	300			4.14	Rg/Ra
66.	ZnO	5 ppm	300	12	60	106	100(Rg - Ra)/Ra
66.	ZnO	5 ppm	300	40	100	43.43	100(Rg - Ra)/Ra
67.	ZnO	100	200	6.7	52.6	37.2	100(Rg - Ra)/Ra
68.	ZnO	100	200	6	17	36.3	100(Rg - Ra)/Ra
69.	ZnO	100	300	45	73	18	Rg/Ra

Our zinc oxide system with nanosheet like morphology has shown almost comparable sensitivity at 130° C with SnO_2-ZnO system reported by

Kim et al. at 250° C [61]. Moreover, our system possessed a very short response and recovery time in comparison with the aforementioned report. This projects the low temperature gas sensing efficiency of our system. Liangyuan et al. synthesized Nanocrystalline ZnO–SnO_2 composites (surface area= 64.1m^2 g^{-1}) by a reverse microemulsion method using cetyltrimethylammonium bromide (CTAB) as surfactant. The maximum response achieved by the sensing material, in the form of a pellet with a thickness of 2 mm, was 34.5 for 500 ppm NO_2 at an operating temperature of 250 ◦C [70]. For 200 ppm NO_2 the response was found to be 16 at 200 ° C.

4.7.7 NO_2 sensing mechanism

The general mechanism of gas sensing in metal oxide involves the change in electrical resistance of the material by the interaction between gas molecules and the surface of the material. The gas sensing mechanism of a metal oxide sensor is influenced by various factors such as the rate of adsorption and desorption, oxygen species, nature of the analyte gas, working temperature etc. When ZnO is exposed to air, oxygen molecules will get adsorbed on the sensor by extracting electrons from the surface, thereby increasing the resistance of the material. On exposure to oxidizing gas NO_2, the gas molecules get adsorbed on the surface, captures electrons from the conduction band, and also react with chemisorbed oxygen (Eqn (2) to (4). As suggested by Liu et al. the adsorption of NO_2 and oxygen molecules on the surface of sensor material compete each other. NO_2 is a strong electron acceptor than O_2 molecules and get physisorbed on the sensor surface by accepting electrons. This in turn creates a surface depletion region of electrons and consequently the resistance of the material further increases.

$$NO_2(g) \rightarrow NO_2(ads) \qquad (2)$$

$$NO_2(ads) + e^- \rightarrow NO_2^-(ads) \quad (3)$$

$$NO_2(ads) + O_2^-(ads) + 2e^- \rightarrow NO_2^-(ads) + 2O^-(ads) \quad (4)$$

Normally, the sensor response increases with increase in surface to volume ratio. The usual trend in sensitivity was not followed in the present study. This can be explained as follows. The intrinsic defects present in zinc oxide systems, especially the oxygen vacancy defects, facilitate the adsorption of oxidizing gases like NO_2 into the surface of ZnO materials. Higher the oxygen vacant sites, higher will be the sensitivity. As clear from photoluminescence and Raman spectral analysis, the prepared system with nanosheet like morphology having lower surface area are rich in oxygen vacant sites than nanoparticles. Hence, even though zinc oxide nanosheets possess lower surface area values, it has shown outstanding sensing performance due to its unique morphological features and oxygen vacancy defects.

A schematic representation of gas sensing mechanism and difference in adsorption of NO_2 on zinc oxide nanosheets (ZS) compared with nanoparticles (ZP) is illustrated in Scheme 1. Generally, it is considered that the system having high surface area is found to be more suitable for various application studies.

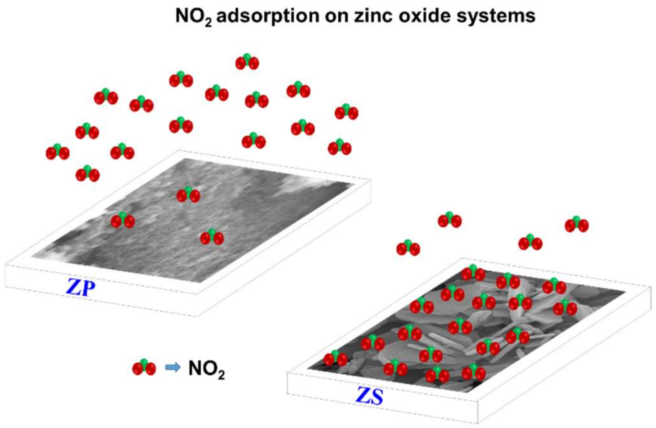

Scheme 1. NO_2 adsorption on ZS and ZP systems

It is also believed that the active planes in zinc oxide nanosheets are also capable for higher response values. ZS systems having exposed active (0001) planes are obvious from the electron microscopic analysis. This polar surfaces rich with oxygen vacant sites also act as active spots for the adsorption of gas molecules. Nanosheets assembled flower like zinc oxide structures come next in the activity order. This can be clearly illustrated with the presence of active planes in the architecture. However, the (0001) planes in ZSF are not as exposed as in nanosheets. Even though large surface area available in nanoparticles, the lack of active sites (both active planes and oxygen vacant sites) make it inferior in NO_2 sensing and keep it in the third position of activity. In the case of nanorods and nanorods assembled flowers, the surface exposed planes are non-polar hexagonal crystal planes leading to the lowering of adsorption of NO_2 on the surface. This results in lowering of their activity. The particle assembled flowers with no exposed specific crystal planes and lowest oxygen vacancy defect make it least responsive towards NO_2 gas.

A comparison of the present work with other reported works is summarized in Table 3 (gas concentration 100 ppm). When compared to similar works, the ZS system operates at lower temperature and has shown a fast response and recovery time, a wide detection range and a lower detection limit.

Table 3. Comparison of gas sensing performance of ZnO nanosheets towards 100 ppm NO_2 with literature reports

Sl. No	**System**	**Sensitivity %S**	**Operating Temperature**	**Response Time, t_{resp} (s)**	**Recovery Time, t_{rec} (s)**	**Ref**
1	ZnO nanorods	240	200	39	241	[71]
2	ZnO nanowires	68	200	20	162	[71]
3	TiO_2	~1500	400	-	-	[72]
4	ZnO thin film	37.2	200	6.7	52.6	[73]
5	Ni/ZnO	484	200	14	326	[74]
6	WO_3 thin film	31	200	13	251	[75]
7	ZnO Microflo	12.27	300	-	-	[76]

	wers	(Rg/Ra)				
8	ZnO Nanoparticles	36.3	200	6	17	[77]
9	ZnO Nanoparticles	18	300	45	73	[78]
10	ZnO nanosheet	2279	170	8	59	Present work

4.7.8 Ammonia sensing

This section deals with the sensing of a reducing gas, ammonia, which is also a toxic air pollutant. In the presence of a reducing gas like ammonia, a decrease in the resistance of zinc oxide material is observed. Zinc oxide on exposure to air, adsorb oxygen molecules from the atmosphere. The adsorbed oxygen molecules capture electrons from zinc oxide to form O_2^-, O^- and O^{2-}, depending upon the temperature at which the adsorption takes place. Reducing gas ammonia can react with this adsorbed oxygen species, which in turn release electrons back to the zinc oxide. Consequently, the resistance of the material decreases.

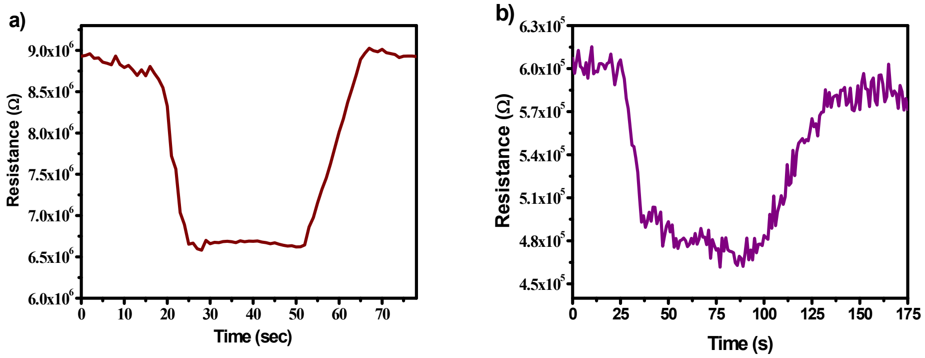

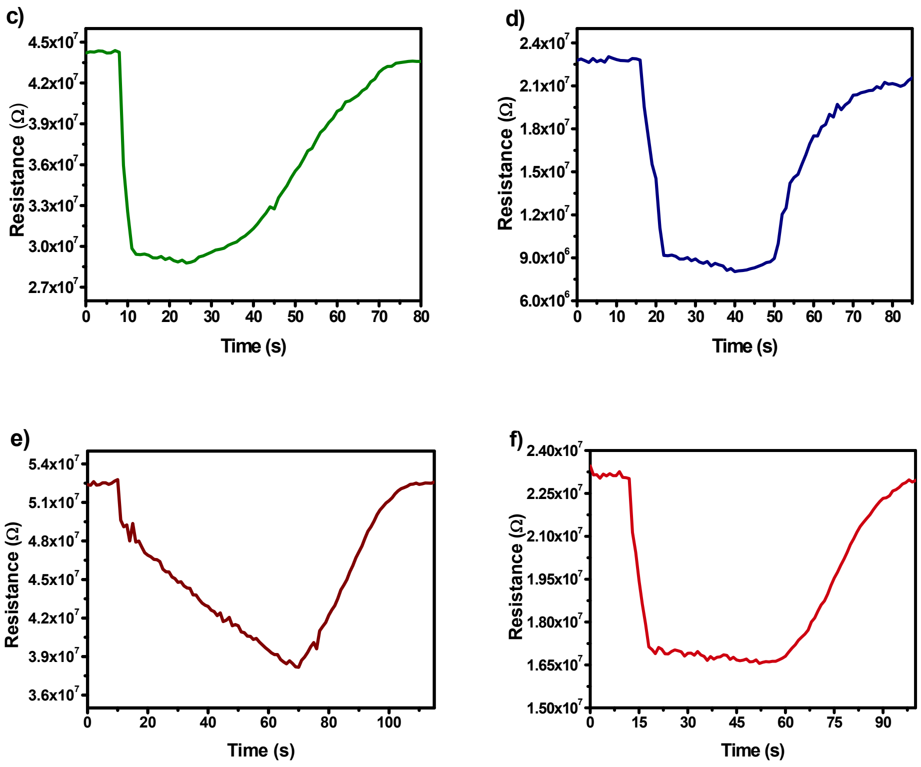

Figure 9. The morphology dependent NH_3 sensing properties of zinc oxide structures: ZSF (a); ZS (b); ZPF (c); ZP (d); ZRF (e); ZR (f)

Figure 9 shows the resistance vs time curve for ammonia sensing of the zinc oxide systems at 220° C and 100 ppm NH_3. The % response values of all the prepared systems are depicted in Figure.10. From the above mentioned plots, we can make out that zinc oxide nanoparticles (ZP system) is comparatively more efficient in sensing NH_3 than the other zinc oxide structures. The highest sensitivity towards 100 ppm NH_3 was observed at 220° C and the response value was found to be 64.4% for zinc oxide nanoparticles (ZP). It can be seen that except zinc oxide nanoparticle all the other systems show almost same response to NH_3.

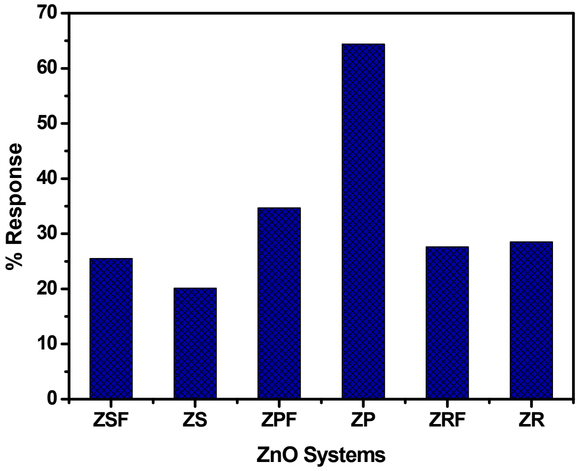

Figure10. % Response curve of prepared zinc oxide systems for NH_3 sensing

The trend in sensitivity of the materials towards ammonia can be explained based on the surface area of the samples. Higher the surface area of the system, higher will be the adsorption of oxygen molecules, leading to greater change in resistance. The nanoparticles possess the highest surface area (40.349 m^2/g) among the six morphologically different zinc oxide structures. The oxygen adsorption coverage will be more in zinc oxide nanoparticles. This enables the reaction of more number of ammonia molecules with ZP system. This is the reason why zinc oxide nanoparticles are more active in ammonia sensing.

The temperature dependent and gas concentration dependent ammonia sensing studies were conducted using zinc oxide nanoparticles (ZP). The usual trend in activity is observed here. Figure 11 illustrates the temperature dependentance. The sensitivity reached a maximum at 220^o C and this was taken as the operating temperature. Temperatures higher than the working temperature causes desorption of gas and the reduction in response. Variation of sensing ability with gas concentration is presented in Figure 11. The lack of availability of active surfaces causes a fall in response of NH_3 gas concentration higher than 100 ppm.

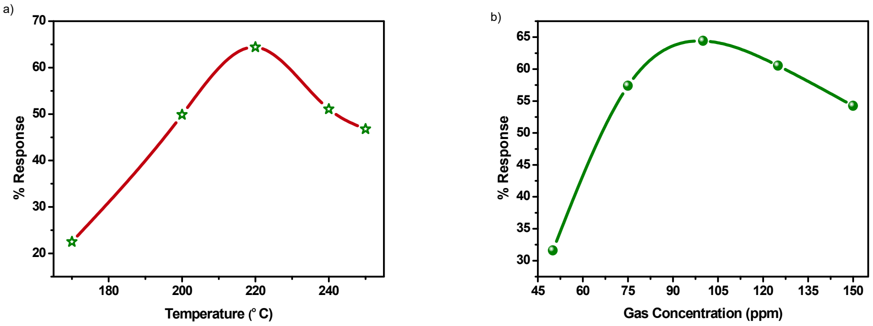

Figure 11. Temperature (a) and gas concentration (b) dependent NH_3 sensing by ZP system

4.7.9 Selective detection of NO_2 over NH_3

We also made an effort to analyze the difference in sensitivity of the prepared systems toward oxidizing as well as reducing gases. NO_2 (an oxidizing gas) and NH_3 (a reducing gas) were taken to this effect, which have different sensing mechanisms. Exposure to NO_2 increases the sensor resistance, while NH_3 decreases the same. The prepared zinc oxide nanosheets are highly selective for the detection of NO_2 over NH_3 gas. This can be attributed to the fact that the oxygen vacant sites available in zinc oxide nanosheets is responsible for the detection of NO_2. The oxygen molecules in NO_2 can easily get adsorbed on the active sites than NH_3 molecules. The selective detection of NO_2 over NH_3 over the metal oxide system is depicted in Figure 12.

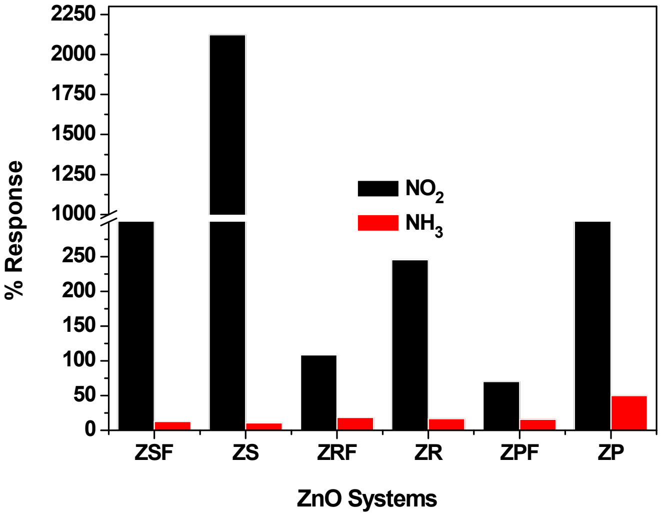

Figure12. Selectivity of prepared ZnO systems

4.8 Conclusions

In conclusion, zinc oxide with morphologically different structures were obtained by a facile low temperature hydrothermal method using different surfactant molecules, CTAB and PVP. The gas sensing properties of the well characterized zinc oxide structures were investigated. The sensor with sheet like morphology is highly sensitive for the detection of NO_2 gas. The predominance of (0001) planes in nanosheets was revealed from X-ray diffraction and electron microscopic analysis. Our investigation revealed that rather than surface area, the combined effect of surface active planes and oxygen deficient sites available in zinc oxide nanosheets is responsible for the detection of NO_2. Highly exposed surface active planes with plenty of oxygen vacant sites is suggested to be the reason sole reason for the higher efficiency of nanosheets, which possessed a low surface area. It was also noted that the sensor is selective for the detection of NO_2 than NH_3. Our studies shed light on the crystal plane dependent NO_2 sensing behaviour of zinc oxide. Rather than surface area the surface active planes and oxygen vacancy defects are the deciding factors for NO_2 detection. The nanoparticles having highest surface area have shown higher response towards NH_3. The high stability, sensitivity, short response and recovery time, large detection range and low detection limit makes the zinc oxide nanosheet sensor promising for practical applications.

References

1. C. Wagner, K. Hauffe, The stationary state of catalysts in homogeneous reactions. Ztschr. Elektrochem. 33 (1938)172.
2. T. Seiyama, A. Kato, K. Fujiishi, M. Nagatani, A new detector for gaseous components using semiconductive thin film. Anal. Chem. 34 (1962) 1502.
3. N. Taguchi, U.S. Patent 3,631,436 (1971).
4. Z. Yunusa, M. N. Hamidon, A. Kaiser, Z. Awang, Gas Sensors: A Review, Sensors & Transducers, 168 (2014) 61.
5. J. Liu, H. Huang, S. Zhong, X. She, D. Yin, Electrochemical Simultaneously Determination of Phenol and o-Cresol in Water Based on ZnO Nanosheets, Int. J. Electrochem. Sci., 11 (2016) 3921.
6. J. Hu, Z. Zhao, Y. Sun, Y. Wang, P. Li, W. Zhang, K. Lian, Controllable synthesis of branched hierarchical ZnO nanorod arrays for highly sensitive hydrazine detection, Applied Surface Science 364 (2016) 434.
7. C. Yang, C. Xu, X. Wang, ZnO/Cu Nanocomposite: A Platform for Direct Electrochemistry of Enzymes and Biosensing Applications Langmuir 28 (2012) 4580.
8. K. Singh, G.R. Chaudhary, S. Singh, S.K. Mehta, Synthesis of highly luminescent water stable ZnO quantum dots as photoluminescent sensor for picric acid, Journal of Luminescence154(2014)148.
9. C.O. Chey, Z.H. Ibupoto, K. Khun, O. Nur, M. Willander, Indirect Determination of Mercury Ion by Inhibition of a Glucose Biosensor Based on ZnO Nanorods, Sensors 12 (2012) 15063.
10. S. Geng, S.M. Lin, Y. Shi, N. B. Li, H.Q. Luo, Determination of cobalt(II) using β-cyclodextrin-capped ZnO quantum dots as a fluorescent probe, Microchim. Acta. 184 (2017) 2533.

11. H. Sharma, A. Singh, N. Kaur, N. Singh, ZnO-Based Imine-Linked Coupled Biocompatible Chemosensor for Nanomolar Detection of Co^{2+}, ACS Sustainable Chem. Eng. 1 (2013) 1600.
12. X. Liu, Y. Yang, X. Xing, Y. Wang, Grey level replaces fluorescent intensity: Fluorescent paper sensor based on ZnO nanoparticles for quantitative detection of Cu^{2+} without photoluminescence spectrometer, Sens. Actuators B: Chem. 255 (2017) 2356.
13. N. Kaur, J. Singh, P. Raj, N. Singh, H. Singh, S.K. Sharma, D.Y. Kim, N. Kaur ZnO decorated with organic nanoparticles based sensor for the ratiometric selective determination of mercury ions, New J. Chem., 40 (2016) 1529.
14. S.K. Sharma, N. Kaur, J. Singh, A. Singh, P. Raj, S. Sankara, D.Y. Kim, N. Singh, N. Kaur, Salen decorated nanostructured ZnO chemosensor for the detection of mercuric ions (Hg^{2+}), Sens. Actuators B: Chem. 232 (2016) 712.
15. H. Sharma, N. Singh, D.O. Jang, Imidazole and imine coated ZnO nanoparticles for nanomolar detection of Al(III) and Zn(II) in semi-aqueous media, Tetrahedron Letters, 55 (2014) 6623.
16. R.N. Moussawi, D. Patra, Modification of nanostructured ZnO surfaces with curcumin: fluorescence based sensing for arsenic and improving arsenic removal by ZnO, RSC Adv., 6 (2016) 17256.
17. K. Singh, S. K. Mehta, Luminescent ZnO quantum dots as an efficient sensor for free chlorine detection in water, Analyst, 141 (2016) 2487.
18. S. Kaur, V.K. Bharadwaj, A. Kaur, N. Singh, N. Kaur, Differential recognition of anions with ZnO based urea coupled sensors, Materials Letters 107 (2013) 154.

19. S. Kaur, A. Kaur, N. Kaur, ZnO nanoparticles decorated with organic anion receptor: Selective recognition of sulphate anion, Materials Letters 100 (2013) 19.
20. Y. Zeng, L. Qiao, Y. Bing, M. Wen, B. Zou, W. Zheng, T. Zhang, G. Zou, Development of microstructure CO sensor based on hierarchically porous ZnO nanosheet thin films, Sens. Actuators B: Chem. 173 (2012) 897.
21. W. Li, X. Wu, N. Han, J. Chen, X. Qian, Y. Deng, W. Tang, Y. Chen, MOF derived hierarchical hollow ZnO nanocages with enhanced low concentration VOCs gas sensing performance, Sens. Actuators B: Chem. 225 (2016) 158.
22. A. Katoch, S.W. Choi, H. W. Kim, S. S. Kim, Highly sensitive and selective H_2 sensing by ZnO nanofibers and the underlying sensing mechanism, Journal of Hazardous Materials 286 (2015) 229.
23. K. Diao, M. Zhou, J. Zhang, Y. Tang, S. Wang, X. Cuib, High response to H_2S gas with facile synthesized hierarchical ZnO microstructures, Sensors and Actuators B 219 (2015) 30.
24. X. Chen, J. Liu, X. Jing, J. Wang, D. Song, Self-assembly of ZnO nanosheets into flower-like architectures and their gas sensing properties, Materials Letters112 (2013) 23.
25. T.Y. Chena, H.I. Chen, C.S. Hsu, C.C. Huang, J.S. Wu, P.C. Chou, W.C. Liu, Characteristics of ZnO nanorods-based ammonia gas sensors witha cross-linked configuration, Sensors and Actuators B 221 (2015) 491.
26. S. Ozturk, N. Kılınc, Z. Z. Ozturk, Fabrication of ZnO nanorods for NO_2 sensor applications: Effect of dimensions and electrode position, Journal of Alloys and Compounds 581 (2013) 196–201. (3.014)

27. Jing Wang, Xian Li, Yi Xia, Sridhar Komarneni, Haoyuan Chen, Jianlong Xu, Lan Xiang and Dan Xie, Hierarchical ZnO Nanosheet-Nanorod Architectures for Fabrication of Poly(3-hexylthiophene)/ZnO Hybrid NO_2 Sensor, ACS Appl. Mater. Interfaces (2016), 8, 8600−8607. ()
28. Yasin Sahin, Sadullah Ozturk, Necmettin Kılınc, Arif Kosemen, Mustafa Erkovan, Zafer Ziya Ozturk, Electrical conduction and NO_2 gas sensing properties of ZnO nanorods, Applied Surface Science 303 (2014) 90–96.
29. P. Su, T. Pan, Fabrication of a room-temperature NO2 gas sensor based on WO_3 films and WO_3/MWCNT nanocomposite films by combining polyol process with metal organic decomposition method, Mater. Chem. Phys. 125 (2011) 351-357.
30. C. Zhang, A. Boudiba, P. De Marco, R. Snyders, M. Olivier, M. Debliquy, Room temperature responses of visible-light illuminated WO_3 sensors to NO_2 in sub-ppm range, Sens. Actuators B 181 (2013) 395e401
31. X. Jie, D. Zeng, J. Zhang, K. Xu, J. Wu, B. Zhu, C. Xie, Graphene-wrapped WO_3 nanospheres with room-temperature NO_2 sensing induced by interface charge transfer, Sens. Actuators B 220 (2015) 201-209.
32. Xin Geng, Jiajun You, Jie Wang, Chao Zhang, Visible light assisted nitrogen dioxide sensing using tungsten oxide - Graphene oxide nanocomposite sensors, Materials Chemistry and Physics 191 (2017) 114-120
33. U. Yaqoob, A.S.M. Uddin, G. Chung, A high-performance flexible NO_2 sensor based on WO_3 NPs decorated on MWCNTs and RGO hybrids on PI/PET substrates, Sens. Actuators B 224 (2016) 738e746.

34. Cho P-S, Kim K-W, Lee J-H. NO2 sensing characteristics of ZnO nanorods prepared by hydrothermal method. J Electroceram 2006;17(2–4):975–8
35. Fowler JD, Allen MJ, Tung VC, Yang Y, Kaner RB, Weiller BH. Practical chemical sensors from chemically derived graphene. ACS Nano 2009;3:301–6.
36. Shubhda Srivastava, Kiran Jain, V N Singh, Sukhvir Singh, N Vijayan, Nita Dilawar, Govind Gupta and T D Senguttuvan, Faster response of NO_2 sensing in graphene–WO_3 nanocomposites, Nanotechnology 23 (2012) 205501 (7pp)
37. Sen Liu, Bo Yu, Hao Zhang, Teng Fei, Tong Zhang, Enhancing NO2 gas sensing performances at room temperature based on reduced graphene oxide-ZnO nanoparticles hybrids, Sensors and Actuators B 202 (2014) 272–278
38. H.Zhang, J.Feng, T.Fei, S.Liu, T.Zhang, SnO_2 nanoparticles-reduced graphene oxide nanocomposites for NO_2 sensing at low operating temperature, Sens. Actuators B190(2014)472–478.
39. S.Deng, V.Tjoa, H.M.Fan, H.R.Tan, D.C.Sayle, M.Olivo, S.Mhaisalkar, J.Wei, C.H. Sow, Reduced graphene oxide conjugated Cu_2O nanowire meso crystals for high-performance NO_2 gas sensor,J.Am.Chem.Soc.134(2012)4905–4917
40. Yan Xiao, Qiuyue Yang, Zhenyu Wang, Rui Zhang, Yuan Gao, Peng Sun, Yanfeng Sun, Geyu Lu, Improvement of NO2gas sensing performance based on discoid tin oxide modified by reduced graphene oxide, Sensors and Actuators B 227 (2016) 419–426
41. Fubo Gu, Rui Nie, Dongmei Han, Zhihua Wang, In_2O_3–graphene nanocomposite based gas sensor for selective detection of NO2 at room temperature, Sensors and Actuators B 219 (2015) 94–99

42. Xin Liu, Jianbo Sun, Xitian Zhang, Novel 3D graphene aerogel–ZnO composites as efficient detection for NO_2 at room temperature, Sensors and Actuators B 211 (2015) 220–226
43. Mei Chen, Zhihua Wang, Dongmei Han, Fubo Gu, Guangsheng Guo, High-sensitivity NO_2 gas sensors based on flower-like and tube-like ZnO nanomaterials Sensors and Actuators B 157 (2011) 565– 574
44. Fang-Tso Liu, Shiang-Fu Gao, Shao-Kai Pei, Shih-Cheng Tseng, Chin-Hsin J. Liu, ZnO nanorod gas sensor for NO2 detection, Journal of the Taiwan Institute of Chemical Engineers 40 (2009) 528–532
45. S.S.Shendage, V.L.Patil, S.A.Vanalakar, S.P.Patil, N.S.Harale, J.L.Bhosale, J.H.Kim, P.S.Patil, Sensitive and selective NO_2 gas sensor based on WO_3 nanoplates, Sensors and Actuators B: Chemical, http://dx.doi.org/10.1016/j.snb.2016.08.177
46. Sharadrao A. Vanalakar, Vithoba L. Patil, Namdev S. Harale, Sagar A. Vhanalakar, Myeng Gil Gang, Jin Young Kim, Pramod S. Patil, Jin Hyeok Kim, Controlled growth of ZnO nanorod arrays via wet chemical route for NO_2 gas sensor applications, Sensors and Actuators B 221 (2015) 1195–1201
47. A. Resmini, U. Anselmi-Tamburini, S.M. Emamjomeh, V. Paolucci, I.G. Tredici, C. Cantalini, The influence of the absolute surface area on the NO_2 and H_2 gas responses of ZnO nanorods prepared by hydrothermal growth, Thin Solid Films 618 (2016) 246–252
48. Rakesh K.Sonker, S.R.Sabhajeet, SatyendraSingh, B.C.Yadav, Synthesis of ZnO nanopetals and its application as NO_2 gas sensor. MaterLett(2015), http: //dx.doi.org/10.1016/j.matlet.2015.03.112
49. Yanghai Gui, Junhua Yuan, Weiming Wang, Jianbo Zhao, Junfeng Tian and Bing Xie, Facile Solvothermal Synthesis and Gas

Sensitivity of Graphene/WO3 Nanocomposites, Materials 2014, 7, 4587-4600

50. Xiaofang Pan, Xiaojin Zhao, Jiaqi Chen, Amine Bermak, Zhiyong Fan, A fast-response/recovery ZnO hierarchical nanostructure based gas sensor with ultra-high room-temperature output response, Sensors and Actuators B 206 (2015) 764–771.
51. J. Zhang, S. Wang, Y. Wang, M. Xu, H. Xia, S. Zhang,W. Huang, X. Guo, S. Wu, ZnO hollow spheres: Preparation, characterization, and gas sensing properties, Sensors and Actuators B 139 (2009) 411.
52. M. Breedon, M. J. S. Spencer, I. Yarovsky, Adsorption of NO2 on Oxygen Deficient ZnO(2-1-10) for Gas Sensing Applications: A DFT Study, J. Phys. Chem. C 114 (2010) 16603.
53. R.C. Pawar, J.-W. Lee, V.B. Patil, C.S. Lee, Synthesis of multidimensional ZnO nanostructures in aqueous medium for the application of gas sensor. Sens. Actuators B: Chem. 187 (2013) 323.
54. P. Rai, S. Raj, K.J. Ko, K.K. Park, Y.T. Yu, Synthesis of flower-like ZnO microstructures for gas sensor applications, Sens. Actuators B: Chem. 178 (2013) 107.
55. X. Wang, F. Sun, Y. Duan, Z. Yin, W. Luo, Y.A. Huang, J. Chen, Highly sensitive, temperature dependent gas sensor based on hierarchical ZnO nanorod arrays, J. Mater. Chem. C, 2015, 3, 11397.
56. D. C. Pugh, E. J. Newton, A. J. T. Naik, S. M. V. Hailes, I. P. Parkin, The gas sensing properties of zeolite modified zinc oxide, J. Mater. Chem. A, 2 (2014) 4758.
57. R.K. Sonker, S.R. Sabhajeet, S. Singh, B.C. Yadav, Synthesis of ZnO nanopetals and its application as NO_2 gas sensor, Materials Letters 152 (2015) 189.

58. J. Chang, M.Z. Ahmad, W. Wlodarski, E.R. Waclawik, Self-Assembled 3D ZnO Porous Structures with Exposed Reactive {0001} Facets and Their Enhanced Gas Sensitivity, Sensors. 13 (2013) 8445.
59. F.T. Liu, S.F. Gao, S.K. Pei, S.C. Tseng, C.H. J. Liu, ZnO nanorod gas sensor for NO_2 detection, Journal of the Taiwan Institute of Chemical Engineers 40 (2009) 528.
60. V. Galstyann, E. Comini, C. Baratto, G. Faglia,G. Sberveglieri, Nanostructured ZnO chemical gas sensors, Ceramics International41(2015)14239.
61. H.W. Kim, H.G. Na, Y.J. Kwon, H.Y. Cho, C. Lee, Decoration of Co nanoparticles on ZnO branched SnO_2 nanowires to enhance gas sensing, Sensors and Actuators B 219 (2015) 22.
62. R.C. Pawar, J.-W. Lee, V.B. Patil, C.S. Lee, Synthesis of multidimensional ZnO nanostructures in aqueous medium for the application of gas sensor. Sens. Actuators B: Chem. 187 (2013) 323.
63. P. Rai, S. Raj, K.J. Ko, K.K. Park, Y.T. Yu, Synthesis of flower-like ZnO microstructures for gas sensor applications, Sens. Actuators B: Chem. 178 (2013) 107.
64. . A.Z. Sadek, W. Wlodarski, K. Kalantar-zadeh, S. Choopun, ZnO nanobelt based conductometric H_2 and NO_2 gas sensors, in Proceedings of Sensors IEEE (2005), 1326
65. P. Rai, Y.-S. Kim, H.M. Song, M.K. Song, Y.T. Yu, The role of gold catalyst on the sensing behavior of ZnO nanorods for CO and NO_2 gases. Sens. Actuators B: Chem. 165 (2012) 133.
66. S. An, S. Park, H. Ko, C. Jin, W.I. Lee, C. Lee, Enhanced gas sensing properties of branched ZnO nanowires. Thin Solid Films 547, (2013) 24.

67. M.A. Chougule, S. Sen, V.B. Patil, Fabrication of nanostructured ZnO thin film sensor for NO2 monitoring. Ceram. Int. 38 (2012) 2685.
68. T.V. Kolekar, S.S. Bandgar, S.S. Shirguppikar, V.S. Ganachari, Synthesis and characterization of ZnO nanoparticles for efficient gas sensors. Arch. Appl. Sci. Res. 5 (2013) 20.
69. P. Rai, Y.T. Yu, Citrate-assisted hydrothermal synthesis of single crystalline ZnO nanoparticles for gas sensor application. Sens. Actuators B: Chem. 173 (2012) 58.
70. C. Liangyuan, B. Shouli, Z. Guojun, L. Dianqing, C. Aifan, C.C. Liu, Synthesis of ZnO–SnO_2 nanocomposites by microemulsion and sensing properties for NO_2, Sensors and Actuators B 134 (2008) 360.
71. Y.H. Navale, S.T. Navale, N.S. Ramgir, F.J. Stadler, S.K. Gupta, D.K. Aswal,V.B. Patil, Zinc oxide hierarchical nanostructures as potential NO_2 sensors, Sens. Actuators B 251 (2017) 551–563.
72. Y. Gonullu, G. C. M. Rodriguez, B.Saruhan,, M.Urgen, Improvement of gas sensing performance of TiO_2 towards NO_2 by nano-tubular structuring, Sens. Actuators B 169 (2012) 151– 160.
73. M.A. Chougule, S. Sen, V.B. Patil, Fabrication of nanostructured ZnO thin film sensor for NO_2 monitoring. Ceram. Int.38 (2012) 2685–2692.
74. V.V. Ganbavle, S.I. Inamdar, G.L. Agawane, J.H. Kim, K.Y. Rajpure, Synthesis of fast response, highly sensitive and selective Ni:ZnO based NO_2 sensor, Chem. Eng. J. 286(2015) 36-47.

75. V.V. Ganbavle, S.V. Mohite, J.H. Kim, K.Y. Rajpure, Effect of solution concentration on physicochemical and gas sensing properties of sprayed WO_3 thin films, Curr. Appl. Phys. 15 (2015) 84-93.

76. P. Rai, S. Raj, K.J. Ko, K.K. Park, Y.T. Yu, Synthesis of flower-like ZnO microstructures for gas sensor applications. Sens. Actuators B: Chem. 178 (2013) 107–112.

77. T.V. Kolekar, S.S. Bandgar, S.S. Shirguppikar, V.S. Ganachari, Synthesis and characterization of ZnO nanoparticles for efficient gas sensors. Arch. Appl. Sci. Res. 5 (2013) 20–28.

78. P. Rai, Y.-T. Yu, Citrate-assisted hydrothermal synthesis of single crystalline ZnO nanoparticles for gas sensor application. Sens. Actuators B: Chem. 173 (2012) 58–65.

Chapter 5

Zinc Oxide Architectures for Photocatalytic Treatment of Waste Water

5.1 Photocatalytic reduction of hexavalent chromium

5.1.1 Introduction

Heavy metals are a group of elements whose density lies above 5 g/cm^3 [1-2]. Even though the term “heavy metals” is a loosely defined one, it is frequently used for those metals whose occurrence in biome has adverse health and environmental impacts [3-4]. The most hazardous heavy metal pollutants such as Mercury (Hg), Lead (Pb), Chromium (Cr), Cadmium (Cd) and Arsenic (As) cause serious threat to living being [5-7]. Trace amounts of some heavy metals are essential for biological activities while its excess causes serious health hazards [8-9]. The higher concentration of these pollutants enter into the environment through natural as well as anthropogenic activities [10].

Different from organic pollutants, heavy metals are non-biodegradable and will persist and accumulate in the biosphere, which causes various environmental and health hazards [11]. The undesirable presence of these elements in drinking water is a critical issue. Hence water pollution caused by heavy metals is one of the foremost jeopardies the world is fretful about. Among the top most heavy metal pollutants, hexavalent chromium is a major environmental contaminant which is highly toxic, mutagenic and carcinogenic.

5.1.2 Hexavalent chromium: Sources and Noxious effects

Chromium exist in different oxidation states ranging from 0 to IV. Out of the various oxidation states, the most common forms are hexavalent chromium [Cr(VI)] and trivalent chromium [Cr(III)], which differ in terms of their toxicity, solubility and mobility [12-16]. Chromium (III) is an essential element, which enhances the production of insulin and takes part in metabolism of carbohydrate, fats and proteins. On the contrary, hexavalent form is a significant contaminant in the environment. Being a strong oxidizing agent, hexavalent chromium is found to be toxic, carcinogenic, genotoxic and mutagenic to human beings, animals, plants and microbial organisms [17-22]. Both natural and anthropogenic sources release hexavalent chromium to the environment. Chromium exposure can occur through water, air, soil and food, and it can diffuse rapidly through water and soil.

Hexavalent chromium is extensively used in electroplating and metal surface processes, inorganic pigment manufacturing, wood processing industry, chromate conversion coatings, anti-corrosion products and leather tanning [23-25]. Hexavalent chromium in the form of lead chromate, zinc chromate, barium chromate, calcium chromate, potassium dichromate, sodium chromate are used in paint and pigment manufacturing industries. It has been used as a colouring agent in plastics and ink. The use of chrome yellow, once widely used as a pigment in paint industry, waned due to health and environmental concerns.

The most important hexavalent chromium source is the leather tanning industries [26-30]. Hexavalent chromium compounds are used for the protection of hides (animal skins) from decay. It also helps to prevent aging due to moisture effect and make the hide more durable. Numerous tanning industries are operating worldwide and most of them have specific regulations for pollution control. The unauthorised and abandoned tanning industries in developing countries pose most of the Cr(VI) pollution. Tanning process requires a large amount of water for soaking hides and produces waste water contaminated with a verity of toxic chemicals including hexavalent chromium. The untreated effluents discharged directly to rivers and canals leading to severe environmental and health hazards.

Workers in tanning industries are expose to Cr (VI) through inhalation or dermal contact due to improper handling.

Chromium trioxide, zinc chromate, barium chromate etc. are used as an anti-corrosion agent in primers, paints and other surface coatings. Chrome plating on metal parts provides a decorative or protective coating. It is an integral part of stainless steel manufacturing since the addition of chromium in steel makes it more hard and corrosion resistant. People engaged in "hot works" such as welding on stainless steel and other chromium containing alloys of metals are more prone to hexavalent chromium exposure. The stainless steel actually contains chromium in its metallic form but the high temperature involved in hot works results in the oxidation of chromium metal to hexavalent form. During the production of ferrochrome, an iron-chromium alloy, a high concentration of hexavalent chromium is released into the air.

The widespread usage of chromium and its compounds as well as its improper ways of dumping to the environment, without adequate treatment creates serious problems that must be taken care of. Tannery workers, people dealing with high temperature welding works as well as workers handling chromium containing pigments and paints are in constant exposure to hexavalent chromium and at high risk of suffering the adverse effects. Numerous hematological disorders due to the abnormal features of blood cells are associated with occupational hexavalent chromium exposure [31, 32]. Workers exposed to hexavalent chromium compounds are more affected by genotoxic effects such as chromosomal aberrations [33]. The prolonged inhalation of hexavalent chromium is highly carcinogenic and cause lung cancer. Epidemiological studies suggested that there is an association between occupational exposure to hexavalent chromium and mortality due to lung cancer [34]. A huge amount of hexavalent chromium present in drinking water sources and tap water system are responsible for oral and small intestine cancer.

Hexavalent chromium transport in cells takes place through the sulphate transport mechanism due to the chemical resemblance between the two oxyanions [35]. The high solubility in water and rapid transportation through biological membranes stimulates the interaction with proteins and nucleic acid. This leads to the damage of DNA and other tissue structure. In addition to the carcinogenic effects, hexavalent chromium impose various health hazards in human being. It causes kidney and liver damage, irritant and inflammatory effects on the respiratory system, vomiting, diarrhoea, stomach upsets and ulcers in intestine, pulmonary congestions and edema, erosion and discoloration of teeth and skin allergies.

The highly soluble nature of hexavalent chromium in water also causes serious problems in plants [36, 37]. It can retard the growth and development of plant tissues, prevent seed germination, generate oxidative stress and pigment degradation. It also inhibit photosynthesis in plants by making ultra-structural changes in chloroplast. Hexavalent chromium has detrimental effect on many of the microorganisms present in the environment [38]. It is mutagenic to several bacteria and also inhibit their growth. It changes the morphology of gram positive and gram negative bacteria. Hexavalent chromium is a potential threat to aquatic life [39]. It causes cytotoxic effects to various fish species and has adverse effects such as suspended feeding, uneven swimming, decline in glycogen and proteins and haematological problems.

A new research from Blacksmith Institute (New York) suggested that India and Pakistan are at the highest risk of Chromium pollution [40]. Ranipet, a place near Chennai, Tamil Nadu is an urban area in India. A chromium production factory in Ranipet provides chromium salts to the local leather tanning industries [41]. The research conducted by Blacksmith Institute has observed that chromium waste produced from leather tanning process were collected in an open area. This causes the leaching of toxic hexavalent chromium through soil and eventually contaminate ground water system. This can adversely affect the local community which consumes water from this area.

Considering all these noxious effects, worldwide authorities have made strict rules and regulations for the use of chromium compounds and limited the concentration of Cr(VI) in water. International Agency for Research on Cancer (IARC) listed hexavalent chromium as a group I human carcinogen [42]. Environmental protection agency (EPA) also classified chromium as a carcinogen to living beings and has set the maximum level of this contaminant in drinking water as 0.1 mg/L for total chromium content [43]. According to WHO regulations, the maximum concentration of Cr (VI) allowed in drinking water is below 0.05 mg/L based on health concerns [44]. The world is serious about the hazards of hexavalent chromium and necessary steps are made to alleviate the problem.

5.1.3 Remedial measures for hexavalent chromium abatement

Hexavalent chromium exists in different forms in aqueous medium based on the solution pH, redox potential and the concentration of Cr(VI). The most plausible Cr(VI) species in aqueous solution are $Cr_2O_7^{2-}$, CrO_4^{2-}, H_2CrO_4, and $HCrO_4^{-}$. None of these hexavalent chromium species form insoluble compounds in aqueous medium. Hence, the separation of hexavalent chromium through direct precipitation is not possible. Even though Cr(VI) does not form insoluble precipitate, its trivalent form can be precipitated as $Cr(OH)_3$ on addition of a base. This can be easily separated from the aqueous phase. Thus reducing hexavalent chromium to its trivalent form simplifies its elimination from waste water, which necessitate its conversion to trivalent chromium. There were various methods adopted for the removal of hexavalent chromium form aqueous medium and some of them are discussed below.

a. Chemical reduction [45, 46]

Chemical reduction method involves the reduction of hexavalent chromium in waste water followed by its precipitation as $Cr(OH)_3$. Sulphur compounds and Iron salts are commonly used for the industrial chemical reduction of hexavalent chromium. The sulphur compounds used for this purpose are mainly sulphur dioxide and sodium sulphite. The iron compounds are generally iron (II) sulphates or chlorides. A strong acidic condition, i.e., $pH<3$ is required to effect the reduction process. Large amount of sludge formation is a disadvantage associated with this method. Sulphur compounds generates sulphur dioxide as a by-product which is considered as a major air pollutant. This method is not suitable for treating rinse water containing low concentration of Cr(VI).

b. Electrochemical reduction [46]

Electrochemical reduction is a clean technique since electrons are used for the reduction of heavy metal pollutant. The processes involved are electrocoagulation and electroflocculation. Electrocoagulation is the process in which the neutralisation of electric charge of the pollutant takes place, and the electroflocculation, where the hydrogen gas released from the cathode aids to carry the flocculated particle to the surface. Iron and Aluminium electrodes are mostly used in this method. Iron electrodes have maximum removal efficiency for Cr(VI). Minimal sludge formation is an advantage of this process. However, the high cost required for the process is a disadvantage.

c. Adsorption[47-49]

Adsorption is another method for the removal of hexavalent chromium from contaminated water. Various natural as well as synthetic materials are used as sorbents such as activated carbon, biomaterials, industrial waste, clay, zeolites etc. in this effect. The efficiency of adsorption depends on the nature of materials used. The high cost of activated carbon limits its use in adsorptive removal of hexavalent chromium from an economic point of view. The difficulty in regeneration of adsorbents is also a demerit associated with this process. Biosorption of heavy metal pollutant from waste water using various biosorbents such as algal biomass, microbial biomass, non-living plant and animal materials is a promising technique which is highly cost effective.

d. Bioremediation [50]

Bioremediation of industrial waste water containing hexavalent chromium is effected through microorganisms such as bacteria, fungi, and actinomycetes. *Pseudomonas* sp., a gram negative bacteria, was the first species reported for the reduction of chromium IV to chromium III. Gram positive chromium resistant bacterial strains isolated from tannery effluent can reduce 87% of Cr(VI) ions in 20 ppm dichromate solution within 72 hours [51]. In addition to the use of microorganisms, different algal species have been widely used for the bioremediation of hexavalent chromium. It has been considered as biosorbent for hexavalent chromium. Using microorganisms or algae as biological reduction agents for hexavalent chromium is an environmentally friendly method but the long reaction time reduces its large scale application.

e. Membrane Filtration [52, 53]

Heavy metals like chromium (VI) can be removed through the membrane filtration method. Different types of membranes used for this purpose are inorganic, liquid and polymeric membranes. The easy operation and the high efficiency are the attractions of this method. Ultrafiltration, reverse osmosis, nanofiltration and electrodialysis are the different membrane filtration techniques. The operational cost associated with this process and the membrane fouling are major drawbacks of membrane filtration.

f. Ion exchange technique [54, 55]

The separation process in which an insoluble substance removes positively or negatively charged ions from an electrolyte and releases an equivalent amount of other ions with the same charge. Different ion exchange resins such as Dowex 2-X4, Ambersep 132 and solvent impregnated resin with aliquat 336 were used for the uptake of hexavalent chromium form waste water. The shortcomings of this techniques include the loss of sensitivity when targeting ions, regeneration of resins using chemical reagents, and the production of secondary pollutants during the regeneration of resins.

The removal of Cr (VI) using conventional methods such as chemical reduction followed by precipitation are inefficient in the sense that they require large amount of chemicals to reduce Cr(VI) in its acceptable levels to discharge and produces hazardous byproducts. The high operational cost of electrochemical methods, ion exchange, membrane filtration etc. limits their application in large scale. Here arises the need of an efficient and economic technology that leads to the conversion of toxic hexavalent chromium to less toxic trivalent chromium.

g. Photocatalytic reduction of hexavalent chromium

An alternative method for the conversion of hexavalent chromium into its less toxic trivalent form that has gained much attention in recent years is heterogeneous photocatalysis. Photocatalysis has long been applied to treat organic and inorganic contaminants in waste water. Hexavalent chromium removal by heterogeneous photocatlytic reduction using a semiconductor catalysts is an effective, innovative and clean technology. The main attraction of this method is the energy source required for the treatment of waste water is a reliable and renewable one, i.e., the solar energy.

The photocatalytic reduction of hexavalent chromium using semiconductor catalyst was first reported by Yoneyama et al. in 1979 [56]. Semiconductors such as TiO_2, ZnO, Fe_2O_3, SnS_2 etc. were used by many researchers for the photocatalytic treatment of waste water laden with Cr(VI). TiO_2 is one of the most extensively studied photocatalysts for the degradation of organic as well as inorganic pollutants [57-62]. The facet enhanced photoreduction of Cr(VI) by surface fluorinated anatase TiO_2 nanosheets were studied by He et al. [63]. Even though TiO_2 is an efficient photocatalyst, the removal of catalyst from the medium after treatment is difficult [64, 65]. In this aspect, ZnO, an alternative for TiO_2 is an emerging candidate for photocatalysis [66-69]. There were reports suggesting that ZnO is more active than TiO_2 [70].

5.1.4 Mechanism of photocatalytic reduction of Cr(VI)

The photocatalytic reduction of hexavalent chromium proceed through the following mechanism. When light photons having suitable energy strike the zinc oxide surface, electrons form the valance band (VB) is excited to the conduction band (CB) leaving behind holes in the valence band. Thus the promotion of electrons from VB to CB results in the formation of electron-hole pairs. These holes and electrons are responsible for the oxidation and reduction of adsorbed species on the semiconductor surface.

Hexavalent chromium, being a strong oxidizing agent, easily gets reduced to trivalent chromium by the electrons produced in the semiconductor metal oxide surface. The following equations represent the reactions involved in photocatalytic reduction of hexavalent chromium:

$$ZnO+h\nu \rightarrow ZnO\ (e^-+h^+) \qquad (1)$$

$$Cr_2O_7^{2-}+14\ H^+ + 6e^- \rightarrow 2\ Cr^{3+}+7H_2O \qquad (2)$$

A schematic representation of the mechanism of photoreduction of hexavalent chromium is shown in Figure 1.

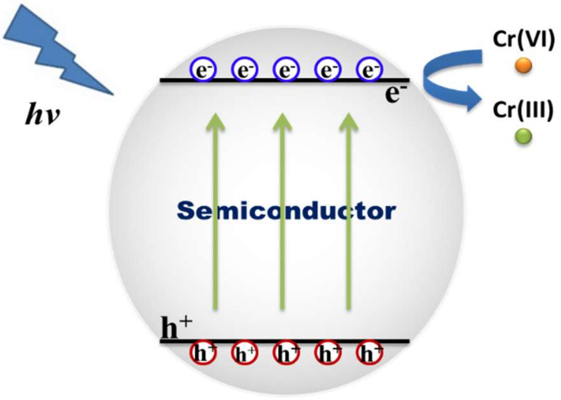

Figure 1. Mechanism of photoreduction of hexavalent chromium

5.1.5 Effect of organic compounds as hole scavengers

Electron-hole recombination is a major problem associated with the photocatalysis. It has been well established that organic compounds have significant role in controlling the photocatalytic reduction of hexavalent chromium [71-73]. The presence of suitable organic compounds, which can capture holes from the reaction medium, enhance the photoreduction. Methanol can act as sacrificial electron donor and hole scavenger in the photoreduction of hexavalent chromium, as reported by various researchers. But its toxicity concern limits its usage. Humic acid was used as a photosensitizer in the photoreduction of Cr(VI) to Cr(III). The rate of photocatalytic reduction of hexavalent chromium is largely increased by the presence of phenol and chlorophenol [74].

Different organic compounds such as citric acid, phenol, EDTA and oxalic acid has been used to evaluate their influence on the photoreduction efficiency of zinc oxide nanorods supported on kaolin [75]. It was found that only citric acid enhances the activity. The adsorption of other organic compounds on the active sites of the catalyst inhibit the photoreduction efficiency of the system. The same organic compounds have been used by Naimi-Joubani et al. for ZnO/TiO_2 composite [73]. But they found that all these organic compounds have an inhibition effect on the photocatalytic reduction of hexavalent chromium. This can be explained by two reasons i.e., (1) the adsorbed organic molecules on the active sites of the catalyst can hinder the photoreduction of hexavalent chromium; (2) The hole scavenging effect of these organic compounds was not greater than its hindering effect.

Addition of organic dyes in the reaction medium facilitate the photocatalytic reduction of hexavalent chromium. Yu et al. investigated the visible light photoreduction of hexavalent chromium on ZnO/CuO composite [76]. They have found that the presence of Rhodamine B in Cr(VI) solution has significantly increased the photoreduction process.

5.1.6 Zinc oxide as a photocatalyst for chromium reduction

As an n-type semiconductor with a wide band gap ~ 3.37 eV and large exciton binding energy, ZnO is gaining much attention for the past few decades. ZnO is widely used in technological applications in various fields like sensors, photocatalysis, optoelectronic devices, solar cells and so on [77-80]. There were a few reports about the photocatalytic reduction of Cr(VI) using zinc oxide as catalyst [81-85]. Jin et al. have synthesized porous single crystalline ZnO nanoplates and discussed in detail the synergistic effect of phenol on ZnO for the photoreduction of hexavalent chromium [65]. Kaoilin supported ZnO was used by Siboni et al. and the effect of different factors on photoreduction of Cr(VI) was well studied [75]. Laser induced photoreduction of Cr(VI) using zinc oxide catalyst was investigated by Qamar and co-workers [86]. Zinc oxide nanostructures have been synthesized by sonochemical method using different precursor solvents [82]. The higher rate of photoreduction of hexavalent chromium is shown by zinc oxide system prepared using ethanol as precursor solvent.

5.1.7 Results and discussion

Various factors that decide the photoctalytic reduction properties of zinc oxide include its structural characteristics, surface area, catalyst dosage, initial concentration of Cr(VI) solution, pH of the medium, hole scavengers etc. We have carried out the photoreduction studies using six different zinc oxide architectures, namely zinc oxide nanoparticles (ZP), nanosheets (ZS), nanorods (ZR) and flower like structures composed of nanosheets (ZSF), nanoparticles (ZPF) as well as nanorods (ZRF) as their building units. The influence of these aforementioned factors for photocatalytic reduction of hexavalent chromium is described in details.

a. Influence of morphology on photocatalytic reduction of hexavalent chromium

The effect of morphology on photocatalytic removal of hexavalent chromium has been studied by conducting the experiments using the six morphologically different zinc oxide structures. The photoreduction of 30 ppm Cr(VI) aqueous solution at pH 4 and a catalyst dosage of 1 g/L was conducted using all the catalyst systems. After the photocatalytic reduction of hexavalent chromium, absorbance at 540 nm is monitored for determining the amount of Cr(VI) ions in solution using the diphenyl carbazide method.

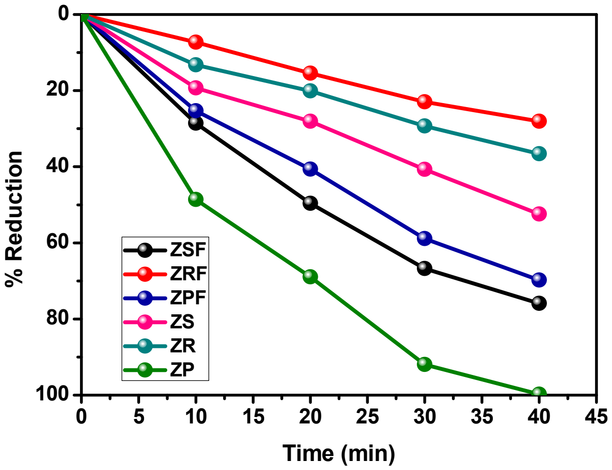

Figure 2. Photocatalytic reduction of hexavalent chromium by ZnO systems (Catalyst dosage: 1 g/L; [Cr(VI)]: 30 ppm; pH: 4)

Figure 2 illustrates the morphological influence of zinc oxide systems on the photoreduction process. Negligible amount of adsorption of Cr (VI) on the catalyst surface was observed. It is obvious from Figure 2 that the ZnO nanoparticles (ZP) are more active towards photocatalytic reduction of Cr(VI) than the other structures, viz., nanosheets (ZS) as well as nanorods

(ZR) and flower like zinc oxide structures. Complete reduction was observed within 40 minutes of irradiation in presence of ZP system with particle morphology. The photoreduction efficiency of other zinc oxide samples within 40 minutes was noted to be 75.89, 69.8, 52.45, 36.6 and 28.09% respectively, for ZSF, ZPF, ZS, ZR and ZRF systems.

The order of activity of the prepared systems for the photocatalytic reduction of hexavalent chromium depends on the surface area and the electron-hole recombination efficiencies. The smaller particle size and the highest surface area (40.34 m^2/g) of zinc oxide nanoparticles among the catalyst systems are the key factors that determine the enhanced photocatalytic activity. A large number of surface sites are exposed to UV light for the photoreduction of hexavalent chromium. Moreover, it is evident from the PL studies that ZP system with comparatively lower intensity PL spectrum exhibits lower electron hole recombination efficiency. This will produce more number of available electrons for the photoreduction process.

ZSF system composed of nanosheets assembled flower like architecture stands second in the activity series. From BET analysis the surface area of the system was found to be 8.09 m^2/g, the lowest surface area among the six morphologically different zinc oxide structures. Besides the lowest surface area value, it also possessed the lowest electron-hole recombination efficiency among the catalyst systems. Hence, the reason for the higher activity of ZSF system can be attributed to its lowest electron-hole recombination efficiency which is obvious from the photoluminescence spectra. Nanoparticles assembled flower like structure occupies third position in the photoreduction efficiency series. The higher surface area (20.32 m^2/g) of the system substantiates the efficiency of ZPF system to photoctalytically reduce hexavalent chromium. Zinc oxide nanosheets (ZS), nanorods (ZR) and nanorods assembled flowers (ZRF) possess lower photoreduction abilities due their low surface area values and high electron-hole recombination efficiencies. The fast rate of electron-hole recombination and the lower adsorption sites available for photoreduction of hexavalent chromium make ZRF system the least efficient.

b. Influence of pH on photoreduction of Cr(VI) using ZnO nanoparticles (ZP)

As ZnO nanoparticles (ZP) are observed to be the most efficient among the series, further studies were conducted using this system. The pH of the solution has significant role in the photoreduction of hexavalent chromium. To study the influence of PH on photoreduction, the reaction was carried out at three different pH such as 4 (acidic), 7(neutral) and 10 (basic) at constant catalyst dosage (1 g/L) and initial chromium concentration (30 ppm). It can be observed from Figure 3 that acidic pH favours the reaction more than the neutral and basic pH. The reaction was completed within 40 minutes at pH 4 and only ~77% and ~64% reduction were achieved respectively in neutral and basic pH at the same time interval.

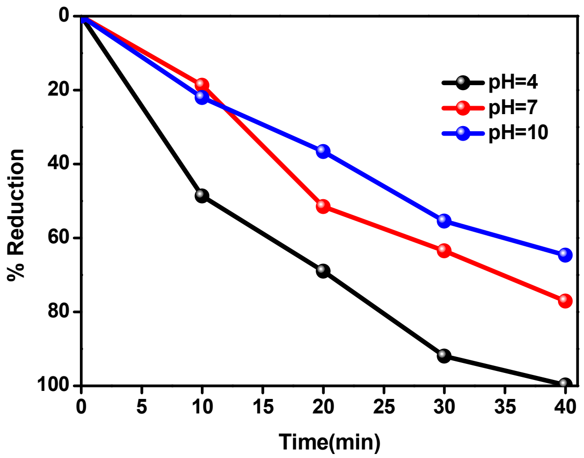

Figure 3. Effect of pH on the photocatalytic activity of ZP system (Catalyst dosage: 1 g/L; [Cr(VI)]: 30 ppm)

This may be attributed to the conversion of $Cr_2O_7^{2-}$ to CrO_4^{2-} as the initial pH changes from 4 to 10 [75]. The mechanism involved in Cr(VI) reduction in different medium is as follows:

Acidic: $Cr_2O_7^{2-} + 14\,H^+ + 6e^- \longrightarrow 2Cr^{3+} + 7H_2O$

Neutral: $CrO_4^{2-} + 8\,H^+ + 3e^- \longrightarrow Cr^{3+} + 4H_2O$

Basic: $CrO_4^{2-} + 4H_2O + 3e^- \longrightarrow Cr(OH)_3 + 5OH^-$

It is clear that at higher pH, $Cr(OH)_3$ species get deposited on the surface of the photocatalyst thereby reducing the activity.

c. Influence of initial Cr(VI) concentration

The dependence of photocatalytic removal on initial chromium concentration is evaluated by varying the concentration of dichromate solution from 20 to 50 mg/L. The pH of the solution was kept constant at 4 and a catalyst dosage of 1 g/L was used. It is obvious from Figure 4, that by increasing the initial concentration of Cr(VI) from 20 to 50 mg/L, the % reduction decreased from 99.77 to almost 44.23% within 40 minutes. The increased Cr(VI) concentration has an inhibitive effect on the photocatalytic activity of zinc oxide nanoparticles. This may be due to the lack of active sites available in zinc oxide catalyst for the photoreduction process. The number of Cr(VI) ions increases with increase in dichromate concentration and more number of surface sites is needed for the adsorption and subsequent photoreduction of these ions.

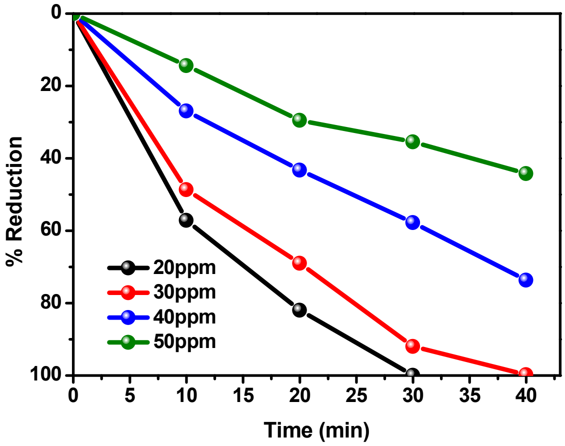

Figure 4. The effect of initial Cr(VI) concentration on the photocatalytic efficiency of ZP system (Catalyst dosage:1 g/L; pH: 4)

d. Influence of hole scavengers

Hole scavengers have got profound influence in these type of reactions. The role of organic compounds as hole scavenger is well established in previous studies [26, 27]. It was noted that hole scavengers have much influence in the activity of ZnO catalyst. Different organic compounds such as humic acid, phenol, methanol, oxalic acid etc. were used as hole scavengers. To assess the influence of organic compounds on the photoreduction of Cr(VI), we have chosen ethanol and phenol as hole scavengers. The concentration of ethanol and phenol in the reaction medium was adjusted to be 10 mg/L while the catalyst dosage, initial chromium concentration and pH were kept constant at 1 g/L, 30 mg/L and 4.

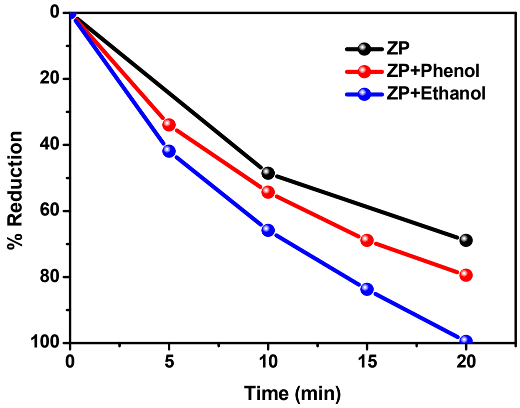

Figure 5. Effect of hole scavengers on the photoreduction of hexavalent chromium

It was observed from the Figure 5 that the addition of ethanol to the reaction medium substantially enhances the photoreduction efficiency of zinc oxide nanoparticles (ZP system). The reduction of hexavalent chromium is completed within 20 minutes in the presence of ethanol, while it took 40 minutes in its absence under similar experimental conditions. In the presence of phenol, 80% photocatlytic reduction of hexavalent chromium was observed within 20 minutes. The reason for the enhanced photoreduction in presence of ethanol and phenol is due to the extraction of holes generated in the valence band of ZnO by the organic compound thereby decreasing the possibility of electron-hole recombination. Ethanol is more efficient than phenol. This may be due to the interference of adsorbed phenol molecules on the active sites of the catalyst for the photoreduction of hexavalent chromium. A schematic representation of the mechanism of photo-reduction in the presence of ethanol is given in Figure 6.

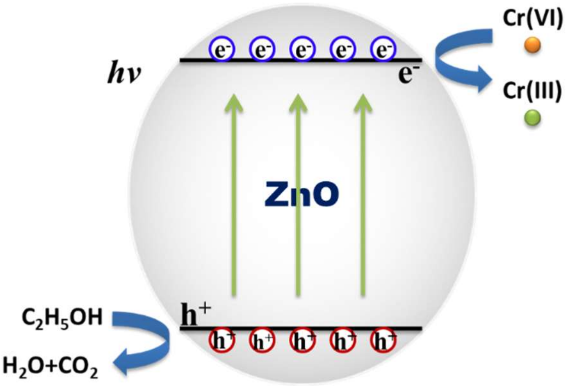

Figure 6. Schematic representation of photoreduction mechanism in the presence of ethanol

e. Reusability of the catalyst

The reusability of the catalyst, zinc oxide nanoparticles (ZP), was also investigated by conducting the experiments over 5 cycles. It was found that the photocorrosion of the catalyst was negligible. The results in this regard are shown in Figure 7, which hints to the fact that the material can successfully function as a stable and reusable efficient catalyst for the photoreduction reactions.

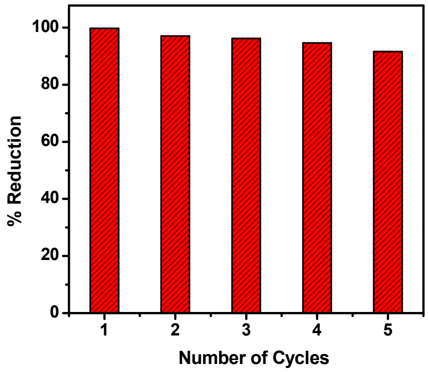

Figure 7. Reusability of ZP system over five cycles.

5.1.8 Concluding remarks

Zinc oxide, a well-known candidate for the photocatalysis, was chosen for the photoreduction of hexavalent chromium. The present study deal with the synthesis, characterization and photoreduction of Cr(VI). Six morphologically different zinc oxide architectures were exploited for the photocatalytic reduction of hexavalent chromium. The results indicated that the catalyst system with particle like morphology i.e., ZP system was more active towards the photoreduction of hexavalent chromium and the activity order is ZP > ZSF > ZPF > ZS > ZR > ZRF. Surface area together with electron-hole recombination efficiency play significant role in tuning the catalytic activity. The higher photocatalytic activity of ZP system was attributed to its large surface area (40.34 m^2/g) among the systems and comparatively low electron-hole recombination efficiency. Our study revealed that the pH of the solution, initial Cr(VI) concentration and hole scavengers have remarkable role in the photoreduction process of hexavalent chromium. In the presence of ethanol as hole scavenger, the activity of the ZnO-PVP system was enhanced to a greater extent. The system is also found to be stable over five cycles of photoreduction processes.

5.2 Photocatalytic degradation of Rhodamine B

A brief introduction on water pollution from textile industries especially organic dyes as the contaminant is discussed in chapter 1. Here we are concentrating on the photocatalytic degradation of the dye, Rhodamine B using six morphological variation of zinc oxide. Modification of the highest active zinc oxide system is carried out using different weight percentages of silver, copper and iron. The detailed discussion on the results in this regard is as follows:

Results and discussion

5.2.1 Effect of Morphology on photocatalytic degradation of Rhodamine B

The prepared zinc oxide flower like architectures with three different morphologies viz, nanosheet assembled flowers (ZSF), nanorods assembled flowers (ZRF) and nanoparticle assembled flowers (ZPF) as well as their nano-building units namely nanosheets (ZS), nanorods (ZR) and nanoparticles (ZP) were used for the photocatalytic degradation of Rhodamine B, an organic cationic dye, so as to study the influence of morphology on the activity. It is noted that the photolysis of Rhodamine B (without the catalyst) was negligible. After adding the catalyst system to Rhodamine B solution, the mixture was stirred for 20 minutes in dark to reach the adsorption desorption equilibrium. There was only 2.7% reduction in the concentration of dye after stirring in the dark due to adsorption. The initial concentration of the dye was set up by considering this amount adsorbed. The absorption spectra of Rhodamine B during photodegradation in presence of ZnO systems are shown in Figure 1.

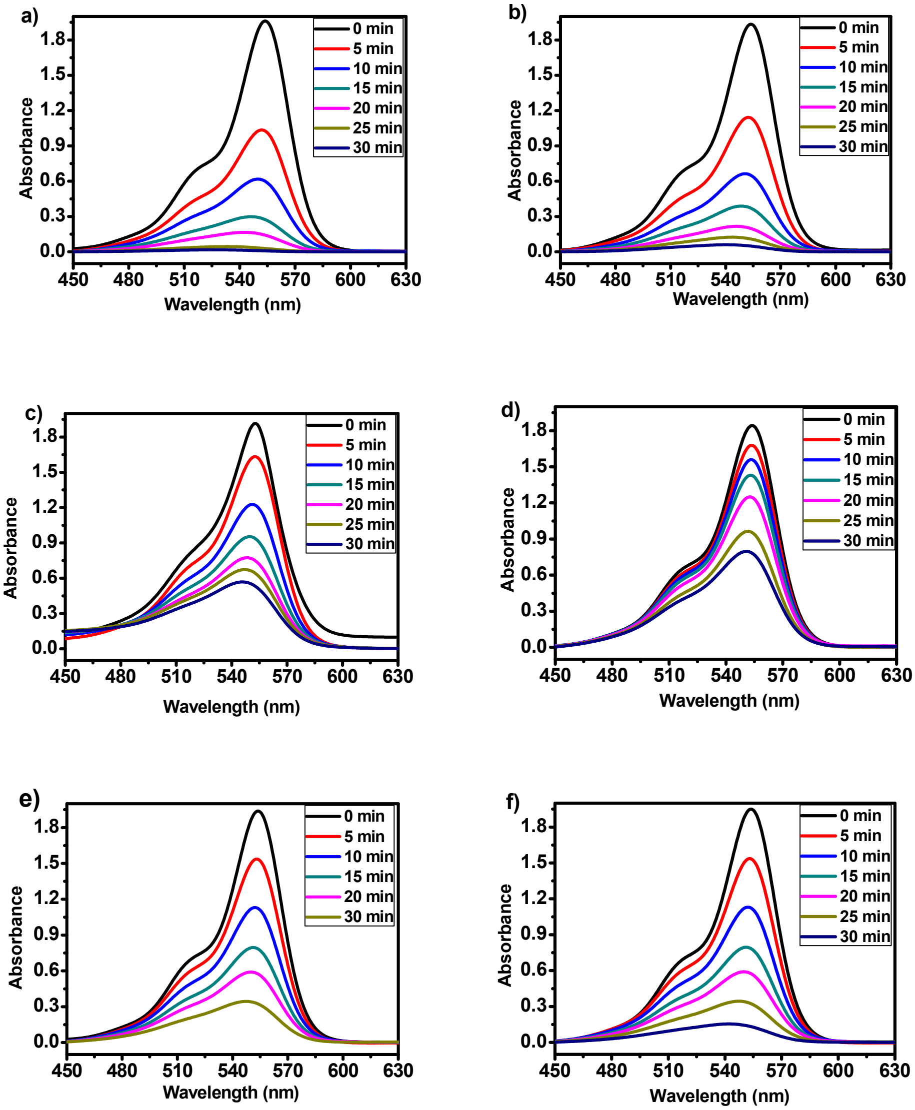

Figure 1. Absorption spectra of photodegradation of Rhodamine B in presence of (a) ZSF, (b) ZS, (c) ZRF, (d) ZR, (e) ZPF and (f) ZP catalyst systems. (Catalyst dosage:1 g/L; [RhB]:10 ppm)

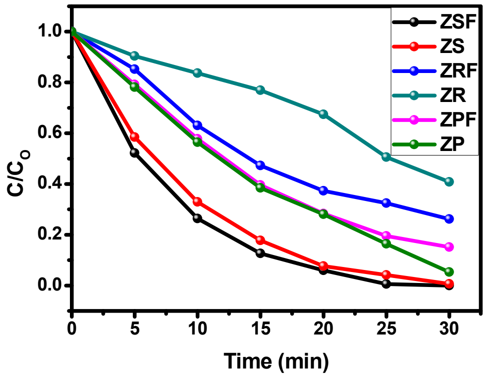

Figure 2. Plot of C/C$_o$ as a function of time

It is clear from the figure that the absorbance intensity at 554 nm decreases as the time elapses. Both zinc oxide nanosheets and flower like structure with nanosheets assembled petals were found to be highly active in the photodegradation of Rhodamine B when compared to other four morphologically different structures. Percentage degradations of 99.56 % and 100% were obtained within 30 minutes of irradiation time for ZS (nanosheets) and ZSF (nanosheet flower) systems respectively. 94.7% degradation of Rhodamine B was achieved by ZP system with particle like morphology. The particle assembled flower like system (ZPF) come in the fourth position of activity with a percentage degradation of 84.89%. Both the nanorods assembled flower like (ZRF) system and nanorods (ZR) were found to be comparatively least efficient in the sense that they possess only 73.8 and 59.2% of Rhodamine B degradation within the same time interval of 30 minutes. The relative concentration C/C$_o$ of Rhodamine B against irradiation time is outlined in Figure 2. The progress of reaction at 30 minutes is monitored for comparing the systems. The activity within 30 minutes follows the order ZSF > ZS > ZP > ZPF > ZRF > ZR.

The nanosheets assembled flower-like ZnO architecture exhibited a strong morphology induced enhancement in photocatalytic performance and show a significantly improved photocatalytic efficiency in the photodegradation of Rhodamine B compared with the nanobuilding units viz., nanoparticles, nanosheets, and nanorods as well as the flower like structures composed of nanoparticles and nanorods.The surface active planes in petals constituted by nanosheets as well as the unique hierarchical structure of ZSF system make it the best candidate for photocatalytic degradation of Rhodamine B as suggested by Zhao et al [87]. They have observed excellent photocatalytic activity for such ZnO flowers, which supports and strengthens our results. Almost complete conversion was achieved within 30 minutes under the prevailing conditions.

Some reports suggest that ZnO systems with active zinc polar (0001) planes are capable of adsorbing photoreactive species on their surface and enhance the photocatalytic activity [88]. It is worth mentioning that the hierarchical structure provides a suitable platform for the effective separation of electron-hole pairs in ZSF system. This is evident from the photoluminescence spectra. The lowest PL intensity is observed for ZSF system with nanosheets interlaced flower like structure. Even though the surface area of ZSF system is found to be the lowest (8.09 m^2/g) compared to other systems, the unique flower like structure with well oriented active surface planes and the low electron-hole recombination efficiency make the system prominent in photocatalytic activity. It was noticed that when compared with other reports on photocatalytic degradation of dye molecules over ZnO based structures, the flower like ZnO system reported herein stands superior by all means [89, 90].

Zinc oxide nanosheets (ZS system) also possess comparable activity (99.56%) to ZSF system with nanosheets assembled flower like architecture. This can be attributed to the well oriented active surface planes as well as the enhanced surface area (13.71 m^2/g) of the system. Zinc oxide nanoparticles (ZP) possess the highest surface area (40.34 m^2/g) among the six morphologically different structures. The significantly high surface area of ZP system arising due to the smallest particle size accounts for the third position of this system in the order of activity. The second highest surface area (20.32 m^2/g) is credited to ZPF system having particle assembled flower like structure. It has shown a degradation efficiency of 84.89% towards Rhodamine B dye within 30 minutes of UV irradiation. The prominent non-polar surfaces, low surface area as well as the high electron-hole recombination efficiency of zinc oxide nanorods and nanorods assemble flowers ZRF and ZR systems were responsible for the lower photocatalytic activity of these systems.

5.2.2. Reusability ZSF and ZS systems

The flower like structure has an added advantage that they are highly stable under the selected reaction conditions. The hierarchical assembly of flower like architectures and the large particle size made the easy sedimentation of ZSF in the reaction medium after photocatalysis. This enables the system for recycling purpose. The recyclability test was carried out over five cycles of reactions. Even after the five consecutive cycles of reactions the structure remains unaltered and the activity is almost retained. ZS system with sheet like morphology is also reusable, but the difficulty in separation of the particles from the reaction medium result in the reduction of activity in further reaction cycles. Thus it is proved that hierarchical structures are more stable towards photocorrosion than its monomorphological constituent parts. Figure 3 illustrates the recycling property of both the prepared systems.

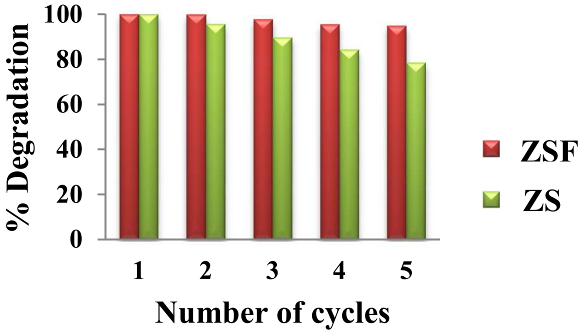

Figure. 3. Recycling ability of the prepared systems

5.2.3. Comparison of ease of sedimentation of ZSF, ZS and P25 systems

It is essential to remove the catalyst from the reaction medium after the photocatalytic degradation of organic pollutants. From the economical point of view, an efficient environmental friendly catalyst must be easily separated and recovered for further use from the medium after photocatalysis. The advantage of our system over the well explored TiO_2 is that, ZnO requires minimum time for sedimentation. The ZSF system can be easily settled out from the reaction medium without any centrifugation process. Figure 4 displays the digital image of normal sedimentation process for ZSF and P25. The natural sedimentation occurs within 1 minute for ZSF. Even after 12 hours, no noticeable sedimentation is observed for P25. For ZS system, the sedimentation occurs within 10 minutes after the first cycle of reaction. The unique flower like structure of ZSF system made it highly stable and facilitate the easy recovery of catalyst from reaction medium. All the above factors contribute to the practical applicability of the prepared zinc oxide system (ZSF) for the removal of toxic organic dyes from aquatic environment.

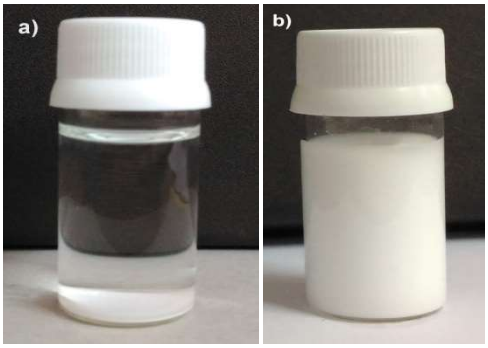

Figure 4. Photographs of sedimentation separation of ZSF after 1 minute (a) and P25 TiO_2 after 12 hours (b).

5.2.4 Modification of ZSF system for a better photocatalyst

Zinc oxide nanosheets self-assembled flower like system possesses the highest photocatalytic efficiency as well as it is stable towards photocorrosion. It can be easily recovered from the reaction medium after the photocatalytic dye degradation and have good recycling properties. Hence, we have modified zinc oxide nanosheet assembled flower like architectures for improving its photocatalytic efficiency. The major problem confronted by zinc oxide as a photocatalyst is the higher rate of electron-hole recombination, which results in the lowering of photocatalytic efficiency. To tackle with this drawback, we have to introduce foreign materials in the zinc oxide matrix which can effectively trap electrons and inhibit the electron-hole recombination to some extent.

Herein we have incorporated 3 weight percentage of copper, iron and silver in zinc oxide nanosheet assembled flower like system. Photodeposition and wet impregnation methods were adopted for the synthesis. The details of the synthetic steps are presented in Chapter 2.

5.2.5 Characterization of the modified systems

a. X-Ray diffraction analysis

The X-ray diffraction analysis of zinc oxide nanosheet assembled flowers and its modified analogues (silver, copper and iron modified) were portrayed in Figure 5. The pure zinc oxide system possessed the characteristics XRD pattern for hexagonal wurtzite structure (Figure 5a). The 2θ values of corresponding crystal planes are as follows: 31.7° (100), 34.3° (002), 36.2 (101), 47.4 (102), 56.5 (110), 62.8 (103) and 67.8 (112) (JCPDS No. 36-1451). Figure 5b represents the XRD pattern of silver loaded ZSF system. Three additional peaks located at 2θ values 38.1, 44.2 and 64.4 correspond to (111), (200) and (220) crystal planes in face centre cubic lattice (fcc) of metallic silver (JCPDS No. 04-0783). For copper loaded zinc oxide system a very low intense peak at 2θ value 38.6° is observed besides the zinc oxide wurtzite peaks (Figure 5c). This can be assigned to the (111) plane of monoclinic copper oxide. The results show that copper in its oxide form is highly dispersed in the ZSF matrix. Figure 5d clearly indicates the incorporation of Fe_2O_3 in zinc oxide lattice. The peaks at 2θ values 30.02, 35.18, 42.82 and 53.26 correspond to (220), (311), (400) and (422) planes of γ-Fe_2O_3.

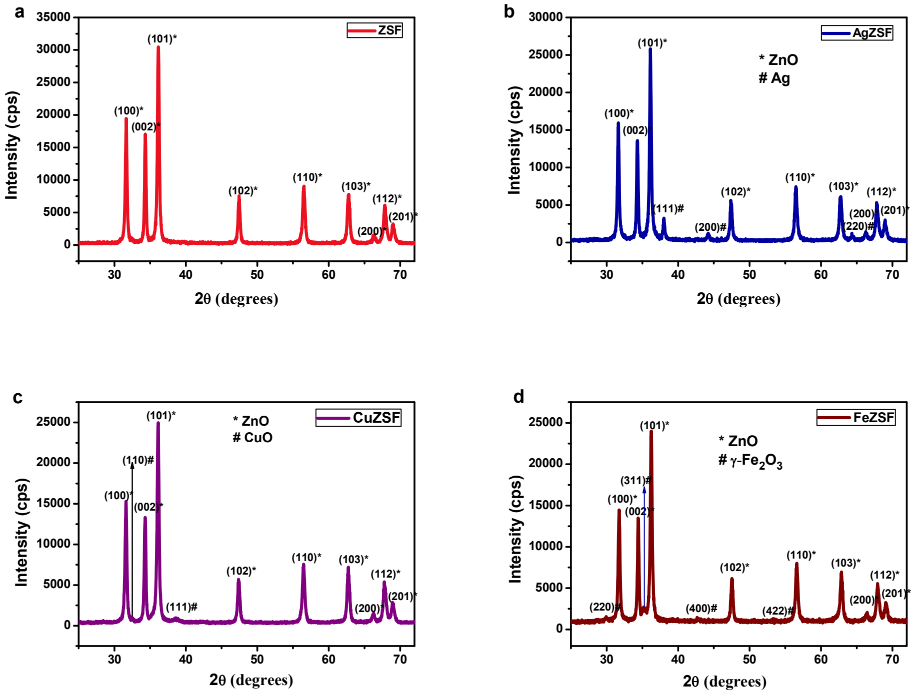

Figure 5. XRD pattern of ZSF system (a); modified ZSF system with silver (b); copper (c) and iron (d).

b. Scanning electron microscopy analysis

The scanning electron microscopic images of zinc oxide flower like system composed of nanosheets as building units and its modified analogues with silver, copper and iron were displayed in Figure 6. ZSF system loaded with silver has comparable morphology with that of the parent system (Figure 6b). The self-assembled nanosheets forming flower like structure is obvious form Figure 6a and 6b and the presence of silver does not alter the morphology of ZSF system. Copper and Iron loading into the zinc oxide flower like matrix changes its morphology to some extent. A distortion in the self-assembled nanosheets were observed in both the cases. The particles were aggregated together and the exposed nanosheets in flower like structures is almost lost in Figure 6c and 6d which represents copper and iron loaded ZSF systems respectively.

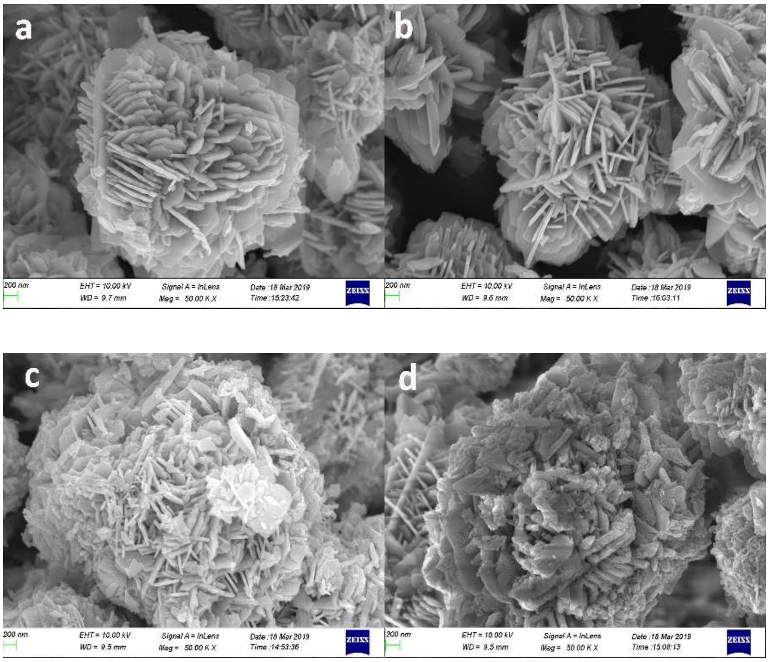

Figure 6. FESEM images of Zinc oxide systems ZSF (a) and the modified ZSF systems AgZSF (b); CuZSF(c); and FeZSF (d)

c. Surface area analysis

The BET surface area analysis by nitrogen adsorption studies further substantiate the results observed from SEM images. The parent ZSF system exhibited a surface area value of 8.09 m^2/g. The surface area of silver loaded system increases from the parent system and the value is 13.648 m^2/g. The surface area values decreases than that of ZSF system for copper and iron loaded systems. The corresponding surface area values are 7.70 m^2/g and 7.39 m^2/g for CuZSF and FeZSF systems respectively. This clearly indicates the aggregation of particle in both copper and iron loaded systems.

d. UV-Vis Diffuse Reflectance Spectroscopy

UV- Visible diffuse reflectance spectra were recorded in the wavelength range 250-700 nm. The absorption spectra and the corresponding Kubelka-Munk plots of ZSF and modified ZSF systems are shown in Figures 7a and 7b respectively. A red shift in absorption is observed for all the modified analogues when compared to ZSF system. Pure zinc oxide absorbs only in the UV region whereas Ag, Cu and Fe analogues of ZSF system has absorption in the visible region also. The band gap values calculated for zinc oxide nanosheet assembled flower like system is 3.18 eV. For AgZSF, CuZSF and FeZSF, the band gap values are 3.17 eV, 2.93 eV and 3.05 eV respectively, as expected from the shift in absorbance values.

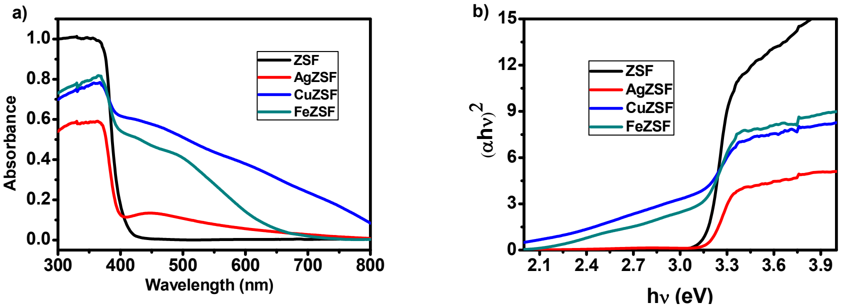

Figure 7. UV-Visible absorption spectra (a) and corresponding Kubelka-Munk plot (b) of ZSF and modified systems.

e. Photoluminescence study

The room temperature photoluminescence spectra of nanosheet assembled flower like architecture and the silver, copper and iron loaded systems were plotted in Figure 8. The spectra were measured at an excitation wavelength of 325 nm. The near band edge (NBE) emission responsible for the recombination of free excitons lies around 380-420 nm. It is apparent from the figure that the intensity of PL spectra of modified systems decreases from the parent ZSF system. The least intense PL spectra is observed for silver loaded ZSF system. This clearly indicates the low electron-hole recombination efficiency in AgZSF system, which is desirable for a good photocatalyst.

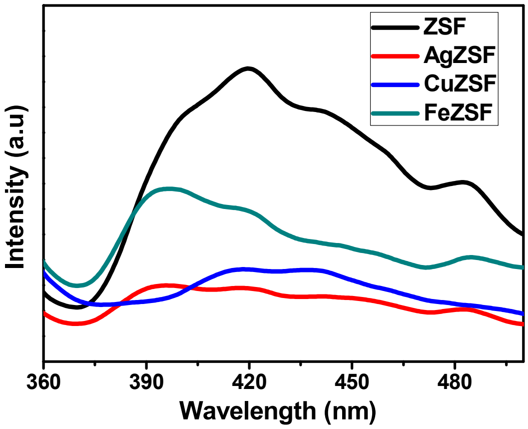

Figure 8. Photoluminescence spectra of ZSF and modified ZSF systems

5.2.6 Photocatalytic degradation of Rhodamine B using Cu, Fe and Ag loaded ZSF systems

The photocatalytic efficiency of modified analogues were investigated by conducting experiments with 10 ppm Rhodamine B solution. The time course absorption spectra of copper, iron and silver loaded zinc oxide nanosheet assembled flowers are shown in Figure 9. As the time elapses the reduction in intensity of Rhodamine B at 554 indicates the degradation of the dye.

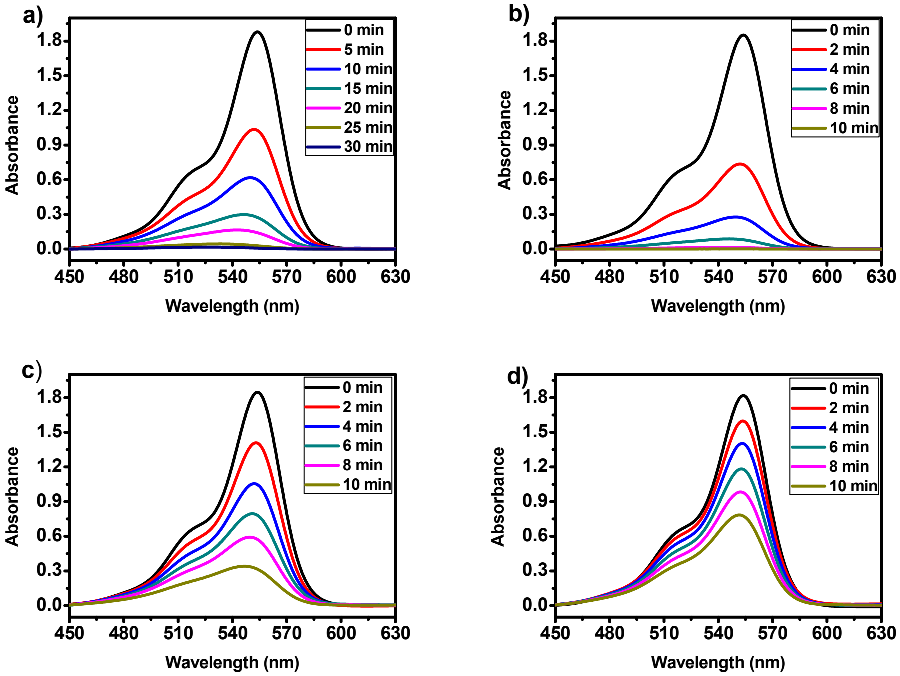

Figure 9. Absorption spectra of photodegradation of Rhodamine B in presence of (a) ZSF, (b) AgZSF and (c) CuZSF and (d) FeZSF catalyst systems. Catalyst dosage: 1g/L; [RhB]: 10 ppm.

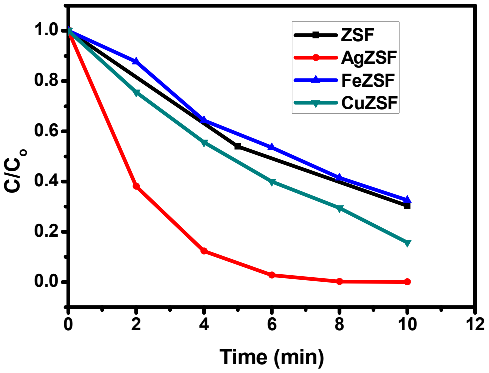

Figure 10. Plot of C/C$_o$ as a function of time

From Figure 10, it is obvious that the silver loaded system is highly efficient, which degraded the dye within 10 minutes of irradiation time. A complete removal of Rhodamine B was observed within this time interval.

Copper loaded ZSF system has shown a percentage degradation of 84.28 within 10 minutes. Compared to the parent zinc oxide nanosheet assembled flowers, iron loaded system has displayed a reduction in activity. The corresponding percentage degradations are 69.64 and 67.40 for ZSF and FeZSF respectively. These observations can be clearly explained on the basis of the scanning electron microscopic images shown above. It is evident from SEM images that the morphology of ZSF is retained only in AgZSF system. The predominant active surface planes together with silver loading enhances the activity. The flower like structure with distinct crystal plane orientation is distorted in copper and iron loaded ZSF systems. The aggregation of particles as well as the hindering of active sites may be the reason for reduction in activity.

The mineralization of Rhodamine B by the modified zinc oxide nanosheet assembled flower like systems are confirmed by the chemical oxygen demand (COD) measurements. The COD value is an indication of the presence of oxidizable species in the aqueous medium, which is expressed in mg/L. The initial dye solutions was taken as the blank and the solutions after photocatalytic dye degradation of Rhodamine B was the sample solutions for COD measurements. The COD values of solutions after photocatalytic reaction with the four systems i.e., ZSF, AgZSF, CuZSF and FeZSF within 10 minutes of UV irradiation and the blank values are summarized in Table 1. The lower COD value means higher photocatalytic degradation of organic pollutants. The lowest COD value is observed for silver loaded ZSF system, which is the most efficient catalyst system as observed from the absorption spectra of Rhodamine B degradation.

Table 1. COD values of the dye solution in mg/L before and after treatment with the catalysts

ZnO Systems	**ZSF**	**AgZSF**	**CuZSF**	**FeZSF**
COD of Blank (mg/L)	98.4	98.4	98.4	98.4
COD of sample solutions (mg/L)	49.3	20.03	35.6	52.1

The photoluminescence spectra give an idea about the electron-hole recombination in modified systems. All the modified systems have shown a reduction in intensity of PL spectra. The presence of foreign materials can easily trap electrons from the zinc oxide surface thereby inhibiting the electron-hole recombination. This is an important characteristics for the photocatalytic performance of the systems. Silver loaded ZSF system has shown the least electron-hole recombination property. The surface area values of the four systems are 13.648 m^2/g, 7.70 m^2/g, 7.39 m^2/g and 8.09 m^2/g for AgZSF, CuZSF, FeZSF and ZSF respectively. The increased surface area, comparable morphology and the lowest electron hole recombination efficiency make silver loaded zinc oxide nanosheets assembled flower like structures superior for the photocatalytic degradation of Rhodamine B dye.

5.2.7 Influence of the amount of silver on the photocatalytic activity

The sheet assembled flower like hierarchical structures modified with silver are found to be highly efficient for the photocatalytic degradation of Rhodamine B. the complete degradation of dye was achieved within a short period of time i.e., 10 minutes. Hence we have analysed the effect of varying weight percentages of silver incorporation on the zinc oxide sheet assembled flower like structure for the degradation study. Modification of ZSF with different weight percentages i.e., 1, 3, 5 and 7 % of silver were done using photodeposition method.

5.2.8 Characterization of silver loaded ZSF systems

a. X-Ray Diffraction analysis

The phase characteristics of silver modified systems were analysed by X-ray diffraction studies. ZSF system crystallises in hexagonal wurtzite structure, as obvious from the XRD pattern. Different weight percentages of silver, namely 1, 3, 5 and 7 were loaded in ZSF system. Additional peaks observed at 2θ values 38.1, 44.2 and 64.4 corresponds to (111), (200) and (220) crystal planes in face centered cubic lattice (fcc) of metallic silver (Figure 11). The intensity of the peaks increases with increase concentration of silver. No peaks of any other impurity were seen in the XRD pattern, indicating that the modified systems are composed of purely ZnO and Ag.

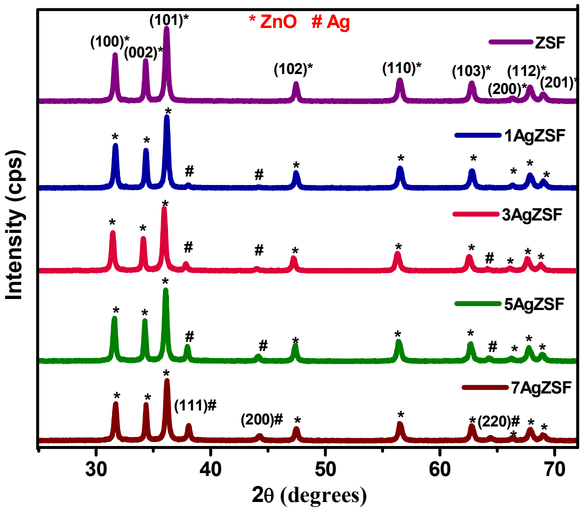

Figure 11. XRD pattern of ZSF system and its modified analogues with different molar percentages of silver

b. Scanning electron microscopy

Figure 12 depicts the scanning electron microscopic images of ZSF and all the silver modified ZSF systems. The morphology of all the silver modified systems were comparable to that of parent ZSF system. The nanosheet assembled flower like structures are seen in the figure. As the silver loading increase from 0 to 5 weight percentage (Figure 12a-12d), there were no aggregation of particle observed. Some aggregation of nanosheets were observed in the scanning electron microscopic image of 7% silver loaded ZSF system (Figure 12 f).

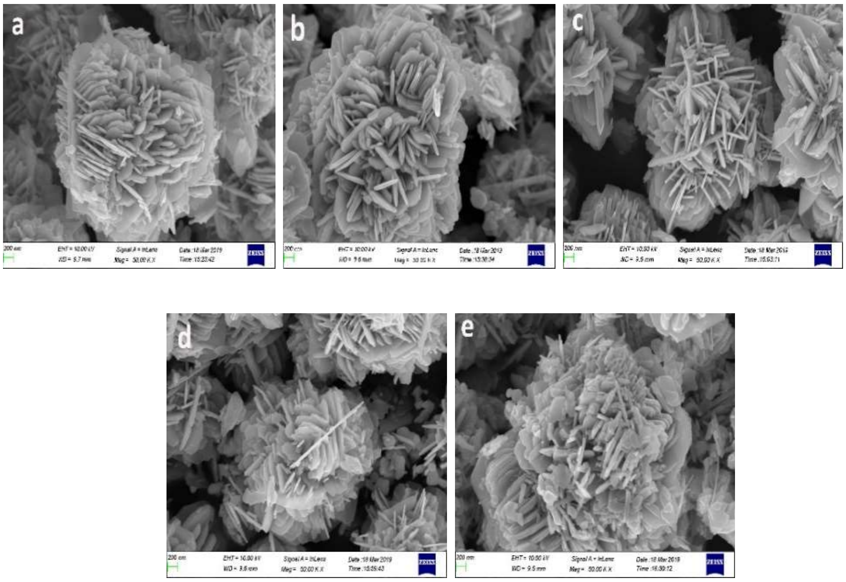

Figure 12. FESEM images of Zinc oxide systems ZSF (a) and the modified ZSF systems 1AgZSF (b); 3AgZSF(c); 5AgZSF (d) and 7AgZSF (e)

c. Transmission electron microscopy

The TEM images of 5% silver loaded zinc oxide flower like system is shown in Figure 13. The silver nanoparticles embedded in the petals of the flower like architectures is clearly seen from the image.

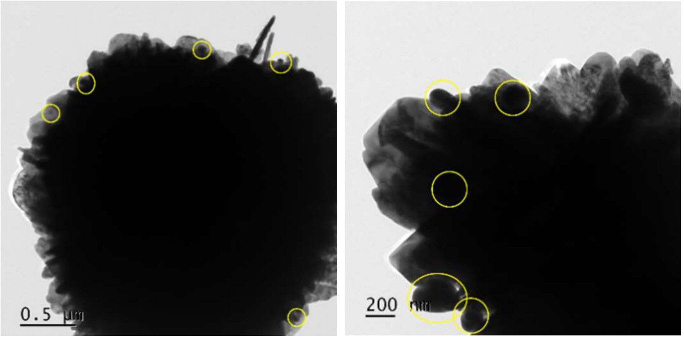

Figure 13. Transmission Electron Microscopic image of 5AgZSF

d. Surface area analysis

Here also the BET surface area analysis by nitrogen adsorption studies further substantiate the results observed from SEM images. The surface area of all the silver loaded systems increased from the parent ZSF system. The surface area values are 11.569 m^2/g, 13.648 m^2/g, 15.507 m^2/g and 14.148 m^2/g for 1, 3, 5 and 7% silver loaded ZSF systems respectively. The highest surface area is observed for 5AgZSF system.

e. UV-Vis Diffuse Reflectance Spectroscopy

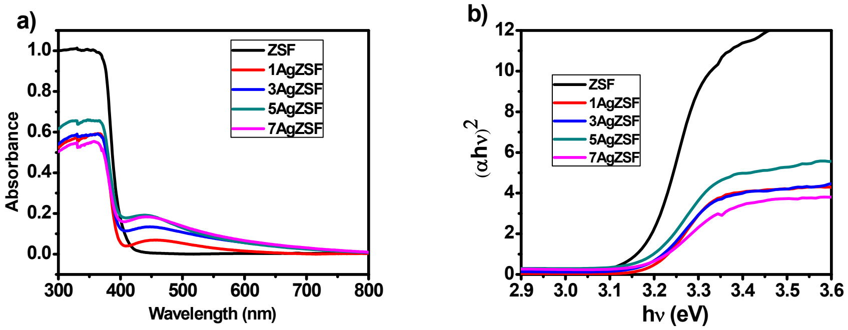

Figure 14. UV-Visible absorption spectra (a) and corresponding Kubelka-Munk plot (b) of ZSF and silver modified systems.

UV-Visible diffuse reflectance spectra were recorded in the wavelength range 250-700 nm. The absorption spectra and the corresponding Kubelka-Munk plots of ZSF and silver modified ZSF systems are displayed in Figure 14a and 14b respectively. A red shift in absorption is observed for all the modified analogues when compared to ZSF system. This is an indication of the absorption in visible region. Among the modified systems the intense absorption spectra is attributed to 5AgZSF. The band gap values calculated for zinc oxide nanosheet assembled flower like system is 3.18 eV. For 1AgZSF, 3AgZSF, 5AgZSF and 7AgZSF possessed the band gap values 3.17 eV, 3.16 eV, 3.15 and 3.17 eV respectively.

f. Photoluminescence study

The room temperature photoluminescence spectra of nanosheet assembled flower like architecture and silver loaded systems are plotted in Figure 15. All the spectra were measured at an excitation wavelength of 325 nm. The near band edge (NBE) emission responsible for the recombination of free excitons lies around 380-400 nm. It is apparent from the figure that the intensity of PL spectra of modified systems decreases from the parent ZSF system. It can be seen that the PL intensity decreases with increasing silver loading up to 5%. Thereafter an increase in intensity is observed for 7% Ag loaded ZSF, signifying the increased electron-hole recombination. The least intense PL spectrum is observed for 5% silver loaded ZSF system. The PL intensity order is as follows 5AgZSF < 7AgZSF < 3AgZSF < 1AgZSF < ZSF. This clearly indicates the lowest electron-hole recombination efficiency in 5AgZSF.

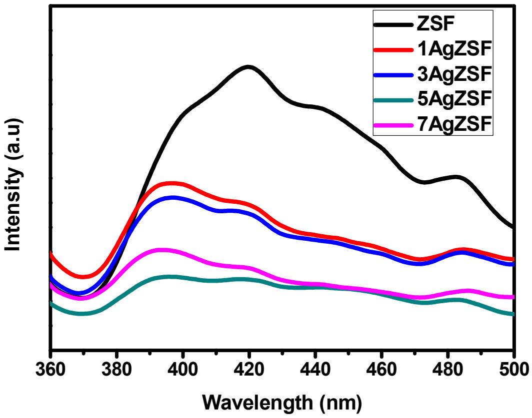

Figure 15. Photoluminescence spectra of ZSF and silver modified ZSF systems

g. X-Ray Photoelectron Spectroscopy (XPS) analysis

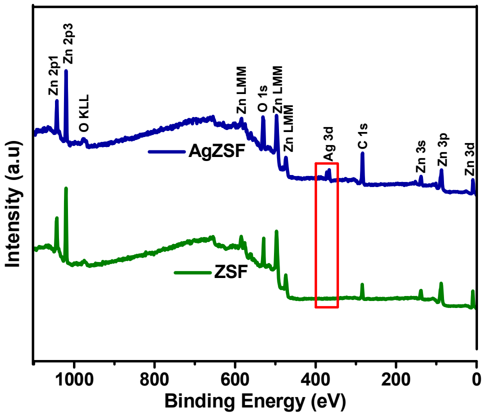

Figure 16. XPS spectra of the ZSF and 5AgZSF samples

The surface chemical composition and the valence state of the as-prepared ZSF and 5AgZSF samples were investigated using XPS analysis, and the corresponding results are shown in Figure 16. There are only C, Zn, and O element peaks in the pure ZnO sample. The peak of Zn $2p_{1/2}$ and Zn $2p_{3/2}$, respectively located at 1043.25 and 1020.15 eV, indicate the presence of ZnO in the sample. In Figure 16, the peak centred at 528.7 eV originates from the lattice oxygen of ZnO, and the peak at 530.95 eV is assigned to chemisorbed oxygen caused by the surface hydroxyl groups. Additional Ag peaks observed at binding energy values 372.1 eV (Ag $3d_{3/2}$) and 366.72 (Ag $3d_{5/2}$) represent silver in its metallic form (Ag[0]) in the heterostructured Ag–ZnO composites [91]. The relative area of different peaks give idea about percentage of different species in the sample. The presence of carbon might be caused by the XPS instrument. No other peaks can be observed in the XPS spectra. This result confirms that the ZnO is composed of only two elements, Zn and O, and the 5AgZSF samples are formed by Zn, O, and Ag, which is consistent with the XRD analysis results discussed above.

5.2.9 Photocatalytic removal of Rhodamine B by silver modified ZSF systems

To investigate the photocatalytic efficiency of silver loaded zinc oxide flower like system, we have used 10 ppm Rhodamine B as model pollutant. Figure 17 displays the absorption spectra of Rhodamine B during the photodegradation in presence of 1, 3, 5 and 7% silver loaded ZSF systems. The plot of C/Co for the photocatalytic degradation is shown in Figure 18 which clearly indicates the variation in removal efficiency of different molar percentage silver doped zinc oxide systems under UV irradiation.

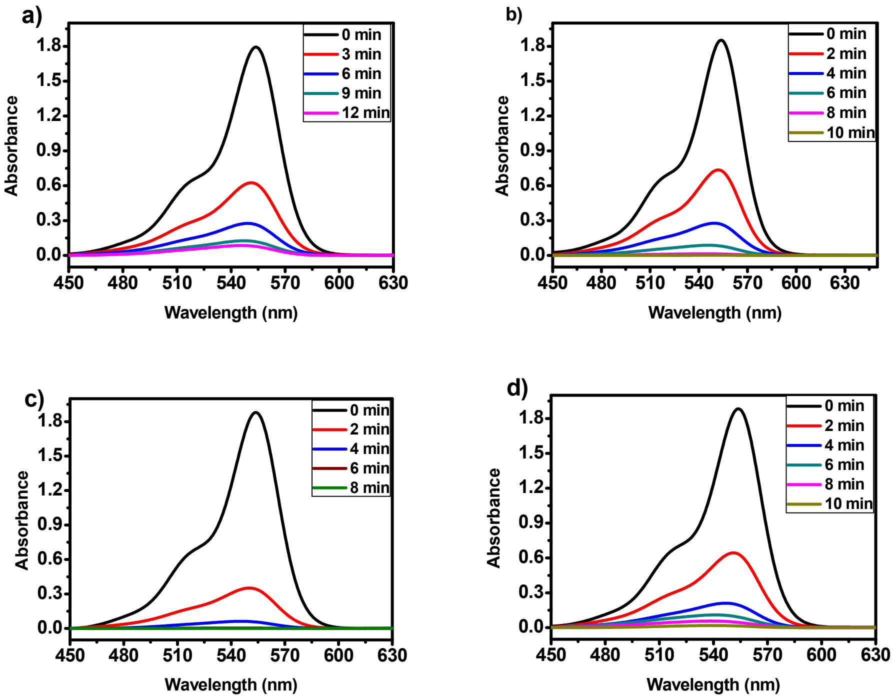

Figure 17. Absorption spectra of photodegradation of Rhodamine B in presence of (a) 1AgZSF, (b) 3AgZSF and (c) 5AgZSF and (d) 7AgZSF catalyst systems. [Catalyst dosage: 1g/L; [RhB]: 10 ppm]

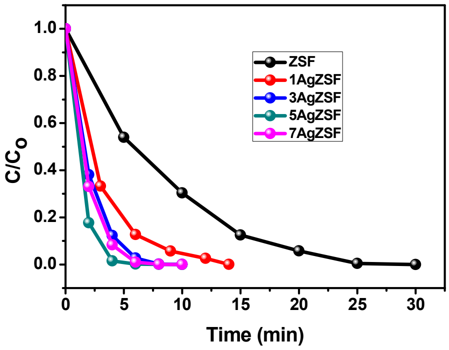

Figure 18. Plot of C/C$_o$ as a function of time

It can be clearly made out from the plot of C/Co that the activity of the Ag/ZnO composites first increases with increase in Ag amount. Further increase in the amount of Ag in the composite decreased the activity. The 5AgZSF sample exhibits the highest photodegradation rate. 5% silver loaded zinc oxide sheet assembled flower like system effected complete degradation of Rhodamine B within 6 minutes of UV irradiation. As presented in Figure. 18, the photodegradation efficiency of Rhodamine B is about 46.09%, 87.26%, 97.64%, 99.03% and100% for ZSF, 1AgZSF, 3AgZSF, 7AgZSF and 5AgZSF respectively, when the reaction was performed under UV-light for 6 min. The deposition of the Ag nanoparticles in an appropriate amount on the ZnO surface can effectively trap and transfer the photogenerated electrons, and thus reduce the recombination of the electron–hole pairs. However, when excess silver was used for loading, the aggregation and/or size increase of the Ag particles occurred, which is unfavourable for the inhibition of recombination of the electron–hole pairs, as evident form the PL spectra and surface area analysis.

Noble metal loading is one of the best method for the effective separation of electron-hole pairs in zinc oxide [92-94]. We have augmented the photocatalytic efficiency of ZnO flower like structures composed of nanosheets as the building units by incorporating silver nanoparticles. From the transmission electron microscopic analysis we confirm that the silver nanoparticles were embedded in the petals of zinc oxide flower like architectures. This silver nanoparticles act as an effective center for electron scavenging and thereby preventing the electron-hole recombination. The observations from photoluminescence spectra revealed that the zinc oxide flower like system with 5% silver loading has the lowest PL intensity and justifies the lower electron-hole recombination. We can say that silver particles embedded in the petals of zinc oxide flowers can act as electron-sink and thus enhance the efficiency of holes to get react with the hydroxyl ions to produce hydroxyl radicals, which plays the key role in the photo-oxidation of dye molecules. Moreover, the catalytic efficiency is further enhanced by surface plasmon absorption effect induced by metallic silver.

Liang and his co-workers [95] have reported a 100% degradation of Rhodamine B (8 ppm) within 180 minutes of UV irradiation using 5% silver loaded zinc oxide micro flowers. When compared to the above work, our systems stand superior in photocatalytic degradation of Rhodamine B, by all means. We have achieved complete removal of the dye within 6 minutes of UV irradiation under similar conditions, except that the dye concentration was 10 ppm. This suggests that the system reported herein is found to possess commendably high activity when compared to other systems found in literature.

Various factors influencing photocatalytic activity of 5AgZSF such as catalyst dosage, calcination temperature and effect of pH have been investigated. The amount of catalyst, calcination temperature and pH have significant role in tuning the photocatalytic activity of silver loaded zinc oxide system. The results are portrayed in Figure 19. As the catalyst dosage increases the photocatalytic degradation efficiency increases first and reaches a maximum for a catalyst dosage of 1 g/L (Figure 19a). This is due to the increase in active sites for the reaction. Further increase in the amount of catalyst will increase the turbidity of the solution thereby prohibiting the light penetration to the medium. This will substantially decrease the activity of the catalyst and hence the reduction in photodegradtion of organic dye, when the catalyst amount is increased further. As previously reported, the calcination temperature of the catalyst system has significant influence in the catalytic activity of zinc oxide. We have investigated the effect of calcination temperature on photocatalytic activity at three different temperatures viz., 400, 600 and 800^{o} C (Figure 19b). The rise in calcination temperature results in the decline of photocatalytic efficiency of 5AgZSF system. This observation can be attributed to the agglomeration of particles, which results in the reduction in active sites at higher temperature.

The pH of the waste water may vary in a wide range. Hence we have done photocatalytic degradation experiments at different pH values; 4, 7 and 10. It is found that the pH of the reaction medium significantly influences the photocatalytic degradation efficiency of the catalyst. This can be ascribed to the nature of organic dye and the surface charge property of zinc oxide. The value of zero point charge (ZPC), the pH at which the surface charge become zero, for zinc oxide is 8.9. At pH above the ZPC value, the surface of the material will be negatively charged and below it the surface will be positively charged. Since Rhodamine B is a cationic dye, the effective adsorption of the molecule on the catalyst surface will occur at basic pH i.e., pH above 8.9. Thus, the photocatalytic degradation of Rhodamine B is more favourable in basic pH than acidic or neutral pH. The results of our experiment is in agreement with this observation (Figure 19 c).

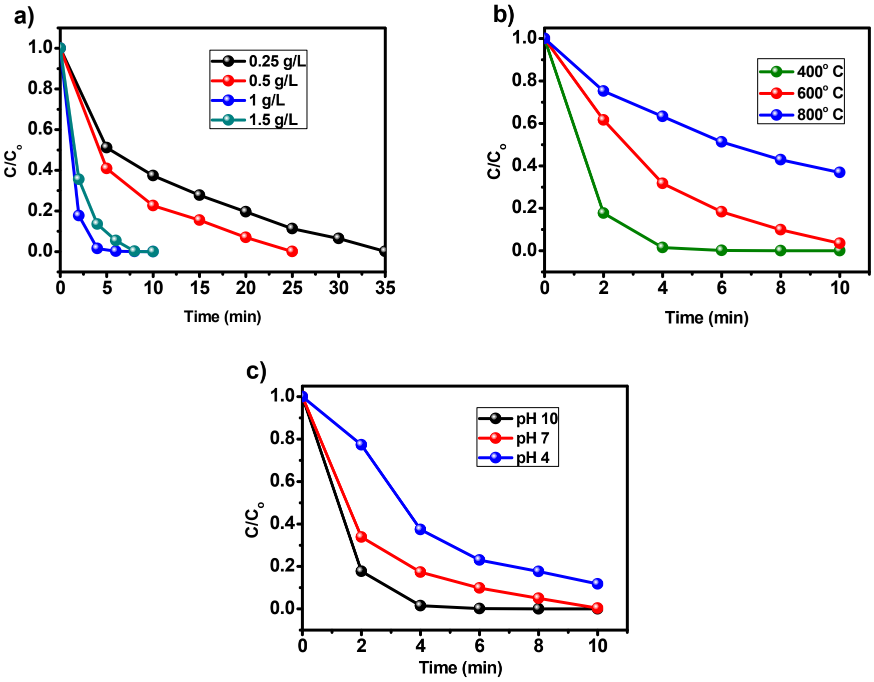

Figure 19. Effect of catalyst dosage (a), calcination temperature (b) and pH (c) on the photocatalytic performance of 5AgZSF system.

To get a better understanding on the photocatalytic degradation mechanism, it is necessary to identify the reactive species involved in the degradation mechanism. The common reactive species initiating the photodegradation of organic compounds are holes (h$^+$), electrons (e$^-$), hydroxyl radicals (OH$^\cdot$), and superoxide radicals (O$_2^{\cdot-}$). In this respect, we have used different scavengers for the reactive species such as isopropanol (IP) (OH$^\cdot$), EDTA (h$^+$) and ammonium oxalate (AO) (O$_2^{\cdot-}$). After the addition of isopropanol and EDTA the photocatalytic activity of 5AgZSF system is remarkably inhibited whereas the presence of ammonium oxalate has no significant influence on the activity. These results shown in Figure 20 indicate that OH$^\cdot$ and holes (h$^+$), are the main active species responsible for the degradation of Rhodamine B dye.

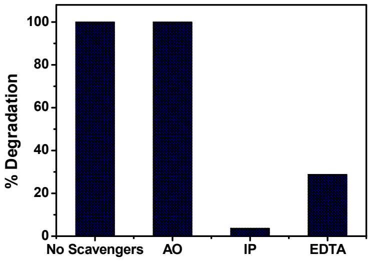

Figure 20. Effect of reactive species scavengers on photocatalytic performance of 5AgZSF system

5.2.10 Concomitant removal of Rhodamine B and Hexavalent chromium

The concomitant removal of organic dyes and heavy metal pollutants is important because of the co-existence of these pollutants in the waste water. We have conducted the photocatalytic experiments for the simultaneous removal of organic dye, Rhodamine B and heavy metal pollutant, hexavalent chromium using 5% silver loaded zinc oxide sheet flower (5AgZSF). A catalyst dosage of 1 g/L was used for the study. The concentration of dye taken was 10 ppm and that of Cr (VI) was 30 ppm. The experiments were carried out at both acidic and basic pH.

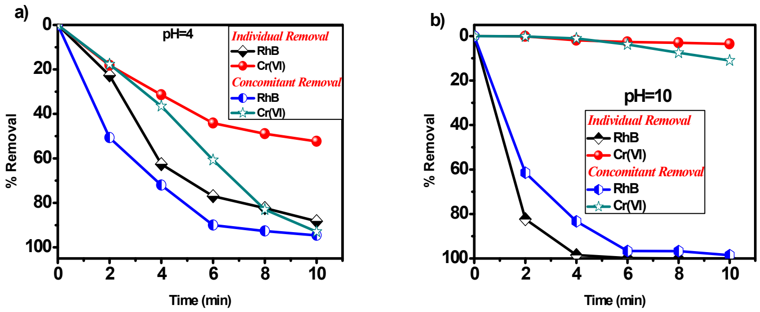

Figure 21. The individual and concomitant photocatalytic removal curves of Cr(VI) and Rhodamine B under UV irradiation in the presence of 5% AgZSF at pH 4 (a); pH 10 (b).

The individual and concomitant removal of Cr (VI) and Rhodamine B in aqueous medium using 5% AgZSF at different pH conditions is depicted in Figure 21. It is obvious from Figure 21a that, at pH 4, the percentage removal of Rhodamine B in single component system is 88.26 and that of Cr (VI) is 52.36 within 10 minutes of irradiation time. In the multicomponent aqueous solution there is an enhancement in the removal of both Rhodamine B and Cr(VI) and the % removal efficiencies are 94.61 and 92.95% respectively within the same duration. Figure 21b represents the individual and simultaneous removal of both the pollutants at pH 10. The single component reactions shows a complete removal of Rhodamine B within 10 minutes and the % removal of Cr (VI) at this pH is only 3.56. In the concomitant removal, the degradation of Rhodamine B was declined to 98.51% and that of Cr (VI) increased to 10.98%. The slight drop in the degradation of Rhodamine B may be due to the deposition of $Cr(OH)_3$ on the surface of the photocatalyst at higher pH values. The results are summarized in Table 2.

Table 2. % Removal of Rhodamine B and hexavalent chromium at different pH.

pH	% Degradation (within 10 minutes)			
	Monocomponent aqueous solution [RhB or Cr (VI)]		Two component aqueous solutions [RhB and Cr (VI)]	
	RhB	**Cr(VI)**	**RhB**	**Cr(VI)**
4	88.26	52.36	94.61	92.95
10	100	3.56	98.51	10.98

From the studies of photocatalytic removal of hexavalent chromium, we have seen that the acidic pH favours the reduction of Cr (VI) to Cr (III) and that of Rhodamine B in basic pH. It was also observed that the presence of hole scavengers in the reaction medium enhances the photoreduction of Cr (VI). The photocatalytic degradation mechanism and scavenger studies of 5AgZSF system clearly indicates that the degradation of Rhodamine B is effected by the holes present in the valence band. Rhodamine B is oxidized by holes in the valence band while Cr(VI) is reduced by electrons from the conduction band. This will decrease the chances of electron hole recombination, leaving more number of electrons available for the photoreduction of hexavalent chromium. Thus we can confirm that the organic pollutant Rhodamine B acts as a hole scavenger, which facilitate the reduction of hexavalent chromium by decreasing the electron-hole recombination chances. Thus the synergetic interaction between Rhodamine B and hexavalent chromium results in the simultaneous removal of these two pollutants.

5.2.11 Conclusions

Zinc oxide has been identified as an effective photocatalyst for the degradation of numerous organic as well as inorganic pollutants. The work dealt with the synthesis, characterization and photocatalytic activity of ZnO structures of different morphologies under UV radiation. The activity order for the photocatalytic degradation of organic pollutant Rhodamine B is ZSF> ZS> ZP> ZPF> ZRF> ZR. The highest activity was noticed for ZSF system with sheet assembled flower like morphology. An irradiation time of 30 minutes was taken for the complete removal of Rhodamine B. Zinc oxide architectures with nanosheet assembled flowers are highly active due to its unique hierarchical structure, highly exposed polar planes and low electron-hole recombination efficiency. ZnO systems with active polar (0001) planes are capable of adsorbing photoreactive species on their surface and enhance the photocatalytic activity. The easy sedimentation properties of ZSF system makes it more attractive towards photocatalytic degradation. Rather than surface area, the exposed surface active planes are decisive in tuning the photocatalytic activity.

Further modification of zinc oxide sheet assembled flower like system with different Metal/Metal Oxide dopants such as Ag, CuO and γ-Fe_2O_3. The systems were well characterized and the photocatalytic efficiency was tested. Among the modified systems the silver is in the metallic form and Cu and Fe are in the oxide form as confirmed from X-Ray diffraction analysis. The photocatalytic efficiency order is found to be AgZSF > CuZSF > ZSF > FeZSF. 100% degradation of Rhodamine B was achieved within 10 minutes of UV irradiation for AgZSF system. The enhancement in activity of silver doped system can be attributed to the lower intense photoluminescence spectra, which indicates lower electron-hole recombination in the system, and higher surface area. Silver can trap the photogenerated electrons from the semiconductor and allow the holes to form hydroxyl radicals which results in the degradation reaction of organic species present. Among the different weight percentage silver modified system the activity order is 5AgZSF > 7AgZSF > 3AgZSF > 1AgZSF > ZSF. The higher surface area and lower electron hole recombination efficiency of 5AgZSF system makes it efficient for the complete degradation of Rhodamine B within 6 minutes of irradiation time. The system is found to be efficient for the simultaneous removal of Rhodamine B and hexavalent chromium. The synergetic interaction between the pohooxidation of Rhodamine B and photoreduction of Cr (VI) enables the concomitant removal of both the pollutants from waste water.

References

1. G.L. Turdean, Design and development of biosensors for the detection of heavy metal toxicity, Int. J. Electrochem. (2011) 1–15.
2. Adverse health effects on heavy metals in children, 2011, www.who.int/ceh.
3. C. Gao, X.Y. Yu, S.Q. Xiong, J.-H. Liu, X.J. Huang, Electrochemical detection of arsenic (III) completely free from noble metal: Fe_3O_4 microspheres room temperature ionic liquid composite showing better performance than gold, Anal. Chem. 85 (2013) 2673–2680.
4. K. Tag, K. Riedel, H.-J. Bauer, G. Hanke, K.H.R. Baronian, G. Kunze, Amperometric detection of Cu^{2+} by yeast biosensors using flow injection analysis (FIA), Sens. Actuators B: Chem. 122 (2007) 403–409.
5. S.J.S. Flora, M. Mittal, A. Mehta, Heavy metal induced oxidative stress & itspossible reversal by chelation therapy, Indian J. Med. Res. 128 (2008) 501–523.
6. S.J.S. Flora, Structural, chemical and biological aspects of antioxidants forstrategies against metal and metalloid exposure, Oxid. Med. Cell. Longev. (2009) 191–206.
7. D. Tekis, J. Wang, Simultaneous electrochemical detection of multiple heavy metal ions in water, AzTE Arizona Technol. Enterp., 1996, pp. 1.
8. F.S. Al-Fartusie, S.N. Mohssan, Essential Trace Elements and Their Vital Roles in Human Body, Indian Journal of Advances in Chemical Science 5 (2017) 127-136.
9. M. Valko, H. Morris, M.T.D. Cronin, Metals, toxicity and oxidative stress, Curr. Med. Chem. 12 (2005) 1161–1208.

10. P.B. Tchounwou, C.G. Yedjou, A.K. Patlolla, D.J. Sutton, Heavy metal toxicity and the environment, EXS 101 (2012) 133–164.
11. X. Rajaganapathy, M.P. Sreekumar, Heavy metal contamination in soil, water and fodder and their presence in livestock and products: a review, J. Environ. Sci. Technol. 4 (2011) 234–249.
12. H. Oliveira, "Chromium as an environmental pollutant: insights on induced plant toxicity," Journal of Botany, 2012, Article ID 375843, 8 pages, 2012.
13. L.E. Eary, R. Dhanpat, Chromate removal from aqueous wastes by reduction with ferrous ion, Environ. Sci. Technol. 22 (1988) 972–977.
14. H. Wang, X. Yuan, Y. Wu, G. Zeng, X. Chen, L. Leng, Z. Wu, L. Jiang, H. Li, Facile synthesis of amino functionalized titanium metal organic frameworks and their superior visible light photocatalytic activity for Cr(VI) reduction, J. Hazard. Mater. 286 (2015) 187–194.
15. C. Mondal, M. Ganguly, J. Pal, A. Roy, J. Jana, T. Pal, Morphology controlled synthesis of SnS_2 nanomaterial for promoting photocatalytic reduction of aqueous Cr(VI) under visible light, Langmuir 30 (2014) 4157–4164.
16. T.K. Yurik, A.K. Pikaev, Radiolysis of weakly acidic and neutral aqueous solutions of hexavalent chromium ions, High Energy Chem. 33 (1999) 208–212.
17. A.D. Dayan, A.J. Paine, Human & experimental toxicology mechanisms of chromium toxicity, carcinogenicity and allergenicity: review of the literature from 1985 to 2000, Hum. Exp. Toxicol. 20 (2001) 439–451.

18. S.K. Dey, S. Roy, Effects of chromium on certain aspects of cellular toxicity, Iran. J. Toxicol. 2 (2009) 260–267.
19. A.H. Smith, Hexavalent chromium, yellow water, and cancer: a convoluted saga, Epidemiology 19 (2008) 24–26.
20. S.R. Nair, Evaluation of in-vivo antioxidant activity of various extracts of *Triumfetta rotundifolia (linn.)* on chromium (VI) induced oxidative stress in albino rats, Int. J. Pharm. Pharm. Sci. 5 (2013) 336–338.
21. A.K. Patlolla, C. Barnes, C. Yedjou, V.R. Velma, P.B. Tchounwou, Oxidative stress, DNA damage and antioxidant enzyme activity induced by hexavalent chromium in Sprague-dawley rats, Environ. Toxicol. 24 (2009) 66–73.
22. C. Montserrat, P.D.C. Fresco, A. Kortenkamp, Chromium (VI) mediated DNA damage: oxidative pathways resulting in the formation of DNA breaks and a basic sites, Chem. Biol. Interact. (1999) 29–39.
23. J.K. Yang, S.M. Lee, Removal of Cr(VI) and humic acid by TiO_2 photocatalysis, Chemosphere 63 (2006) 1677.
24. G. S. Khorramabadi, R. D. C. Soltani, A. Rezaee, A.R. Khataee, A. J. Jafari, Utilisation of immobilised activated sludge for the biosorption of chromium (VI), Can. J. Chem. Eng. 90 (2012) 1539.
25. X. Jin, M. Jiang, J. Du, Z. Chen, Removal of Cr(VI) from aqueous solution by surfactant modified kaolinite, J. Ind. Eng. Chem. 2014, 20, 3025-3032.
26. “The World’s Worst Toxic Pollution Problems 2011 Report”, Blacksmith Institute in collaboration with Green Cross Switzerland.

27. T. Nandy, S.N. Kaul, S. Shastry, U. Manivel, C.V. Deshpande, Wastewater management in cluster of tanneries in Tamil Nadu through implementation of common effluent treatment plants. J. Sci. Ind. Res. 1999 58, 475–516.
28. Central pollution control board (CPCB), 2013. Pollution Assessment: River Ganga. Status of Grossly Polluting Industries (GPI).
29. Kaul, S.N., Szpyrokowicz, L., Gautam, A., Khanna, D.R., 2005. Wastewater Management with Special Reference to Tanneries. Discovery publishing house, New Delhi, pp. 480.
30. A.A. Belay, Impacts of chromium from tannery effluent and evaluation of alternative treatment options. J. Environ. Prot. 1 (2010) 53–58.
31. R.R. Ray, Adverse hematological effects of hexavalent chromium: an overview, Inter.discip. Toxicol. 9 (2016) 55–65.
32. A. Kumar, R. Barthwal, Hexavalent chromium effects on hematological indices in rats. Bull. Environ. Contain. Toxicol. 46 (1991) 761-768.
33. S. Mishra, R.N. Bharagava, Toxic and genotoxic effects of hexavalent chromium in environment and its bioremediation strategies, J. Environ. Sci. Health Part C, 34 (2016) 1-32.
34. R.S. Luippold, K.A. Mundt, R.P. Austin, E. Liebig, J. Panko, C. Crump, K. Crump, D. Proctor, Lung cancer mortality among chromate production workers, *Occup. Environ. Med.*, 60 (2003) 451.
35. A. Arita, M. Costa, Environmental Agents and Epigenetics, Environmental Agents and Epigenetics. Handbook of Epigenetics, (2011) 459–476.

36. H. P. Singh, P. Mahajan, S. Kaur, D. R. Batish, and R. K. Kohli, "Chromium toxicity and tolerance in plants," Environmental Chemistry Letters, 11 (2013) 229–254.
37. S. K. Panda and S. Choudhury, "Chromium stress in plants," Brazilian Journal of Plant Physiology, 17 (2005) 95–102.
38. F. L. Petrilli and S. De Flora, Toxicity and mutagenicity of hexavalent chromium on *Salmonella typhimurium*, Applied and Environmental Microbiology, 33 (1977) 805–809.
39. V. Velma, S. S. Vutukuru, and P. B. Tchounwou, "Ecotoxicology of hexavalent chromium in freshwater fish: a critical review," Reviews on Environmental Health, 24 (2009)129–145.
40. A. McCartor, D. Becker, Blacksmith Institute's World´s Worst Pollution Problems Report 2010, Blacksmith Institute, New York. www.worstpolluted.org
41. J.M. Serena, The groundwater beneath their feet, The Hindu, February 18, 2017.
42. IARC, Chromium, nickel and welding, IARC Monogr Eval Carcinog Risks Hum, 49 (1990) 1-248.
43. J. K. Sueker, Chromium. Environmental Forensics (1964) 81–95.
44. Guidelines for drinking-water quality, 2nd ed. Vol. 2. Health criteria and other supporting information. World Health Organization, Geneva, 1996.
45. G. Qin, M.J. McGuire, N.K. Blute, C. Seidel, L. Fong, Hexavalent Chromium Removal by Reduction with Ferrous Sulfate, Coagulation,

and Filtration: A Pilot-Scale Study, Environ. Sci. Technol. 39 (2005) 6321-6327.

46. C.E. Barrera-Díaz, V. Lugo-Lugo, B. Bilyeu, A review of chemical, electrochemical and biological methods for aqueous Cr(VI) reduction, Journal of Hazardous Materials 223– 224 (2012) 1– 12.
47. C.P. Huang, A.R. Bowers, Activated carbon processes for the treatment of chromium (VI)-containing industrial wastewaters, Water Sci. Technol. 13 (1980) 629–649.
48. V.K. Gupta, S. Agarwal, T.A. Saleh, Chromium removal by combining the magnetic properties of iron oxide with adsorption properties of carbon nanotubes, Water Res. 45 (2011) 2207–2212.
49. T. Chen, T. Wang, D. Wang, H. Xue, J. Zhao, X. Ding, S. Wu, J. He, Synthesis of ordered large-pore mesoporous carbon for Cr (VI) adsorption, Mater. Res. Bull.46 (2011) 1424–1430.
50. G.Q. Chen, W.J. Zhang, G.M. Zeng, J.H. Huang, L. Wang, G.L. Shen, Surface modified phanerochaete chrysosporium as a biosorbent for Cr (VI)-contaminated wastewater, J. Hazard. Mater. 186 (2011) 2138–2143.
51. A. R. Shakoori, M. Makhdoom, R. U. Haq, Hexavalent chromium reduction by a dichromate resistant gram-positive bacterium isolated from effluents of tanneries, Appl. Microbiol. Biotechnol. 53 (2000) 348-351.
52. W. Zhang, J. Liu, Z. Ren, S. Wang, C. Du, J. Ma, Kinetic study of chromium (VI) facilitated transport through a bulk liquid membrane using tri-n-butyl phosphate as carrier, Chem. Eng. J. 150 (2009) 83–89.

53. P.S. Kulkarni, V. Kalyani, V.V. Mahajani, Removal of hexavalent chromium by membrane based hybrid processes, Ind. Eng. Chem. Res. 46 (2007) 8176–8182.
54. S. Edebali, E. Pehlivan, Evaluation of Amberlite IRA96 and Dowex 1×8 ion exchange resins for the removal of Cr (VI) from aqueous solution, Chem. Eng. J. 161 (2010) 161–166.
55. Y. Deng, T. Long, H. Zhao, L. Zhu, J. Chen, Application of porous N-methylimidazolium strongly basic anion exchange resins on Cr (VI) adsorption from electroplating wastewater, Sep. Sci. Technol. 47 (2012) 256–263.
56. H. Yoneyama, Y. Yamashita, H. Tamura, Heterogeneous photocatalytic reduction of dichromate on n-type semiconductor catalysts, Nature 282 (1979) 817-818.
57. S. Lakshmi, R. Renganathan, S. Fujita, Study on TiO_2-mediated photocatalytic degradation of methylene blue, J. Photochem. Photobiol. A: Chem. 88 (1995) 163-167.
58. W.Z. Tang, H. An, UV/TiO_2 photocatalytic oxidation of commercial dyes in aqueous solutions, Chemosphere 31(1995) 4157-4170.
59. H. Lachheb, E. Puzenat, A. Houas, M. Ksibi, E. Elaloui, C. Guillard, J.M. Herrmann, Photocatalytic degradation of various types of dyes (Alizarin S, Crocein Orange G, Methyl Red, Congo Red, Methylene Blue) in water by UV-irradiated titania, Appl. Catal. B: Environ. 39 (2002) 75–90.
60. H.C. Liang, X.Z. Li, Effects of structure of anodic TiO_2 nanotube arrays on photocatalytic activity for the degradation of 2, 3-dichlorophenol in aqueous solution, J. Hazard. Mater. 162 (2009) 1415–1422.

61. L. Wang, S.Z. Kang, X. Li, L. Qin, H. Yan, J. Mu, Rapid and efficient photocatalytic reduction of hexavalent chromium by using "water dispersible" TiO_2 nanoparticles, Mater. Chem. Phys. 178 (2016) 190-195.
62. J.K. Yang, S.M. Lee, Removal of Cr(VI) and humic acid by using TiO_2 photocatalysis, Chemosphere 63 (2006) 1677–1684.
63. Z. He, Q. Cai, M. Wu, Y. Shi, H. Fang, L. Li, J. Chen, J. Chen, S. Song, Photocatalytic reduction of Cr(VI) in an aqueous suspension of surface-fluorinated anatase TiO_2 nanosheets with exposed {001}facets, Ind. Eng. Chem. Res. 52 (2013) 9556–9565.
64. Q. Sun, H. Li, S. Zheng, Z. Sun, Characterizations of nano-TiO_2/diatomite composites and their photocatalytic reduction of aqueous Cr (VI), Appl. Surf. Sci. 311 (2014) 369–376.
65. Z. Jin , Y.X. Zhang, F.L. Meng, Y. Jia, T. Luo, X.Y. Yu, J. Wanga, J.H. Liua, X.J. Huang, Facile synthesis of porous single crystalline ZnO nanoplates and their application in photocatalytic reduction of Cr(VI) in the presence of phenol, J. Hazard. Mater. 276 (2014) 400–407.
66. S. Sakthivel, B. Neppolian, M.V. Shankar, B. Arabindoo, M. Palanichamy, V. Murugesan, Solar photocatalytic degradation of azo dye: comparison of photocatalytic efficiency of ZnO and TiO_2, Sol. Energy Mater.Sol.Cells. 77 (2003)65–82.
67. V.L. Chandraboss, J. Kamalakkannan, S. Prabha, S. Senthilvelan, An efficient removal of methyl violet from aqueous solution by an AC-Bi/ ZnO nanocomposite material, RSC Adv. 5 (2015) 25857–25869.

68. J.H. Zeng, B.B. Jin, Y.F. Wang, Facet enhanced photocatalytic effect with uniform single-crystalline zinc oxide nanodisks , Chem. Phys. Lett. 472 (2009) 90–95.
69. K.M. Parida, S.S. Dash, D.P. Das, Physico-chemical characterization and photocatalytic activity of zinc oxide prepared by various methods, J. Colloid Interface Sci. 298 (2006) 787–793.
70. Q. Wan, T. H. Wang, J. C. Zhao, Enhanced photocatalytic activity of ZnO nanotetrapods, Appl. Phys. Lett. 87 (2005) 1-3.
71. S. Chakrabarti, B. Chaudhuria, S. Bhattacharjee, A.K. Rayb, B.K. Dutta, Photo-reduction of hexavalent chromium in aqueous solution in the presence of zinc oxide as semiconductor catalyst, Chem. Eng. J. 153 (2009) 86–93.
72. S. Challagulla, R. Nagarjuna, R. Ganesan, S. Roy, Acrylate-based polymerizable sol−gel synthesis of magnetically recoverable TiO_2 supported Fe_3O_4 for Cr(VI) photoreduction in aerobic atmosphere, ACS Sustainable Chem. Eng. 4 (2016) 974−982.
73. M.N. Joubani, M.S. Siboni, J.K. Yang, M. Gholami, M. Farzadkia, Photocatalytic reduction of hexavalent chromium with illuminated ZnO/TiO_2 composite, J. Ind. Eng. Chem. 22 (2015) 317-323.
74. Z. Jin, Y.X. Zhang, F.L. Menga, Y. Jia, T. Luo, X.Y. Yu, J. Wang, J.H. Liu, X.J. Huang, Facile synthesis of porous single crystalline ZnO nanoplates and their application in photocatalytic reduction of Cr(VI) in the presence of phenol, Journal of Hazardous Materials 276 (2014) 400–407.
75. M.S. Siboni, M. Farrokhi, R.D.C. Soltani, A. Khataee, S. Tajassosi, Photocatalytic reduction of hexavalent chromium over ZnO nanorods immobilized on kaolin, Ind. Eng. Chem. Res. 53 (2014) 1079−1087.

76. J. Yu, S. Zhuang, X. Xu, W. Zhu, B. Feng, J. Hu, Photogenerated electron reservoir in hetero-p–n CuO–ZnO nanocomposite device for visible-light driven photocatalytic reduction of aqueous Cr(VI), J. Mater. Chem. A, 3 (2015) 1199–1207.
77. A. Katocha, S.W. Choia, H.W. Kimb, S.S. Kim, Highly sensitive and selective H_2 sensing by ZnO nanofibers and the underlying sensing mechanism, J. Hazard. Mater. 286 (2015) 229–235.
78. J. Yu, X. Yu, Hydrothermal Synthesis and photocatalytic activity of zinc oxide hollow spheres, *Environ. Sci. Technol. 42* (**2008)** 4902–4907.
79. A.B. Djurisic, A.M.C. Ng, X.Y. Chen, ZnO nanostructures for optoelectronics: Material properties and device applications, Prog. Quant. Electron. 34 (2010) 191–259.
80. Y. Hames, Z. Alpaslan, A. Kösemen, S.E. San, Electrochemically grown ZnO nanorods for hybrid solar cell applications, Solar Energy. 84 (2010) 426–431.
81. J. Domenech, J. Munoz, Photocatalytical reduction of Cr(V1) over ZnO powder, Electrochim. Acta. 32 (1987) 1383-1386.
82. P. Banerjee, S. Chakrabarti, S. Maitra, B.K. Dutta, Zinc oxide nano-particles – sonochemical synthesis, characterization and application for photo-remediation of heavy metal, Ultrason. Sonochem. 19 (2012) 85–93.
83. J. Liu, Y. Zhao, J. Mab, Y. Dai, J. Li, J. Zhang, Flower-like ZnO hollow microspheres on ceramic mesh substrate for photocatalytic reduction of Cr(VI) in tannery wastewater, Ceram. Int. 42 (2016) 15968-15974.

84. E. Selli, A.D. Giorgi, G. Bidoglio, Humic acid-sensitized photoreduction of Cr(VI) on ZnO particles, Environ. Sci. Technol. 30 (1996) 598-604.
85. G.C.C. Yang, S.W. Chan, Photocatalytic reduction of chromium(VI) in aqueous solution using dye-sensitized nanoscale ZnO under visible light irradiation, J. Nanopart. Res. 11 (2009) 221–230.
86. M. Qamar, M.A. Gondal, Z.H. Yamani, Laser-induced efficient reduction of Cr(VI) catalyzed by ZnO nanoparticles, J. Hazard. Mater. 187 (2011) 258–263.
87. X. Zhao, F. Lou, M. Li, X. Lou, Z. Li, J. Zhou, Sol_gel-based hydrothermal method for the synthesis of 3D flower-like ZnO microstructures composed of nanosheets for photocatalytic applications, Ceram. Int. 40 (2014) 5507–5514.
88. A. Mc Laren, T. Valdes-Solis, G. Li, S.C. Tsang, Shape and size effects of ZnO nanocrystals on photocatalytic activity, J. Am. Chem. Soc. 131 (2009) 12540–12541.
89. J. H. Zeng, B. B. Jin, Y. F.Wang, Facet enhanced photocatalytic effect with uniform single-crystalline zinc oxide nanodisks, Chem. Phys. Lett. 472 (2009) 90–95.
90. P. Worajittiphon, K. Pingmuang, B. Inceesungvorn, N. Wetchakun, S. Phanichphant, Enhancing the photocatalytic activity of ZnO nanoparticles for efficient Rhodamine B degradation by functionalised graphene nanoplatelets, Ceram. Int. 41 (2015) 1885–1889.
91. X. Zhao, S. Su, G. Wu, C. Li, Z. Qin, X. Lou, J. Zhou, Facile synthesis of the flower-like ternary heterostructure of Ag/ZnO

encapsulating carbon spheres with enhanced photocatalytic performance, Applied Surface Science, 2017, 406, 254-264.

92. C. Mondal, J. Pal, M. Ganguly, A. K. Sinha, J. Jana, T. Pal, A one pot synthesis of Au–ZnO nanocomposites for plasmon-enhanced sunlight driven photocatalytic activity, New J. Chem., 2014, 38, 2999-3005.
93. M.J. Height, S.E. Pratsinis, O. Mekasuwandumrong, P. Praserthdam, Ag-ZnO catalysts for UV-photodegradation of methylene blue, Applied Catalysis B: Environmental 63 (2006) 305–312.
94. S.M. Hosseini, I. A. Sarsari, P. Kameli, H. Salamati, Effect of Ag doping on structural, optical, and photocatalytic properties of ZnO nanoparticles, Journal of Alloys and Compounds 640 (2015) 408–415.
95. Y. Liang, N. Guo, L. Li, R. Li, G. Ji, S. Gan, Facile synthesis of Ag/ZnO micro-flowers and their improved ultraviolet and visible light photocatalytic activity, *New J. Chem.,* 2016, 40, 1587-1594.

Chapter 6

Summary and scope of future work

Summary

In the scenario of environmental pollution, the importance of zinc oxide as a photocatalyst and gas sensing platform is gaining much attention. The properties of zinc oxide is highly dependent on its morphology and crystal plane orientation. Here, zinc oxide with morphologically different structures are synthesized by a facile low temperature hydrothermal method using different surfactant molecules, cetyltrimethyl ammonium bromide (CTAB), hexamethylene tetramine (HMTA) and polyvinylpyrrolidone (PVP). The systems are well characterized using X-Ray diffraction analysis (XRD), Scanning electron microscopy (SEM), Transmission electron microscopy (TEM), Fourier Transform Infra-Red Spectroscopy (FTIR), surface area analysis by BET method, Diffuse Reflectance UV spectroscopy (UV-DRS), photoluminescence study (PL) and Raman spectroscopy.

The morphological analysis by electron microscopic analysis revealed that the six zinc oxide systems are morphologically different. Nanoparticles, nanosheets, nanorods, nanoparticle assembled flowers, nanosheet assembled flowers and nanorod assembled flowers are the resulted morphologies of the zinc oxide systems. The crystalline nature of the prepared systems were obvious from the X-ray diffraction analysis. The characteristics vibrational modes in zinc oxide structures was obtained from FTIR spectral analysis. The oxygen vacancy defects in the prepared zinc oxide systems were analysed by raman spectroscopy and photoluminescence studies. The optical properties of the zinc oxide architectures were analysed by Diffuse Reflectance UV spectroscopy and photoluminescence study.

A detailed investigation on the gas sensing properties of the well characterized zinc oxide structures are carried out. The sensitivity of the six zinc oxide structures follows the order nanosheets > nanosheet flower >

nanoparticles > nanorods> nanorods flower> nanoparticle flower. The zinc oxide nanosheets having the highest oxygen vacancy defects, as evidenced from photoluminescence study, and more exposed surface active planes is highly sensitive for the detection of NO_2 gas. The crystal plane dependent NO_2 sensing behaviour of zinc oxide is identified. Highly exposed surface active planes with plenty of oxygen vacant sites are supposed to be the reason for the higher efficiency of nanosheets, which possessed a low surface area. It was also noted that the zinc oxide nanosheets is selective for the detection of NO_2 than NH_3. The high stability, sensitivity, short response and recovery time, large detection range and low detection limit are the major advantages of zinc oxide nanosheet gas sensor. The low temperature sensitivity of the zinc oxide nanosheets with fast response and recovery characteristics makes it promising for practical applications. The nanoparticles having highest surface area has shown maximum response towards NH_3.

Zinc oxide has been identified as an effective photocatalyst for the removal of numerous pollutants from aqueous medium. The morphologically different zinc oxide architectures are exploited for the photocatalytic reduction of hexavalent chromium. The order of photocatalytic reduction efficiency of zinc oxide structures is given as nanoparticles > nanosheet flower > nanoparticle flower > nanoparticle flower > nanosheets > nanorods > nanorods flower. The results indicated that the catalyst system with particle like morphology i.e., ZP system was more active towards the photoreduction of hexavalent chromium. Surface area together with electron-hole recombination efficiency play significant role in tuning the catalytic activity. The higher photocatalytic activity of ZP system was attributed to its large surface area (40.34 m^2/g) among the systems and comparatively low electron-hole recombination efficiency. Our study revealed that the pH of the solution, initial Cr(VI) concentration and hole scavengers have remarkable role in the photocatalytic reduction of hexavalent chromium. It is obvious from the present study that, hole scavengers have significant role in the reduction of hexavalent chromium by zinc oxide photocatalyst. The activity of the ZP system was enhanced to a greater extent in the presence of ethanol, a hole scavenger in the reaction medium. Even after five cycles of reaction there was only a negligible decrease in the activity, which indicates the stability of the system.

The activity order for the photocatalytic degradation of organic pollutant Rhodamine B is nanosheet flower (ZSF)> nanosheets (ZS)> ZP (nanoparticles)> ZPF (nanoparticle flower)> nanorods flower (ZRF)> nanorods (ZR). The highest activity was noticed for ZSF system with sheet assembled flower like morphology. An irradiation time of 30 minutes was taken for the complete removal of Rhodamine B. Zinc oxide architectures with nanosheet assembled flowers are highly active due to its unique hierarchical structure, highly exposed polar planes and low electron-hole recombination efficiency. ZnO systems with active polar (0001) planes are capable of adsorbing photoreactive species on their surface and enhance the photocatalytic activity. The easy sedimentation properties of ZSF system makes it more attractive towards photocatalytic degradation. Rather than surface area, the exposed surface active planes are decisive in tuning the photocatalytic activity.

Modification of zinc oxide sheet assembled flower like system was done with different Metal/Metal Oxide dopants such as Ag, CuO and γ-Fe_2O_3. The systems were well characterized by X-Ray diffraction analysis (XRD), Scanning electron microscopy (SEM), Transmission electron microscopy (TEM), surface area analysis by BET method, Diffuse Reflectance UV spectroscopy (UV-DRS), photoluminescence study (PL) and X-ray photoelectron spectroscopy (XPS) and the photocatalytic efficiency was tested. Among the modified systems the silver is in the metallic form and Cu and Fe are in the oxide form as confirmed from the X-Ray diffraction analysis.

The photocatalytic efficiency order is found to be AgZSF > CuZSF > ZSF > FeZSF. 100% degradation of Rhodamine B was achieved within 10 minutes of UV irradiation for AgZSF i.e., silver loaded zinc oxide nanosheet flower like system. The enhancement in activity of silver doped system can be attributed to the lower intense photoluminescence spectra in the near band edge emission, which indicates lower electron-hole recombination in the system, and higher surface area when compared to copper and iron loaded and pure zinc oxide nanosheet flowers. Silver can trap the photogenerated electrons from the semiconductor and allow the holes to form hydroxyl radicals which results in the degradation reaction of organic species present. The photocatalytic degradation efficiency of zinc oxide nanosheets modified with different weight percentages of silver follows the order 5AgZSF > 7AgZSF > 3AgZSF > 1AgZSF > ZSF. The higher surface area and lower electron hole recombination efficiency of 5% silver loaded zinc oxide nanosheets assembled flowerlike system (5AgZSF) make it efficient for the complete degradation of Rhodamine B within 6 minutes of irradiation time. The system is found to be efficient for the simultaneous removal of Rhodamine B and hexavalent chromium from aqueous medium. The synergetic interaction between the pohooxidation of Rhodamine B and photoreduction of Cr (VI) enables the concomitant removal of both the pollutants easy.

To sum up, the present work has identified ZnO nanosheets with exposed surface active planes as efficient for sensing oxidizing gases. 5% Ag modified ZnO microflowers were evolved as excellent photocatalyst for degradation of organic dyes.

Scope of future work

The results of the present investigation shed light on the utilization of the prepared zinc oxide systems for future applications. The gas sensing applications of zinc oxide nanosheets can be tuned by modification with other metals and metal oxides. It will augment the sensitivity of the material at room temperature and give a solution for the power hungry sensors. The incorporation of foreign materials will also rectify the selectivity issues related with metal oxide gas sensors. The selective detection of various toxic gases can be achieved in this regard. The zinc oxide system will also be used as a sensing platform for various biological molecules as well as heavy metal pollutants in the liquid phase.

Coming to the photocatalytic application studies, it is understood that zinc oxide is an alternate for the well explored TiO_2 photocatalyst. The zinc oxide flower like architectures composed of nanosheets (ZSF) as the building blocks is found to be highly efficient for the photocatalytic application studies. The system will be utilized for the degradation of various other organic pollutants like phenolic compounds and pesticides. Modification of the systems with other metals or metal oxides will further tune the visible light driven photocatalysis.

PRESENTATIONS

2017:- Oral presentation at the International conference on Emerging Frontiers of Chemical Science 2017 (EFCS 2017) at the department of Chemistry, Farook college.

2017:- Oral presentation at ICEEAMSF-2017 held at Kongu Engineering College, Erode

2016:- Poster presentation at SCICON 2016, International Conference on Advanced Materials held at Amrita University, Coimbatore.

2015:- Poster Presentation at the National conference on Advanced Nanomaterials organised by Nirmalagiri College, Kannur

LIST OF PUBLICATIONS

1. T.V.A. Kusumam, T. Panakkal, T. Divya, M.P. Nikhila, M. Anju, K. Anas, N.K. Renuka, Morphology controlled synthesis and photocatalytic activity of zinc oxide nanostructures, Ceram. Int. 42 (2016) 3769–3775.
2. Arsha Kusumam T.V, N. K. Renuka, Effect of crystal plane orientation in tuning the photocatalytic activity of zinc oxide particles, Materials Today: Proceedings 5 (2018) 16118–16124.
3. M. P. Nikhila, A. K. Akhila, T. Divya, M. Anju, T. V. Arsha Kusumam and N. K. Renuka, P123 and solvent-assisted synthesis of titania nanocuboids with co-exposed {101} and {001} planes, CrystEngComm, 2017,19, 511-518
4. M. Anju, T. Divya, M. P. Nikhila, T. V. Arsha Kusumam, A. K. Akhila, V. A. Ansi and N. K. Renuka* An elegant and handy selective sensor for ppt level determination of mercury ions, RSC Adv., 2016, 6, 109506
5. Divya T., Nikhila M.P., Anju M., Arsha Kusumam T.V., Akhila A.K., Ravikiran Y.T.,Renuka N.K., Sensors and Actuators A 261 (2017) 85–93